1-1-2013

Studying On Capacity Fade Mechanisms of Li-Ion Batteries Through Modeling

Yiling Dai
University of South Carolina - Columbia

STUDYING ON CAPACITY FADE MECHANISMS OF LI-ION BATTERIES THROUGH MODELING

by

Yiling Dai

Bachelor of Science
Nanjing University, 2010

Submitted in Partial Fulfillment of the Requirements

For the Degree of Doctor of Philosophy in

Chemical Engineering

College of Engineering and Computing

University of South Carolina

2013

Accepted by:

Ralph E. White, Major Professor

Edward P. Gatzke, Committee Member

Xinyu Huang, Committee Member

Harry J. Ploehn, Committee Member

John W. Weidner, Committee Member

Lacy Ford, Vice Provost and Dean of Graduate Studies

Dedication

To my parents!

Acknowledgements

I would like to thank my research advisor, Prof. Ralph White, for having me work in his group and supporting me at all levels. Under his guidance, I have learnt a lot. I would also like to thank my committee members, Prof. Edward Gatzke, Prof. Xinyu Huang, Prof. Harry Ploehn, and Prof. John Weidner, for their valuable suggestions and comments towards this work.

I thank all of previous and present members in the group: Dr. Sean Rayman, Dr. Long Cai, Dr. Meng Guo, Dr. Saeed Rahimian, Tingting, Eric for their inputs to my research. In particular, I would like to thank Dr. Long Cai for his helpful discussions on this work.

I am lucky to live and study here with many kind friends -Tianyuan, Weijian, Yuanya, Zhiyong et al. Many thanks should go to them for making my time wonderful here.

Finally, I am indebted to my parents and my brother for their continuous support and encouragement.

Abstract

Li-ion batteries are promising candidates as power sources for hybrid electric/electric vehicles, as well as storage devices for renewable energies (wind, solar). Longer life batteries are more desirable for large-scale application, which would help lower the capital cost ($/KW) and improve the system stability. However, the aging problem of Li-ion batteries obstructs their fast penetration into these markets. The cell life can be improved based on an in-depth understanding of the fade mechanisms. The purpose of this dissertation is to explore, through a mathematical modeling approach, failure mechanisms of Li-ion batteries.

To study the capacity fade of a $LiMn_2O_4$ (LMO) electrode, a pseudo-2 dimensional (P2D) model based on porous electrode theory is first developed. This model takes into account the loss of LMO due to acid attack and the breakdown of the Li ion diffusion pathway due to the formation of the solid electrolyte interphase (SEI) film. The acid stems from the decomposition of the $LiPF_6$ salt and the organic solvent. The decrease of the Li-ion diffusion coefficient is implemented as an empirical function of the loss of LMO. Good agreement is achieved between our simulation results and the experimental data reported in literature. Next, we provide a mathematical model to study the generation of mechanical stress in LMO particles, which are mixed with $LiNi_{0.8}Co_{0.15}Al_{0.05}O_2$ (NCA) as a battery cathode. The mechanical equations which

capture the stress buildup in the LMO particle due to Li insertion/extraction are incorporated into the P2D model. The predictions obtained from our blended cathode (LMO and NCA) model show that the stress generated in the LMO particles is reduced at the end of discharge due to adding NCA particles in the electrode. This detailed model can help elucidate the effect of adding NCA particles on the improvement of the LMO electrode performance. Finally, a two-dimensional model is developed for large-format LMO/Carbon cells to understand inhomogeneous degradation. The model considers the non-uniform porous electrode properties and the electrode mismatch. The simulation results show that when the anode edge is extended over the cathode edge, the LMO particles near the edge will suffer larger potential drop, larger charge/discharge depth, and higher diffusion-induced stress. Therefore, the loss of LMO is more pronounced near the electrode edge in agreement with experimental observations.

Table of Contents

List of Tables

List of Figures

List of Symbols

a specific surface area, $m^2\ m^{-3}$

a_j specific surface area in electrode region j, $m^2\ m^{-3}$

a_k specific surface area for reaction k, $m^2\ m^{-3}$

a_2 specific surface area for solvent oxidation reaction, $m^2\ m^{-3}$

$a_{2,set}$ specific surface area preset for solvent oxidation reaction, $m^2\ m^{-3}$

$brugg_j$ Bruggeman coefficient of region j (j=*pos*, *s*ep)

c_i concentration for species i (i=H_2O, Mn^{2+}, H^+, Li^+), mol m^{-3}

c_i^0 initial concentration for species i (i=H_2O, Mn^{2+}, H^+, Li^+), mol m^{-3}

c_s concentration of lithium ions in the solid particle, mol m^{-3}

c_s^0 initial concentration of lithium ions in the solid particle of electrode, mol m^{-3}

$c_{s,max}$ maximum concentration of lithium ions in the solid particle, mol m^{-3}

$c_{s,avg}$ volume averaged lithium ions concentration in the particles, mol m^{-3}

$c_{s,surf}$ surface lithium ions concentration of particles, mol m^{-3}

D_i electrolyte diffusion coefficient for species i (i=H_2O, Mn^{2+}, H^+, Li^+), $m^2\ s^{-1}$

D_s lithium ion diffusion coefficient in the solid particle of electrode, $m^2\ s^{-1}$

F Faraday's constant, 96487 C $equiv^{-1}$

I_{app} applied current density, A m^{-2}

J pore wall flux of lithium ions, mol $m^{-2}\ s^{-1}$

i_1 solid phase current density, A m^{-2}

i_2 solution phase current density, A m^{-2}

$i_{b,Li}$ current density on Li metal surface for Li ion, A m^{-2}

$i_{b,i}$ current density on Li metal surface for species i (i= Mn^{2+}, H^+), A m^{-2}

i_0 exchange current density, A m^{-2}

$i_{n,j}$ local transfer current density for Li ions intercalation/deintercalation reaction in electrode region j (j=*pos*,*sep*), A m^{-2}

i_s local transfer current density for solvent oxidation reaction, A m^{-2}

k_i reaction rate constant for side reaction i (i=2, 3)

$k_{b,Li}$ reaction rate constant on Li metal surface for Li ion, A $m^{-0.5}$ $mol^{-0.5}$

$k_{b,i}$ reaction rate constant on Li metal surface for species i (i= Mn^{2+}, H^+), A m mol^{-1}

k_{Li} Li intercalation/deintercalation reaction rate constant, A $m^{2.5}$ $mol^{-1.5}$

L_{cc} thickness of current collector, m

L_p thickness of positive electrode, m

L_s thickness of separator, m

n_1 adjust factor

pos positive electrode

$q_{s,avg}$ volume averaged flux in the particle, mol m^{-4}

r radial coordinate, m

R universal gas constant, J mol^{-1} K^{-1}

$R_{s,i}$ reaction rate for side reaction i (i=1, 3), mol m^{-2} s^{-1}

$R_{s,2}$ reaction rate for side reaction 2, mol m^{-3} s^{-1}

R_{pos} radius of the active spinel, m

R_{conc} contact resistance on the surface of particle type k, $\Omega\ m^2$

sep separator

SOC state of charge

$q_{s,avg}$ volume averaged flux in the particle, mol m^{-4}

t_+ Li^+ transference number in the electrolyte

T environment temperature, K

u displacement, m

U_i potential of reaction on the Li metal surface for species i (i=Mn^{2+}, H^+), V

U_i^θ equilibrium potential of reaction on the Li metal surface for species i (i=Mn^{2+}, H^+), V

U_p equilibrium potential of Li intercalation/deintercalation reaction in cathode, V

U_{side} equilibrium potential of solvent oxidation side reaction, V

$\overline{V}$ molar volume of $LiMn_2O_4$

V_{cell} cell potential, V

x spatial coordinate, m

X_c carbon content in the composite electrode, %

$X_{c,set}$ preset value of carbon content in the composite electrode, %

z_i number of electrons for species i (i=Mn^{2+}, H^+)

Z_1, Z_2 integration constant

Greek letters

α_a anodic transfer coefficient

α_c cathodic transfer coefficient

α_i the activity coefficient for species i (i=Mn^{2+}, H^+)

$\varepsilon_{1,pos}$ volume fraction of the solid phase in the positive electrode

$\varepsilon_{2,j}$ porosity of region *j* (*j=pos*, *sep*)

ε_{ij} strain

θ dimensionless concentration of lithium ions in the solid particle ($\theta = c_{s,surf}/c_{s,\max}$)

θ^0 initial dimensionless concentration of lithium ions in the solid particle

κ ionic conductivity of the electrolyte, S m^{-1}

κ_{eff} effective ionic conductivity of the electrolyte, S m^{-1}

σ electronic conductivity of the solid phase, S m^{-1}

σ_{eff} effective electronic conductivity of the solid phase, S m^{-1}

σ_r radial component of stress, N m^{-2}

σ_t tangential component of stress, N m^{-2}

ϕ_1 solid phase potential, V

ϕ_2 solution phase potential, V

η overpotential, V

η_{Li} overpotential for Li intercalation/deintercalation reaction, V

η_s overpotential for the solvent oxidation side reaction, V

ν Poisson's ratio

δ_{ij} Kronecker delta

τ Tortuosity

Ω Partial molar volume, m^3 mol^{-1}

Subscript

cc current collector

e extra electrolyte area

eff	effective
max	maximum
C	Carbon
h	hydrostatic
LMO	$LiMn_2O_4$
n	negative electrode
NCA	$LiNi_{0.8}Co_{0.15}Al_{0.05}O_2$
r	radial direction
t	tangential direction
s	separator
p	positive electrode

1 Introduction

1.1 Li-ion Batteries

Li-ion batteries are one important type of rechargeable batteries, which store electric energy in electrochemical form. The main components of a Li-ion battery include a cathode, a separator, an anode, and the electrolyte filled in the electrode porosity. The active materials in the cathode and anode serve as the host matrix for reversible insertion/extraction of lithium ions. During charge and discharge, lithium ions transfer through the separator between anode and cathode.

Due to its large advantage over other competing technologies, Li-ion batteries have become the most popular power sources for many portable consumer applications. Recently, the problems of finite fossil-fuel and environment pollution have pushed the development of renewable energies and electric vehicles. To succeed in these fields, an efficient energy storage system is required. Because Li-ion batteries show great benefits in terms of energy and power density, they are considered as potential candidates in these applications. However, for a wide use of lithium ion technology areas, further improvements are required, such as reducing cost and improving lifetime [1, 2].

1.2 Capacity Fade of Li-ion Batteries

The capacity fade of lithium ion batteries is a serious problem that limits large-scale application. Many degradation mechanisms have been proposed to explain the failure of lithium ion batteries [3, 4]. The loss of cyclable lithium is considered the most important

to capacity loss [5, 6]. The charge stored in the battery is determined by the amount of cyclable lithium in the system. However, the loss of cyclable lithium due to solvent reduction and Li plating on the carbonaceous anode cannot be avoided. This generates a solid electrolyte interface (SEI) film on the carbon surface primarily during the initial cycling, but the formation may continue due to cycling. The loss of active material is considered another contribution to the capacity loss. Most of cathode active materials are found unstable in common organic electrolytes. The experiment has observed that the surface of cathode material is covered by surface films after soaked in solutions [7, 8]. Also, the dissolution of transition metal from cathode active material into the electrolyte is largely reported [9, 10]. Several experiments have suggested the electrolyte oxidation will promote the metal dissolution [10-12]. The dissolved metal will be transferred to the anode, which causes the unstable SEI layer and the loss of cyclable lithium [13, 14]. Besides the chemical degradation, particle fracture of the active material is severe for many active materials due to electrochemical cycling [15-17]. Particle fracture not only leads to loss of active material, but also increases resistance and a loss of cyclable lithium. The particle fracture would expose fresh active material surface for SEI layer formation. If the passive SEI layer becomes thicker, it leads to a loss contact between the active material and conductor [18].

It is essential to know the fundamental mechanisms of the capacity fading, because an in-depth understanding is helpful to improve the cell life. However, the cell failure mechanisms are not yet fully understood, especially for special electrode materials, as the diagnosis of cell failure is very challenging. Since Li-ion batteries are complicated

systems, a mathematical model would be a great help for understanding the complex phenomena.

1.3 Mathematical Modeling of Li-ion Batteries

There have been several physics-based models for Li-ion batteries to assist the understanding of aging phenomena inside batteries. The first detailed model to describe the discharge behavior of Li-ion batteries was developed by Newman's group [19, 20]. In the model, the diffusion in both the solid phase and liquid phase is considered. With the full consideration, the model predicted results are good in agreement with experimental data. Darling et al. then modified the model to study the electrolyte oxidation on the cathode [21]. This model-based method presents a simple way for estimating the kinetic parameters of the side reaction, although the detailed mechanistic information is not provided. Arora et al. [22] then applied the model to study the Li-plating issues on the graphite-based negative electrode. The work provided a way to analyze the effect of various operating conditions, cell designs and charging protocols on the lithium deposition side reaction. There are other studies implementing this detailed model to study the SEI layer formation on the carbonaceous anode [6, 23]. For example, Sikha et al. predicts the porosity distribution in the aged electrode due to SEI formation [23]. This is confirmed by the experimental observation [24].

These studies have proven the values of simulation to help understand cell failure. Also, this model can be used to aid in cell design and optimization, which reduces experimental work. In addition, the physical model with aging mechanisms is valuable to the battery management system for the prognostics of cell life.

1.4 Outline of the Dissertation

LMO based cells have many advantages over other kinds of Li-ion batteries. However, the capacity loss is significant in LMO based cells, especially in high temperature. In Chapter 2, a complicated manganese (Mn) dissolution mechanism was proposed to explain the capacity loss in LMO based cells. The model includes the acid attack on the active material and the SEI film formation on the surface of the particles in this electrode. The acid is considered to be generated by the decomposition of the $LiPF_6$ salt and the organic solvent. The effects of operating conditions, such as end of charge potential, and kinetics of side reactions on battery life, are also investigated.

The previous experiments suggest that an addition of layered active materials to a LMO based cell, like NCA, can reduce Mn dissolution and improve the cell cycling and storage performance at elevated temperature. However, the origin of the effect is unknown. In Chapter 3, stress generation inside LMO particle in the mixed electrode (LMO and NCA) was investigated, and then compared to that of a pure LMO electrode. The analysis of the mechanical behavior of LMO particles in the mixed electrode is conducted.

In Chapter 4, a two-dimensional model is developed to study the inhomogeneous degradation of the LMO electrode in a large format LMO/Carbon cell. Both the porous electrode property and electrode mismatch are considered. The analysis is based on the model predicting electrochemical, chemical, and mechanical behavior. The model developed also predicts the influence of different design adjustable parameters (such as: the anode extension length, the capacity ratio, the porosity, and the electrode thickness)

and electrolyte properties (such as: the diffusion coefficient and the ionic conductivity) on the performance of LMO electrode.

2 Development of a Capacity Fade Model for Spinel $Li_xMn_2O_4$ Electrode

2.1 Introduction

Spinel $LiMn_2O_4$ (LMO) has been considered as one of the most attractive cathode materials for rechargeable lithium-ion batteries because of its low cost, environmentally benign, high cell potential and high rate capability, which especially makes it a favorable candidate for electric vehicles (EV) and hybrid electric vehicles (HEV) application. However, this material exhibits severe capacity fading during cycling or storage at elevated temperature. This shortcoming makes it less competitive with other cathode materials and limits its wide use in commercial batteries.

Several capacity fading mechanisms of spinel electrode have been proposed, such as degradation of the active material, electrolytes decomposition and surface-film formation [3]. Among these, manganese (Mn) dissolution is mainly believed to be the most critical factor resulting in deterioration,[9] although the cause and effect of Mn dissolution is not well understood. Jang et al. [10] proposed that the solvent molecules are electrochemically oxidized and some generated species promote Mn dissolution. They reported that significant amounts of Mn^{2+} ions were detected when a composite electrode was placed near a polarized carbon electrode, but this did not happen when the carbon electrode was left at the open-circuit condition. In their following work [11], they compared Mn dissolution and capacity loss in Li/LMO cells in various electrolyte solutions. They concluded that acids were generated as a result of electrochemical

oxidation of solvent molecules on a composite cathode which caused electrode dissolution. Chromik et al.[25] reported that just after the reversible Li deintercalation a peak of LMO electrode the current rose steeply and a large number of protons were generated in the electrolyte, which were quantitatively measured by using a rotating ring/disk-electrode (RRDE). Also, the solvent irreversible anodic oxidation potential was found to be more negative at the LMO electrode than that at a Pt electrode due to the electrocatalytic activity of LMO. Lee et al.[26] employed the RRDE and a gas analysis technique to study hydrogen evolution in overcharged $LiCoO_2$/graphite cells. Abundance of H_2 evolution during overcharge was observed. They argued that it could not be attributed to the trace water and suggested that the anodic decomposition of the electrolyte was accompanied by acid generation which contributed to the gas evolution. Wang et al.[12] proposed that the acid which is generated in the cell causes Mn dissolution. In addition, solvent oxidation at the cathode and a water reaction with $LiPF_6$ are two main sources of acid generation. Pasquier et al.[27] revealed that generated acid within the cell was responsible for Mn dissolution and formation of a protonated phase. Myung et al.[28] disassembled C/LMO cells cycled at 60 ^{o}C and found very high HF concentrations in the used electrolyte. An increase of HF concentration was also observed in the electrolyte storage LMO electrode at room and high temperature.[29, 30]

Although Mn dissolution was considered to be the critical factor of capacity fading, experimental work found that the capacity losses caused by Mn dissolution alone cannot account for all the capacity fading.[31] Furthermore, factors causing capacity loss may not occur separately. For example, electrolyte oxidation not only causes Mn dissolution but also leads to the loss of cycle lithium. Moreover, the soluble manganese and the

produced acid can be transported to anode and be reduced at the anode, which could destroy the solid electrolyte interphase (SEI) film on the carbon anode.[13, 14] Also, a passive film was observed on the particle surfaces of the cathode electrode.[8, 32] The main sources of film formation come from Mn dissolution which results in inactive material, precipitation of a Mn composite such as MnF_2, as well as the solvent oxidation products [32, 33]. This passive film on the cathode active material would block Li ion diffusion into or out of the bulk electrode and lead to cell polarization loss.

Park et al. [34] developed a mathematical model to describe the degradation of spinel LMO cathode based on the mechanism of Mn(III) disproportionation reaction proposed by Lu et al.[35] They argued that the changes in effective transport properties are the important role in capacity degradation. Recently, a more complete model was developed by Cai et al,[36] which takes the decrease of radius of the active material into account by using a shrinking core model to describe the solid phase diffusion in the cathode. Also, the formation of an inactive material layer which causes a resistance increase in the cathode was included in the model. The kinetics and parameters used in these models were obtained from experiment data where spinel was only statically soaked in the electrolyte. However, it has been reported that the amount of dissolved Mn after cycling or applied potential is much larger than the amount dissolved due to being statically exposed.[10, 31]

In this Chapter, we present an electrochemical model for the capacity fade of the spinel LMO by including acid generation from two side reactions (solvent oxidation on the cathode surface and $LiPF_6$ decomposition) and acid attack induced Mn dissolution. The decrease of the Li ion diffusion coefficient in the solid phase due to the passive film

formation on the cathode active material surface was also included as another factor that causes cell capacity loss. The effects of cell operation/fabrication conditions on cell performance were investigated by using the mathematical model presented in this paper. The effects include cell cycling voltage range and the carbon content in the composite electrode. Various kinetic values were chosen to investigate the contribution of the different side reactions to the capacity loss. To exclude the influence of the loss of cycle lithium and the change in the carbon anode, a Li/LMO half-cell was used in the simulations.

2.2 Model Development

The model system considered in this paper is a Li/LMO half-cell which consists of a LMO working electrode, a Li metal counter electrode, two layers of 25 μm Celgard separator and 2 M $LiPF_6$ dissolved in EC/DMC/PC. The main side reactions proposed in this model include acid generation from solvent oxidation as well as $LiPF_6$ decomposition, and the acid induced Mn dissolution. These side reactions have been discussed in several experimental reports [11, 12, 21, 27, 33, 37-46]. The side reaction scheme and rate expression are presented.

Side Reactions:

It is assumed that the solvent decomposes according to the following oxidation reaction [11, 27, 37-39],

$$Solvent \xrightarrow{oxidation} Sl_o + H^+ + e^- \tag{2.1}$$

where Sl_o represents the overall products of the solvent oxidation and includes soluble species and solid species. The rate of the solvent decomposition is charge-transfer-kinetic controlled and can be expressed by a Butler-Volmer expression as follows:

$$i_s = i_{0,s}[\exp(\frac{\alpha_{a,s}F}{RT}\eta_s) - \exp(-\frac{\alpha_{c,s}F}{RT}\eta_s)] \tag{2.2}$$

$$\eta_s = \phi_1 - \phi_2 - U_{side} \tag{2.3}$$

where $i_{0,s}$ is the exchange current density, F is Faraday's constant, R is the universal gas constant, T is the environment temperature, η_s is the over-potential for the electrochemical side reaction in equation (2.1) and is defined as the difference between the solid phase potential, ϕ_1, and the solution phase potential, ϕ_2, with respect to the equilibrium potential of the side reaction, U_{side}.

An anodic Tafel expression can be used to describe the rate expression if the decomposition reaction is considered to be irreversible. Consequently, the rate expression can be simplified as follows:[21]

$$i_s = i_{0,s} \exp(\frac{\alpha_{a,s}F}{RT}\eta_s) \tag{2.4}$$

The H^+ production rate due to the reaction given in equation (2.1) can be written as follows:

$$R_{s,1} = \frac{i_s}{F} \tag{2.5}$$

The acidity of the electrolyte containing a $LiPF_6$ salt can be affected by the reaction of $LiPF_6$ with residual water in the organic solvent.[41, 47] That is, the $LiPF_6$ salt is decomposed as follows:

$$LiPF_6 \rightarrow LiF+PF_5 \tag{2.6}$$

where the product PF_5 reacts with water to form HF:

$$PF_5+H_2O \rightarrow POF_3+2HF \tag{2.7}$$

The reaction rate of $LiPF_6$ decomposition is given by:[42, 43]

$$R_{s,2}=k_2[H_2O]^2[LiPF_6] \tag{2.8}$$

where k_2 is the reaction rate constant for the $LiPF_6$ decomposition reaction, $[LiPF_6]$ is the total $LiPF_6$ concentration added in the electrolyte including ionized $LiPF_6$. The concentration, $[LiPF_6]$, can be approximated by the concentration of Li^+, $[Li^+]$, due to the high ionization of $LiPF_6$. That is:

$$R_{s,2} = k_2 c_{H_2O}{}^2 c_{Li^+} \tag{2.9}$$

where c_{H_2O} is concentration of H_2O ,$[H_2O]$, c_{Li^+} is concentration of Li^+ ,$[Li^+]$.

The acid attack on the active material in the cathode, $LiMn_2O_4$, is assumed to occur as follows:[11, 12, 27, 44]

$$4H^+ +2LiMn_2O_4=2Li^+ +Mn^{2+} +\frac{3}{2}Mn_2O_4+2H_2O \tag{2.10}$$

It is supposed that the reaction rate for acid attack on the active material shown in equation (2.10) is dominated by the acid concentration in the solution.[11, 45, 46] Consequently, the reaction rate for the reaction in equation (2.10) is given by:

$$R_{s,3} = k_3 c_{H^+} \tag{2.11}$$

where k_3 is the reaction rate constant for the acid attack on the active material, c_{H^+} is concentration of H^+, $[H^+]$.

Electrochemical Model:

The material balance for Li^+ in the electrolyte is given as follows:

$$\varepsilon_{2,j} \frac{\partial c_{Li^+}}{\partial t} = -\nabla(-D_{eff,Li} \nabla c_{Li^+}) - R_{s,2} + \frac{1-t^+}{F} a_j i_{n,j}, \; j = pos, sep \tag{2.12}$$

where $\varepsilon_{2,j}$ is the porosity of j region (*pos*=positive, *sep*=separator), $D_{eff,Li}$ is the effective diffusion coefficient of Li^+ in the binary electrolyte, t^+ is the transference number, a_j is the specific area, $i_{n,j}$ is the local transfer current density in the electrode region j. In the separator region (j=*sep*), the last term in equation (2.12) is zero since there is no Li intercalation/deintercalation reaction. The specific area in the positive electrode, a_{pos}, is defined as:

$$a_{pos} = 3 \frac{\varepsilon_{1,pos}}{R_{pos}} \tag{2.13}$$

where $\varepsilon_{1,pos}$ is volume fraction of the solid active material in the positive electrode, and R_{pos} is radius of the spherical particle.

The current density distribution in the solid phase, i_1, is given by Ohm's law as follows:

$$i_1 = -\sigma_{eff} \nabla \phi_1 \tag{2.14}$$

where σ_{eff} is the effective electronic conductivity of the cathode.

The current density in the electrolyte i_2 is given in a modified form of Ohm's law as follows:

$$i_2 = -\kappa_{eff} [\nabla \phi_2 - 2 \frac{RT(1-t^+)}{F} \nabla \ln c_{Li^+}] \tag{2.15}$$

where κ_{eff} is the effective ionic conductivity of the electrolyte in the cathode.

The total current density is conserved and thus:

$$\nabla \cdot (i_1 + i_2) = 0 \tag{2.16}$$

Due to conservation of charge, the divergence of the current density in the solution phase can be related to the two electrochemical reactions: Li intercalation/deintercalation reaction and solvent oxidation side reaction as follows:

$$\nabla \cdot i_2 = \sum_{k=1,2} a_k i_{n,k} \tag{2.17}$$

where a_k represents the specific surface area, $i_{n,k}$ represents the pore wall flux current density of Li intercalation/deintercalation reaction (k=1) and solvent oxidation side reaction (k=2), respectively:

$$
\begin{aligned}
a_1 &= a_{pos} \\
i_{n,1} &= i_{n,pos} \\
i_{n,2} &= i_s
\end{aligned}
\tag{2.18}
$$

Guyomard et al. [37] reported that the solvent oxidation occurs mostly on the conductive carbon black, so the area per unit volume for the solvent oxidation, a_2, is related to the carbon content (weight percent), $X_c\%$, in the composite electrode as follows:

$$
a_2 = \frac{X_c}{X_{c,set}} a_{2,set} \tag{2.19}
$$

where $X_{c,set}$ represent the carbon content for a preset value and it is set to 10%; $a_{2,set}$ is value of a_2 corresponding to the preset carbon content $X_{c,set}$. The value of $a_{2,set}$ is reported by $a_{2,set} i_{0,s}$ as given in Table 2.2.

Substitution equation (2.15) into (2.17) yields,

$$
\nabla \cdot (\kappa_{eff} \nabla \phi_2 - 2 \frac{\kappa_{eff} RT(1-t^+)}{F} \nabla \ln c_{Li^+}) = \sum_{k=1,2} a_k i_{n,k} \tag{2.20}
$$

where the source term on the right side of equation (2.20) is zero in the separator region.

Substitution of equations (2.14) and (2.17) into (2.16) yields:

$$
\nabla \cdot (-\sigma_{eff} \nabla \phi_1) = -\sum_{k=1,2} a_k i_{n,k} \tag{2.21}
$$

Because the concentration of salt $LiPF_6$ is much higher than the concentrations of H^+ and Mn^{2+} in the solution, we assume that the fluxes of H^+ and Mn^{2+} in the solution are not

affected by the electric field in the solution and their effects on the electric filed are negligible. Therefore, the migration term can be ignored in the material balance for H^+ and Mn^{2+}. The material balance for H^+ in the electrolyte is given by:

$$\varepsilon_{2,j}\frac{\partial c_{H^+}}{\partial t} = \nabla\cdot(D_{eff,H^+}\nabla c_{H^+}) + a_2 R_{s,1} + 2R_{s,2} - 4a_j R_{s,3},\ j = pos, sep \tag{2.22}$$

The material balance for Mn^{2+} in the electrolyte is given by:

$$\varepsilon_{2,j}\frac{\partial c_{Mn^{2+}}}{\partial t} = \nabla\cdot(D_{eff,Mn^{2+}}\nabla c_{Mn^{2+}}) + a_j R_{s,3},\ j = pos, sep \tag{2.23}$$

The material balance for H_2O in the electrolyte is given by:

$$\varepsilon_{2,j}\frac{\partial c_{H_2O}}{\partial t} = \nabla\cdot(D_{eff,H_2O}\nabla c_{H_2O}) - R_{s,2} + 2a_j R_{s,3},\ j = pos, sep \tag{2.24}$$

In equations (2.22)-(2.24), a_j and a_2 are zero in the separator region (j=*sep*) because the heterogeneous side reactions do not occur in the separator.

The governing equation for the volume fraction of the active material in the matrix phase which accounts for the acid induced Mn dissolution (side reaction in equation (2.10)) is given by:

$$\frac{\partial \varepsilon_{1,pos}}{\partial t} = -a_{pos} R_{s,3}\overline{V} \tag{2.25}$$

where $\overline{V}$ is the molar volume of LMO.

It is assumed that the total volume of the solid phase (including active material and inactive material) is not changed due to the side reaction shown in equation (2.10), that is, the active material degrades to the same volume of the inactive material.

It is assumed that the particles of the active material in the cathode are spheres. The material balance in the particles can be written using Fick's second law as follows:

$$\frac{\partial c_s}{\partial t} = \frac{1}{r^2}\frac{\partial}{\partial r}[D_s r^2 (\frac{\partial c_s}{\partial r})] \tag{2.26}$$

The intercalation/deintercalation kinetics is written in the form of Butler-Volmer equation:

$$i_{n,pos} = i_{0,Li}[\exp(\frac{\alpha_{a,Li}F}{RT}\eta_{Li}) - \exp(-\frac{\alpha_{c,Li}F}{RT}\eta_{Li})] \tag{2.27}$$

where η_{Li} is the over potential for Li intercalation/deintercalation reaction, $i_{0,Li}$ is exchange current of Li intercalation/deintercalation reaction, and expressed as:

$$i_{0,Li} = k_{Li} c_{s,surf}^{0.5} \left(c_{s,\max} - c_{s,surf}\right)^{0.5} c_{Li^+}^{0.5} \tag{2.28}$$

where k_{Li} is the reaction rate constant in the positive electrode , $c_{s,surf}$ is the surface concentration of Li^+ in the particles in the positive electrode, $c_{s,\max}$ is the maximum concentration of Li^+ in the particles in the positive electrode, and:

$$\eta_{Li} = \phi_1 - \phi_2 - U_p \tag{2.29}$$

where U_p is the equilibrium potential of Li intercalation/deintercalation reaction in cathode relative to a lithium reference electrode.

Moreover, the Li ion diffusion coefficient in the solid phase changes due to the plugging of pores and the formation of the film on the LMO particles surface in the cathode. The reduction of Li ion diffusion coefficient is given by an empirical equation which is similar to others in the literature.[23, 48] That is, the effective diffusion coefficient in the solid phase is given by:

$$D_S = D_{S,0}[1-(\frac{\varepsilon_{1,pos}^0 - \varepsilon_{1,pos}}{\varepsilon_{1,pos}^0})^{n_1}] \tag{2.30}$$

where $D_{S,0}$ is the initial solid phase diffusion coefficient, n_1 is an empirical factor which represents the effect of the formation of the film on the Li ion diffusion. n_1 can be obtained through experiments.

Boundary and initial conditions:

At the current collector/cathode interface (x=0):

The entire current density is carried by the solid phase, that is:

$$-\sigma_{eff} \left.\frac{\partial \phi_1}{\partial x}\right|_{x=0} = I_{app} \tag{2.31}$$

where I_{app} is the applied current density (the current divided by the projected electrode area), I_{app} is positive when charging the cell and is negative when discharging the cell.

For the same reason, the boundary condition for solution phase potential at x=0 is given by:

$$-\kappa_{eff} \left.\frac{\partial \phi_2}{\partial x}\right|_{x=0} = 0 \tag{2.32}$$

The fluxes for the solution species are zero at x=0:

$$-D_{i,eff}\left.\frac{\partial c_i}{\partial x}\right|_{x=0}=0, i=\mathrm{H_2O},\ \mathrm{Mn^{2+}},\ \mathrm{H^{+}},\ \mathrm{Li^{+}} \tag{2.33}$$

At cathode/separator interface ($x= L_P$), the total current density is carried by the solution phase, therefore the solid phase current density is zero. The solution phase current density and the species flux on the left side of the interface should be equal to those on the right, therefore:

$$-\sigma_{eff}\left.\frac{\partial \phi_1}{\partial x}\right|_{x=L_P}=0 \tag{2.34}$$

$$i_2\big|_{x=L_p^-}=i_2\big|_{x=L_p^+} \tag{2.35}$$

$$-D_{\mathrm{eff},pos}\left.\frac{\partial c_i}{\partial x}\right|_{x=L_p^-}=-D_{\mathrm{eff},sep}\left.\frac{\partial c_i}{\partial x}\right|_{x=L_p^+}, i=\mathrm{H_2O},\ \mathrm{Mn^{2+}},\ \mathrm{H^{+}},\ \mathrm{Li^{+}} \tag{2.36}$$

At the separator/Li metal interface ($x=L_P+L_S$), we set the potential at the Li metal electrode to be zero:

$$\phi_1\big|_{x=L_p+L_s}=0 \tag{2.37}$$

For the Li^+ ion, as the assumption above, the electric filed in the solution is not influence by H^+ and Mn^{2+}, therefore:

$$-D_{eff}\left.\frac{\partial c_{Li^+}}{\partial x}\right|_{x=L_p+L_s}=\frac{i_{b,Li}}{F}(1-t^+) \tag{2.38}$$

where,

$$i_{b,Li}=-k_{b,Li}c_{Li^+}^{0.5}[\exp(\frac{\alpha_a F}{RT}(-\phi_2))-\exp(-\frac{\alpha_c F}{RT}(-\phi_2))] \tag{2.39}$$

For H^+ and Mn^{2+}, it is assumed that when the cell is charged H^+ and Mn^{2+} are reduced at the anode surface as following reactions:

$$\begin{aligned} H^+ + e^- &= H_2 \\ Mn^{2+} + 2e^- &= Mn \end{aligned} \tag{2.40}$$

And, assuming for H^+ and Mn^{2+} there is no reduction/oxidation reactions when discharging cell,

$$-D_{eff}\left.\frac{\partial c_i}{\partial x}\right|_{x=L_p+L_s} = \frac{i_{b,i}}{F}, \quad i=H^+, Mn^{2+} \tag{2.41}$$

where

$$\begin{aligned} i_{b,i} &= k_{b,i}[-\exp(-\frac{\alpha_{c,i}F}{RT}(-\phi_2 - U_i))], && \text{Charge} \\ i_{b,i} &= 0, && \text{Discharge} \end{aligned} \tag{2.42}$$

where $k_{b,i}$ is the reaction rate constant for species *i* on the Li metal surface, and

$$U_i = U_i^{\theta} + \frac{RT}{z_i F}\ln[\alpha_i c_i], i=H^+, Mn^{2+} \tag{2.43}$$

where U_i^{θ} is the equilibrium potential of the reaction on the Li metal surface for species *i*, α_i is the activity coefficient for species *i* in the solution.

The flux of H_2O is zero at the Li metal surface:

$$\left.\frac{\partial c_{H_2O}}{\partial x}\right|_{x=L_P+L_S} = 0 \tag{2.44}$$

Current balance at $x=L_P+L_S$ is given by:

$$I_{app} = i_{b,Li} + i_{b,H^+} + i_{b,Mn^{2+}} \tag{2.45}$$

The boundary conditions for the solid phase diffusion are given by:

$$-D_s \left.\frac{\partial c_s}{\partial r}\right|_{r=0} = 0 \tag{2.46}$$

The initial conditions used in the model are:

$$\begin{aligned} &c_i = c_i^0, \quad i=\mathrm{H_2O},\ \mathrm{Mn^{2+}},\ \mathrm{H^+},\ \mathrm{Li^+} \text{ at } 0 \le x \le L_P + L_S \\ &c_s = c_s^0, \quad \text{at } 0 \le r \le R_{pos} \text{ and } 0 \le x \le L_P + L_S \\ &\varepsilon_{j,pos} = \varepsilon_{j,pos}^0,\ j = 1 \text{ at } 0 \le x \le L_P \end{aligned} \tag{2.47}$$

An energy balance is not included in this model because all the simulations are at a low C-rate where the temperature across the cell does not change significantly.

Table 2.1 shows the values of the electrode parameters. Table 2.2 shows the values of the side reaction parameters. The open circuit potential of the spinel cathode and other model expressions are presented in Appendix A.

2.3 Results and Discussions

The FORTRAN code was developed for the model and was solved using DARST (a DAE solver).[49] The model was used to investigate the effects of the cut off charge voltage, the carbon content in the cathode, the exchange current density of the solvent oxidation, and the reaction rate constants of the side reactions on the battery capacity fade.

Figure 2.1 shows the charge-discharge curves for selected cycle numbers (2, 25, and 50) of Li/LMO cell cycled at C/3 rate (1 C rate is 10.5 A cm^{-2}) and 55 ^oC between 3.5 and 4.5 V (vs Li/Li^+, all potentials below are relative to Li/Li^+ reference). As shown in Figure 2.1, the cell capacity decreases with repeated cycling. Also, the cell resistance

increases slightly with the cycle number which is indicated in the voltages of the plateaus in different cycles. The simulation results are very similar to experimental values in which the voltages of the plateaus corresponding to lithium ion extraction/insertion do not change very much with cycling despite capacity loss.[10, 31, 50]

The capacity loss with cycle number is shown in Figure 2.2 (solid line). The cell capacity is reduced by 16% after 50 cycles at C/3 and 55 ^{o}C between 3.5 and 4.5 V. For the same cycling conditions, the active material only decreases by 5% after 50 cycles as shown in the figure (dash line). Obviously, loss of active material amount cannot alone contribute to the overall capacity loss. Xia et al.[31] reported that the Li/LMO cell capacity decreases 19% after 50 cycles at C/3 and 50 ^{o}C between 3.5 and 4.5 V, which is similar to the 16% reported by our model. Also, they measured that the capacity losses caused by Mn dissolution are only 34% and 23% of the overall capacity loss at 50 ^{o}C and room temperature, respectively. In our model, about 30% of the total capacity loss is attributed to Mn dissolution which is close to the experimental values. However, in previous models the loss of active material due to Mn dissolution contributed significantly to the capacity losses.[34, 36]

As shown in Figure 2.2 (the plot corresponding to the axes on the right), the Li ion diffusion coefficient is decreased from 3.5e-15 m^2 s^{-1} (diffusion coefficient recorded at the beginning of second cycle) to less than 2e-15 m^2 s^{-1} after 50 cycles. The decrease of Li ion diffusion coefficient is another critical factor that leads to the capacity loss. The decrease of Li ion diffusion coefficient would result in cell polarization loss. The electrochemically inactive material generated from the Mn dissolution reaction and the precipitation of the electrolyte decomposition products both can cause the inactive film

growth on cathode. This film which is formed on the active material surface blocks Li ion transportation and decreases the effective solid phase diffusion coefficient. Those were reported in several experimental observations. Aurbach et al.[51] studied the impedance spectra of LMO cell polarized to 4.5 V with different time. The resistance of Li ion migration in the surface films was observed to increase from 171.9 Ω to 518.8 Ω after 120 min. This increase means that the kinetics of the electrode becomes sluggish. Zhang et al.[52] measured the Li ion diffusion coefficient as a function of cycle number for spinel LMO through an analysis of the Warburg impedance. The Li ion diffusion coefficient was found to decrease from 9.65e-10 cm^2 s^{-1} to 5.78e-10 cm^2 s^{-1} after 100 galvanostatic cycles with cut-off voltages of 3.4 V and 4.4 V. Das el al.[53] investigated the kinetics of Li ion diffusion in LMO thin film electrode by cyclic voltammetry as well as potential step chronoamperometry measurements. After repeated charge/discharge cycling, the Li ion diffusion coefficient was found to drop by almost one order of magnitude as compared to the original electrode. They reported that a surface electrolyte interface layer was formed on the electrode and this passive layer reduced the Li ion diffusion coefficient and lead to the observed capacity fading.

Figure 2.3 presents the rate dependent discharge curves of aged electrodes which have been cycled 50 times at C/3 rate and 55 ^oC between 3.5 and 4.5 V from a fresh cell. When the current density applied to the aged electrode reduces from C/3 to C/30, about half of the loss discharge capacity can be recovered again. This confirms that the loss of active material is not the only factor causing capacity fading, but the cell polarization is another important contribution. Kim et al.[33] observed the charge capacity of aged LMO electrode increase with a decrease in the current density, which had been stored in the

electrolyte 14 days at 60 ^{o}C. The capacity was about 20 mAh g^{-1} at 50 mA g^{-1}, but 75 mAh g^{-1} at 2 mA g^{-1}. The capacity measured at the lower rate (2 mA g^{-1}) is not much smaller than that (108 mA g^{-1}) obtained from the fresh cell at the same rate. They revealed that during high-temperature storage, the electrolyte decomposition products were deposited on the LMO surface. The depiction layer was highly resistive for electron and Li^{+} ion conduction and lead to a cell polarization and capacity loss.

The end of charge voltage (EOCV) is also a major factor in the battery cycle life. Figure 2.4 shows the variation of the cell capacity for 50 cycles with different cut-off charge voltages, namely 4.2, 4.3 and 4.5 V. Overcharging the cell to 4.5 V, the capacity fade is much more serious than that for the cells charged to 4.3 V as shown in the figure. In our model, the equilibrium potential of the solvent oxidation U_{side} is set to 4.2 V. Therefore, when the cell potential is above the $U_{side,}$ the solvent decomposition increases much faster. Also, more acid is generated. This overcharging damage has been reported in the literatures[31, 51, 54]. Aurbach et al. [51] observed that there was more Mn dissolution from the LMO electrode which was charged to 4.5 V compared to the electrode charged to 4.2 V. Also, the electrode cycled in the potential range of 3.8-4.5 V at high rates, the dissolution was much less than that for the electrode cycled at low rated in the same voltage region. They revealed that the Mn dissolution process related to an oxidation of the solution. Xia et al.[31] reported that the capacity decreased 19.2% for Li/LMO cell cycled between 3.5 and 4.5 V at C/3 and 50 ^{o}C after 50 cycles compared to 6.9% capacity loss cycled the cell between 3.5 and 4.23V while other conditions remain the same. In our current model, the capacity loss after 50 cycles is about 16% cycled cell between 3.5 and 4.5 V at C/3 and 55 ^{o}C. There is about 5% capacity loss when the cell is

cycled between 3.5 and 4.3 V. Our simulation results are similar to the experimental data mentioned above.

In most of Li-ion cells, the carbon material has been used to improve electrical conductivity between the active particles in the cathode. The solvent oxidation currents were found to be roughly proportional to the surface area of the composite electrode. Since carbon used as conductor in the cathode has higher surface area compared to the active material, the surface area of the composite electrode is mainly dominated by that of carbon even though it is in a small quantity. In this model, the carbon content is related to cell performance by providing reaction sites for solvent oxidation through equation (19). Figure 2.5 shows the variation of capacity with different carbon contents in the composite cathode for the 50 cycles. As shown in figure, when the carbon content is decreased from 10% to 3%, the capacity loss is decreased from 16% to 6%. Also, the capacity loss after 50 cycles depends almost linearly on the carbon content. Guyomard et al. [37] determined that the variation of the irreversible capacity followed a straight line due to electrolyte oxidation at 55 ^{o}C as a function of the carbon content (weight percent) in the composite electrode. Jang at al.[55] also reported that both the extent of solvent oxidation and the amount of Mn dissolution are proportional to carbon surface area. It should be mentioned that the effect of the carbon content on cell resistance is not considered in our current model. When carbon content is lower, the internal resistance increases much larger when the cell is aged. Consequently, the carbon content can be optimized by the tradeoff between the cell capacity loss and the polarization loss.

The adjustable parameters in the study mentioned above, such as the reaction rate constants (k_2, k_3) of side reactions were mainly fixed. For a better understanding of the

contribution of different side reactions to the cell capacity fade, various parameters dominating the side reactions need to be investigated. The discussions shown below include the effects of the exchange current density of solvent oxidation, $i_{0,s}$, the reaction rate constant of $LiPF_6$ decomposition, $k_{2,}$ and the reaction rate constant of LMO dissolution due to the acid attack, $k_{3,}$ on the capacity fade of the Li/LMO half cells which are cycled between 3.5 and 4.5 V with current rate of C/3 at 55 ^{o}C.

Figure 2.6 shows the effect of the exchange current density for the solvent oxidation reaction on the cell capacity fade. The stabilities of the solvent components (DME, EC, DMC, PC) in the cell are highly different. For example, ethers are easily oxidized whereas carbonates are relatively stable. Different compositions of the solvent species may lead to different values in $i_{0,s}$. The larger values $i_{0,s}$ mean that the electrolyte is less stable and the rate of the electrolyte oxidation increases during the cell cycling in the same voltage region. Consequently, the Mn dissolution and the capacity loss increase. As shown in Figure 6, the capacity loss is more than 5 times higher by changing $a_{2,set}i_{0,s}$ from 1 A m^{-3} to 30 A m^{-3}. A similar capacity loss tendency has been noted in many papers. For example, Jang et al[11] observed that Li/LMO cells lost their capacity at faster rates in ethers and the capacity loss rate was slower in the carbonate-containing electrolytes. The Li/LMO cells in 1 M $LiClO_4$/PC/THF electrolyte lost half of its capacity after 50 cycles between 4.3 and 3.6 V. At the same cycling condition, the cells capacity in 1 M $LiClO_4$/PC/DEC only decreases about 10%. They explained that protons generated from solvent oxidation play an important role in Mn dissolution and ethers are relatively easier to be oxidized than carbonates. Therefore, the capacity loss in ethers is more significant compared to that in carbonates.

Water is undesirable for lithium ion batteries because it results in decompositions of the cell components, such as the electrolyte and the SEI film on the anode. However, there is often about ten of ppm water in the commercial electrolyte used in lithium ion cells. Moreover, many cathode materials are highly absorbent, and they draw a large amount of water into batteries. In addition water can be generated from a parasitic reaction (such as the side reaction shown in equation(2.10)) as discussed in Wang et al.[12] Figure 2.7 presents the effect of the reaction rate constant of the conductive salt decomposition, k_2, on the capacity fade at 55 ^{o}C. The simulation results in Figure 2.7 show that an increase in the value of k_2 even by one order of magnitude dramatically accelerates the capacity loss which indicates that the variation of k_2 value has a significant influence on the cell capacity. That is, a high value of k_2 means that the rate of conductive salt decomposition with water will increase and more acid will be formed. That not only causes the resistance increase in the solution phase but also leads to more Mn dissolution. Therefore, a stable salt which has a small value of k_2 is more attractive than $LiFP_6$ for high temperature application. Likewise, water or acid scavenger additive such as zeolite would enhance cell performance, because they would absorb water or acid and reduce the apparent acid generation rate. Sano et al.[56] reported that substituting part of $LiPF_6$ in the electrolyte with $Li(C_2F_5SO_2)_2N$ (LiBETI) improved the LMO cell capacity retention when cycled at high temperature. LiBETI is not as facile as $LiPF_6$ to hydrolyze and produce acid. Therefore, it helps suppress acid formation from the hydrolysis. They also reported that phosphate additives improved the performance of LMO cells when cycled at high temperature.

Figure 2.8 shows the influence of the reaction rate constant of LMO dissolution due to acid attack, k_3, on the cell capacity fading. By reducing k_3 from 2e-10 m s^{-1} to 2e-12 m s^{-1}, the capacity loss is reduced by 8 times (from 16% to 2%) for 50 cycles. This indicates that the stability of LMO in acid solution is very important for the cell performance operated at high temperature. When k_3 is changed from 2e-9 m s^{-1} to 2e-8 m s^{-1}, by contrast, the increase of the capacity loss is not significant. This indicates that Mn dissolution is controlled not only by the reaction rate constant but also by the acid supply. Coating and doping are effective ways to prevent the acid attacking on the LMO electrode. The stability of LMO in the acid solution increases and the value of k_3 becomes smaller. Wang et al.[12] reported that the Li_2CO_3 coated spinel LMO had better storage performance at elevated temperature than the original spinel. Deng et al.[57] observed that after Li-doped, the stability of spinel soaked in the solution at the elevated temperature increases, that is, the Mn dissolution from a Li-doped LMO sample decreases. At the same time, the cycling performance was improved significantly and the capacity retention ratio after 50 cycles at 60 ^{o}C was improved to more than 90%.

2.4 Conclusions

A capacity fade model for a spinel based cathode was developed in this chapter. The model considers the capacity loss due to the acid attack and the SEI film formation. The acid is generated from the decomposition of the solvent and the $LiPF_6$ solute, and then attacks the active material which leads to Mn dissolution and the formation of a SEI film on the cathode. The SEI film built on the cathode surface causes a decrease in the solid phase diffusion coefficient and causes the cell polarization loss. Case studies show that the end of charge voltage (EOCV) is a critical operation factor for capacity fading of the

spinel based cathode. The effects of side reactions on cell performance are also investigated qualitatively. This study reveals that the stabilities of electrolyte and the spinel LMO are important for the cell life when the cell is cycled at the elevated temperature.

In this model, it was assumed that the Mn dissolution depends only on the concentration of acid species. This assumption may not represent the practical situation well. Consequently, a mechanism for the Mn dissolution at different states of charge will be implemented in a future model. A Carbon/LMO full cell model including the Mn^{2+} ion deposition on the carbon anode surface will also be included in a future model.

Table 2.1. Electrode parameter values

Parameter	Value	Parameter	Value
L_p	50 e-6 m	k_{Li}	1e-5 A m^{-2}
L_s	50 e-6 m	$k_{b,Li}$	6.1e-6 A m^{-2}
$\varepsilon_{2,pos}$	0.444	t_+	0.37
$\varepsilon_{2,sep}$	0.724	D_s	6e-15 m^2 s^{-1}
$\varepsilon^0_{1,pos}$	0.43	σ	10 S m^{-1}
R_{pos}	4.7 e-6 m	$\alpha_{a,Li}$	0.5
Brugg_{pos}	1.5	$\alpha_{c,Li}$	0.5
Brugg_{sep}	1.5	$c^0_{Li^+}$	2000 mol m^{-3}
R	8.314 J mol^{-1} K^{-1}	θ^0	0.3
F	96487 C $equiv^{-1}$	$c_{s,max}$	22040 mol m^{-3}
T	55 ^oC	I_{app}	3.5 A m^{-2}
$\overline{V}$	4.1389e-5 m^3 mol^{-1}		

Table 2.2. Parameter of side reactions

Parameter	Value	Parameter	Value
U_{side} [a]	4.2 V	c^0_{H2O} [a]	4 mol m^{-3}
$a_{2,set}i_{0,s}$ [a]	10.0 A m^{-3} *	c^0_{H+} [a]	4 mol m^{-3}
$\alpha_{a,s}$ [a]	0.5	c^0_{Mn2+} [a]	0
k_2 [b]	7.13e-10 m^6 mol^{-2} s^{-1} *	$k_{b,H+}$ [a]	1.0e-18 A m mol^{-1}
k_3 [a]	2.0e-10 m s^{-1}*	$k_{b,Mn2+}$ [a]	1.0e-11 A m mol^{-1}
n_1 [a]	0.12	α_{H+} [a]	0.01
$X_{c,set}$ [a]	10%	α_{Mn2+} [a]	0.1
X_c [a]	10 %*	$U^{\theta}_{H^+}$ [a]	2.5 V
D_{H2O} [c]	3e-9 m^2 s^{-1}	$U^{\theta}_{Mn^{2+}}$ [a]	1.5 V
D_{H+} [c]	5e-9 m^2 s^{-1}	D_{Mn2+} [c]	0.72e-9 m^2 s^{-1}

[a] Assumed

[b] From Ref. 28

[c] Referred to diffusion coefficients of ions at infinite dilution in water solvent

* Except specification

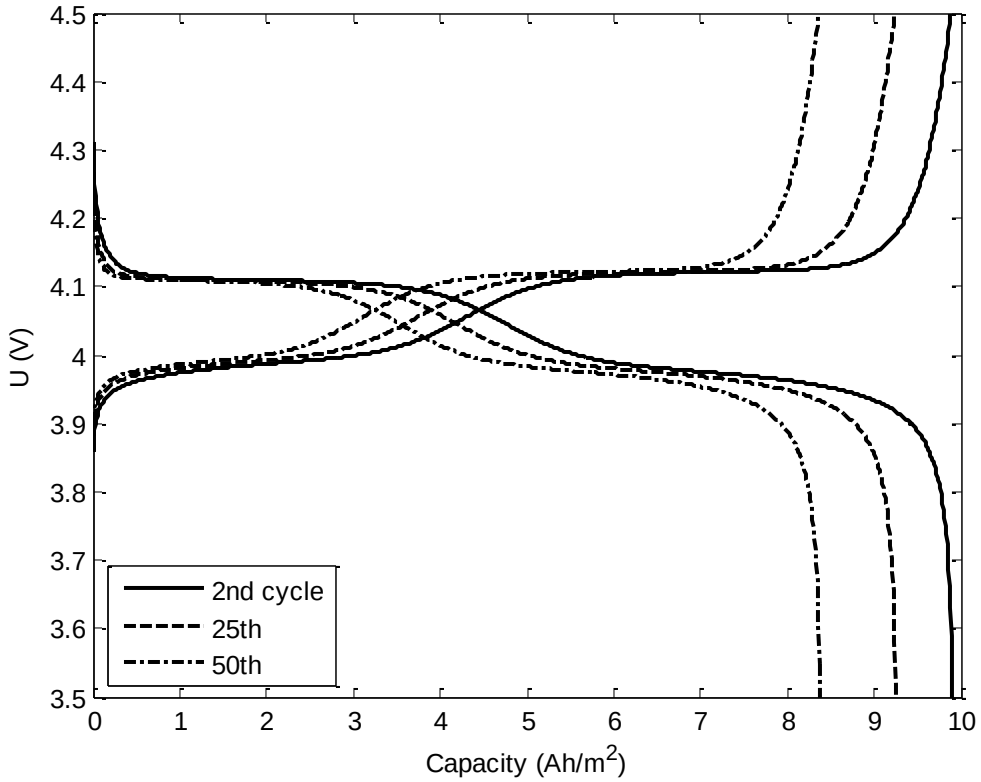

Figure 2.1 The 2nd, 25th, 50th charge and discharge curves of Li/LMO cell. The cell is cycled at C/3 rate and 55 ^{o}C between 3.5 and 4.5 V

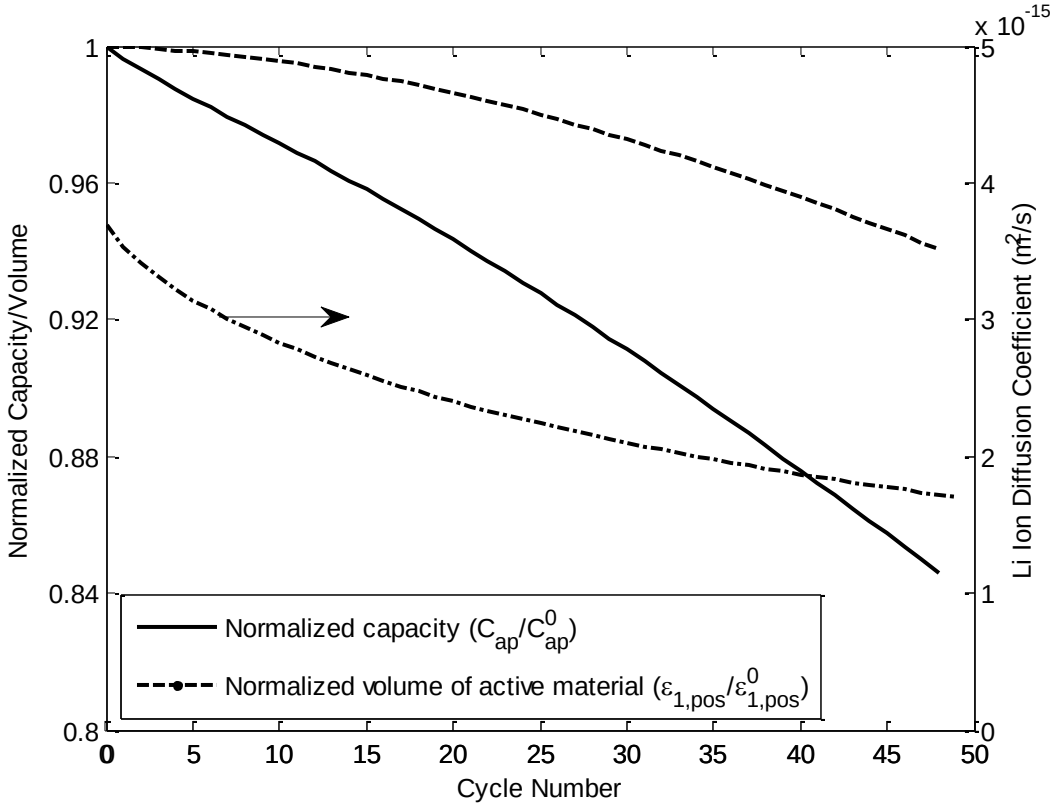

Figure 2.2 Normalized cell capacity, normalized volume fraction of active material and Li ion diffusion coefficient (the plot corresponding to the axes on the right) change with cycle number for Li/LMO cell. The cell was cycled at C/3 rate and 55 ^{o}C between 3.5 and 4.5 V

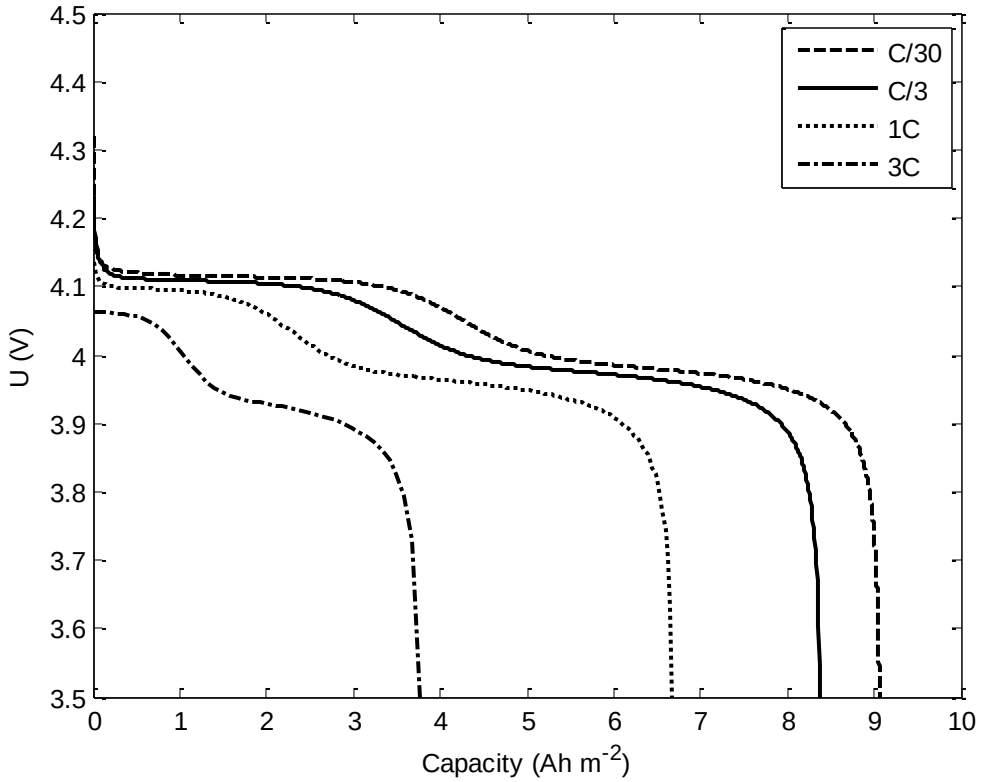

Figure 2.3 Discharge curves of aged Li/LMO cell at different current densities (C/30, C/3, 1C and 3 C) between 3.5 and 4.5 V at 55 ^{o}C. Prior to each discharge, the cell has been cycled 50 times at C/3 and 55 ^{o}C rate between 3.5 and 4.5 V from a fresh cell.

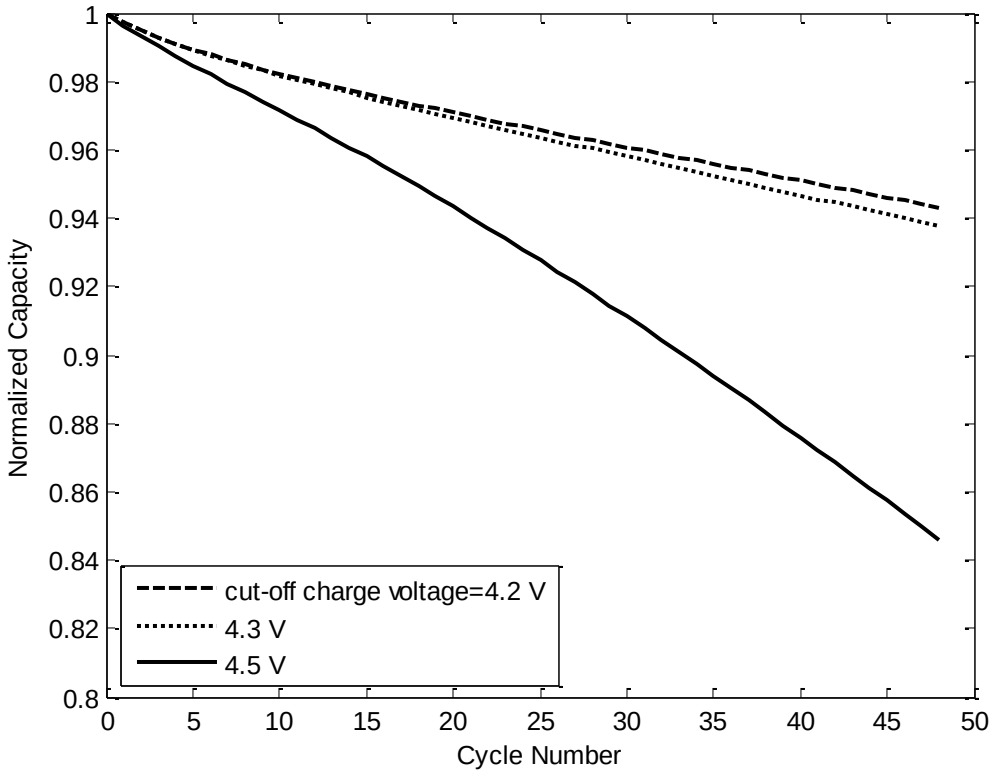

Figure 2.4 Normalized capacities as functions of cycle number for different end of charge voltages (4.2, 4.3 and 4.5 V). The Li/LMO cell is cycled at C/3 rate and 55 ^{o}C, and the end of discharge voltage is 3.5 V.

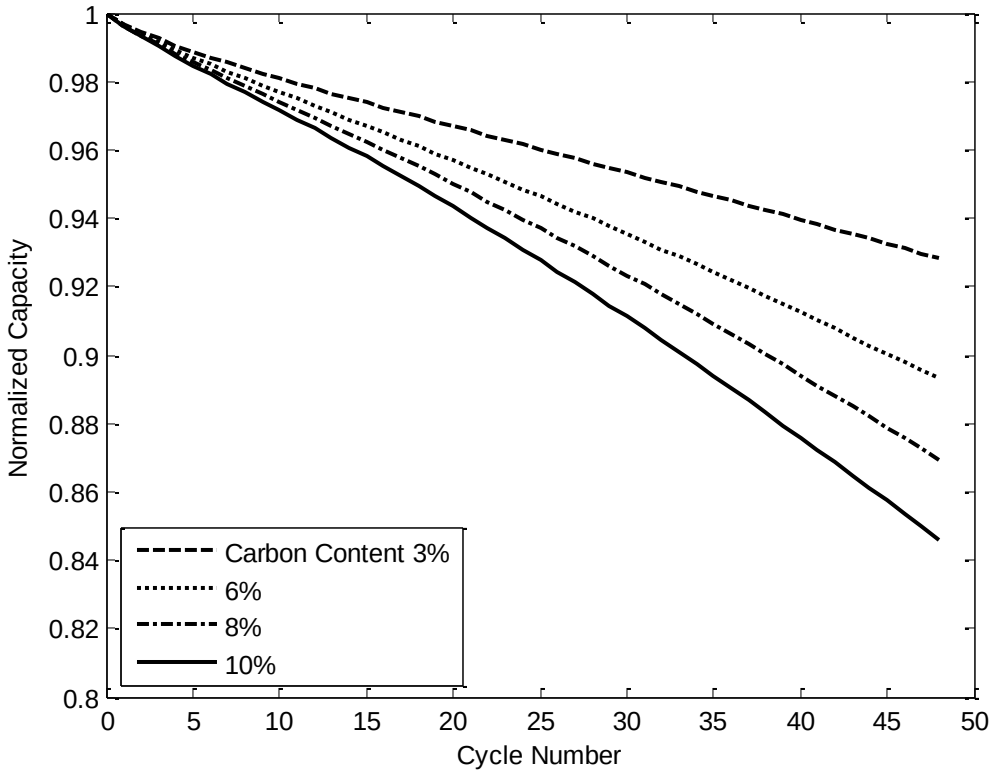

Figure 2.5 Normalized capacities as functions of cycle number for different carbon contents (3%, 6%, 8%, 10%, weight percent) in composite electrode. The Li/LMO cells are all cycled at C/3 and 55 ^{o}C rate between 3.5 and 4.5 V

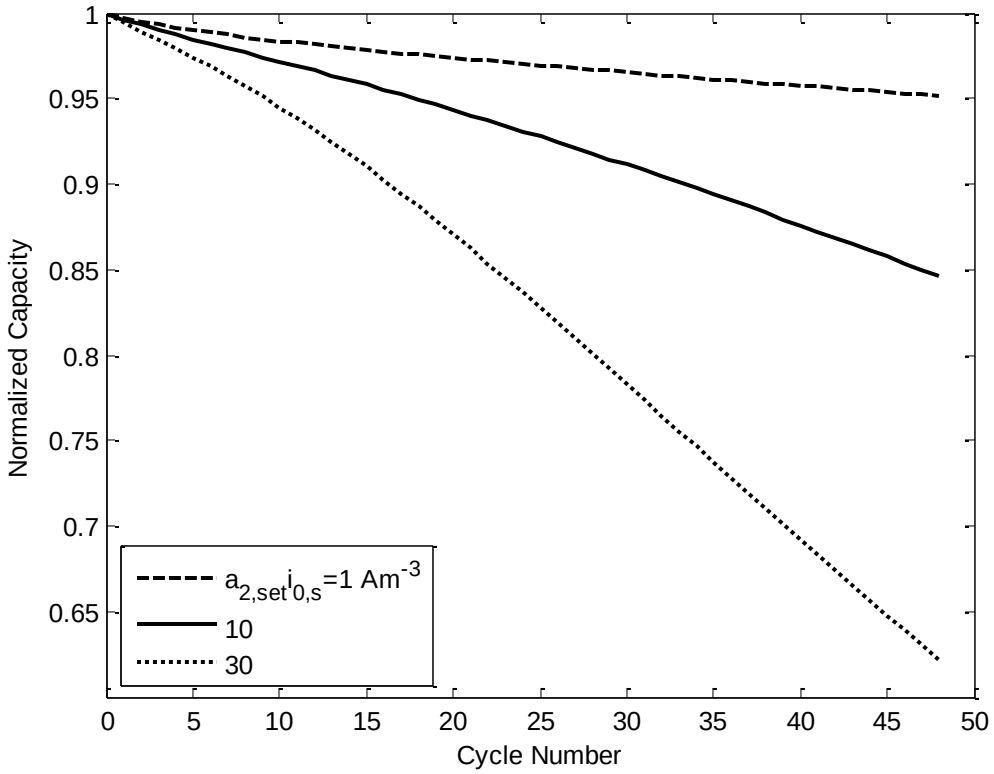

Figure 2.6 Normalized capacities as functions of cycle number for different solvent oxidation exchange current densities, $a_{2,set}i_{0,s}$, (1, 10 , 30 A m^{-3}). The Li/LMO cells are all cycled at C/3 rate and 55 ^{o}C between 3.5 and 4.5 V

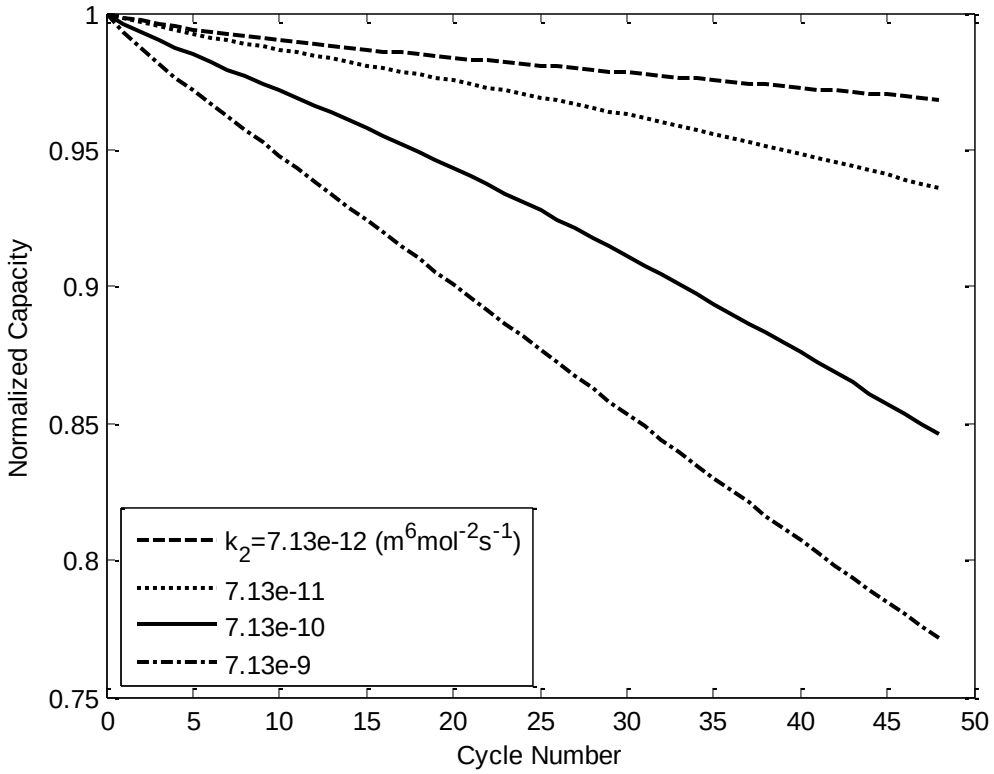

Figure 2.7 Normalized capacities as functions of cycle number for different $LiPF_6$ decomposition reaction rate constant, k_2, (7.13e-12, 7.13e-11, 7.13e-10, 7.13e-9 m^6 mol^{-2} s^{-1}). The Li/LMO cells are all cycled at C/3 rate and 55 ^oC between 3.5 and 4.5 V

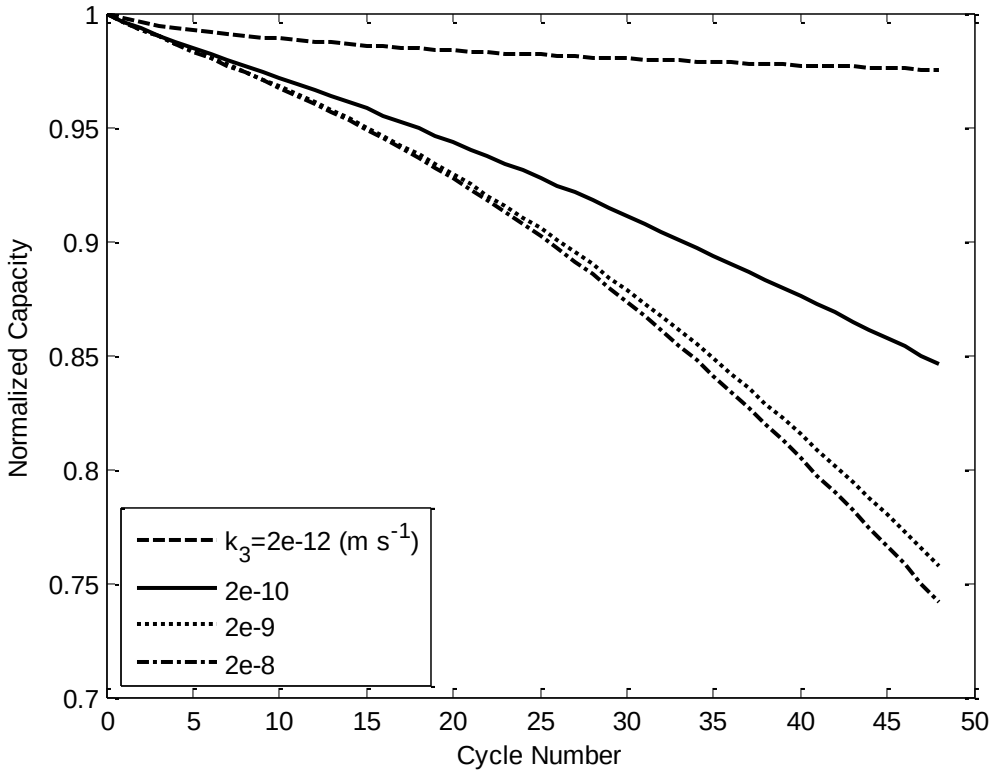

Figure 2.8 Normalized capacities as functions of cycle number for different reaction rate constants of LMO dissolution due to acid attack, k_3, (2e-12, 2e-10, 2e-9, 2e-8 m s^{-1}). The Li/LMO cells are all cycled at C/3 rate and 55 ^{o}C between 3.5 and 4.5 V

3 Simulation and Analysis of Stress in a Li-ion Battery with a Blended $LiMn_2O_4$ and $LiNi_{0.8}Co_{0.15}Al_{0.05}O_2$ Cathode

3.1 Introduction

Spinel $LiMn_2O_4$ (LMO) is one of the most attractive positive electrodes for high power applications such as hybrid/plug-in hybrid electrical vehicles (HEV/PHEVs). It shows great benefits in the area of cost, safety and power density, which are major concerns of large format applications in the automotive industry. However, this spinel material exhibits serious capacity fade during cycling or storage at elevated temperature which makes it less competitive with other cathode materials.[58] Recent studies have revealed that capacity fade in spinel LMO cathodes is mostly due to manganese (Mn) dissolution and its toxic effect on the carbon anode.[9, 13, 59] There are at least two possible reasons for the Mn dissolution: (1) acid attack and a disproportionation reaction of Mn(III) on the particle surface;[3, 10, 60] (2) the instability of the two-phase structure in the charged state which leads to the loss of MnO and the dissolution of Mn(II) to form a more stable single-phase structure.[31]

Several improvements have been made to increase the long term stability of the LMO based cells by using surface treatment or element substitution. For example, Amatucci et al.[61] have investigated the effects of modifying the surface of LMO on the cell performance at high temperatures. The surface improvement helps to reduce Mn dissolution and retain capacity. Doped spinel $LiMn_{2-x}M_xO_4$ (where M=Li, Co, Cr, Ni etc.) materials have also been reported to be effective for the improvement of the cell high

temperature performance.[52, 62-64] The benefit of doping elements in LMO has been attributed to the stabilization of the spinel structure. Among them, the doped material with lithium substitution of Mn sites has higher theoretical capacity than others because of the light element lithium, but the doped material retain the native low capacity of LMO. In order to increase the reversible capacity after the cation doping while keeping the other electrochemical performance, F^- ions were introduced in place of O^{2-} ions.[65, 66] Unfortunately, the cost for the production of the doped materials is significantly high.

A promising approach was first provided by Numata et al. to improve the capacity retention for LMO based electrodes by adding $LiNi_{0.8}Co_{0.2}O_2$.[30] They found that both the Mn dissolution from the LMO and the acid generation decreased with the addition of $LiNi_{0.8}Co_{0.2}O_2$. Myung et al.[67] investigated the behavior of the electrode with the LMO and $LiNi_{0.8}Co_{0.15}Al_{0.05}O_2$ (NCA) mixture. They found that a cell with the mixed electrode had better cycle performance at elevated temperature than a cell with a pure LMO electrode. In addition, the capacity of the LMO based electrode has been enhanced by adding high capacity NCA. Recently, Tran et al.[68] reported on the electrochemical and thermal behavior of LMO and NCA blended electrodes. Their results indicated that the NCA addition increased the capacity of blends and reduced the Mn dissolution from the spinel, but harmed the rate capacity; On the other hand, with the existence of LMO the heat generation from the blends is less than that from the pure NCA. According to their study, blends with 33.3 wt% NCA have the best behavior. Manthiram et al.[69] studied the suppression of the Mn dissolution in spinel cathodes by mixing LMO or its doping derivatives with layered oxide cathodes such as: $LiCoO_2$ and $LiNi_{0.85}Co_{0.15}O_2$. They observed that $LiCoO_2$ was more effective than $LiNi_{0.85}Co_{0.15}O_2$ in improving the storage

and cycle performance of LMO based electrodes. Smith et al.[70] showed that the addition of $Li[Ni_{1/3}Mn_{1/3}Co_{1/3}]O_2$ to the LMO electrode produced a great improvement in the capacity retention. Also, it was found that the $Li[Ni_{1/3}Mn_{1/3}Co_{1/3}]O_2$ helped to reduce the Mn dissolution from the LMO electrode. Now, Li-ion batteries with LMO mixed with other insertion active material as cathodes have been commercialized such as Samsung SDI Li-ion batteries.

The mechanical degradation under cycling is one of the most important failure mechanisms of modern Li-ion batteries. It has been reported that the fractures and cracks exist in several electrode materials after Li insertion/extraction.[15, 16, 24, 71] For example, Lim et al.[16] have observed an evident disruption in the LMO particle after electrochemical cycling. There is about 6.5% volume change when the LMO is lithiated from empty state to full state.[72] However, the particle volume change inside particle is not uniform. This gives rise to stress and produces cracks or fractures in the particle. Furthermore, the particle fracture will generate more fresh active material surface on which the new solid electrolyte interface (SEI) film is formed. In the meanwhile, the particle fracture can also lead to loss of connection of the active material particle to the conductor.[18]

Mathematical models have been largely applied to investigate the stress generation and the effect of stress on battery degradation. Christensen et al.[73, 74] developed an integrated model based on theories of transport and elasticity to simulate the stress inside active material particles. Zhang et al.[75] studied the intercalation-induced stress in LMO particles by considering the intercalation-induced stress as being analogous to thermal stress. Their approach showed similar results to those of Christensen et al.. Without

considering the stress-driven diffusion in Zhang et al's approach, Cheng et al.[76] obtained an analytical solution for the generation of stress in a spherical particle under galvanostatic and potentiostatic operation.

Unlike the studies above on single particles only, there are several papers on the stress generation in a porous composite electrode. Garcia et al.[77] developed a two-dimensional model with particle distribution to compute stress in the porous electrode. Also, the model account for the potential and Li-ion concentration distribution in the solution. However, this model is very computationally intensive and the stress-driven diffusion has been ignored. Golmon et al.[78] combined the mechanical equation and porous electrode theory (the pseudo two dimensional (P2D) model) together to investigate the stress distribution in porous electrode. They applied homogenization techniques to relate the parameters between the micro-scale and the macro-scale. Similarly, Renganathan et al.[79] studied the stress generation in a $LiCoO_2$/Cabon battery with considering the phase change in the $LiCoO_2$. Christensen [80] simulated the stress generation in porous electrode by incorporated the model for stress generation in single particle [73, 74] to the P2D model. Recently, Bower et al.[81] proposed a finite –strain elastic-plastic model to predict the variation of stress and electric potential in a one-dimensional half-cell.

However, the stress generation of an electrode with multiple active materials has never been studied by mathematical model. For a better understanding of the properties of Li-ion batteries with blended material cathodes, we present a study of the mechanical behavior of electrodes made from mixing LMO and NCA through theoretical modeling for the first time. The mechanical equations capturing the stress generation in the

spherical particle are incorporated into classical the P2D model together. To elucidate the effect of mixing, the simulation is conducted and compared to a pure LMO electrode and the blended electrode with LMO and NCA. Simulation results for a mixed electrode show that the stress generated in the LMO particles is significantly reduced at the end of discharge due to adding NCA to the electrode. This stress reduction might partially explain why experiment invesigations show that the performance of the LMO based electrodes can be improved by adding NCA.We also investigate the mixing ratio on the stress generation of the blended electrode. Simulations for mixed electrodes with different blend ratios show that the reduced stress region increases by increasing the NCA ratio.

3.2 Model Development

In this study, we have combined P2D model and mechanical equations to study the stress generated due to Li insertion into/extraction from the active material particles in a lithium ion battery. This approach is similar to Renganathan et al.'s work to study the $LiCoO_2$/Carbon battery [79], but we have extended that work to electrodes with multiple active materials in the cathode. Furthermore, because no phase change is considered during Li insertion into/extraction from the active material particles, we could express the stress profile as function of concentration. To obtain the stress profile in the P2D model, we only modified the diffusion equation in the classic P2D model, which is shown in detail below.

The Li-ion battery considered in this study consists of three regions: a positive electrode (pure LMO or LMO mixed with NCA), a separator, and a carbon negative electrode as shown in Figure 1. The full cell is chosen here, because it is more closed to

the practical situation where the cell encounters. For an electrode that has more than one active material, it is assumed that the materials in the electrode are well mixed and their properties (such as: diffusion coefficients, reaction rate constants and so on) remain the same as those in a pure material electrode. The parameters for the mixed positive electrode used in this model were obtained from the work by Albertus et al.[82], in which the electrochemical behavior of a mixed cathode half-cell was simulated. In the following, we will briefly introduce the mechanical equations and the porous electrode model equations.

Mechanical stress model:

In this work, the stress generated due to Li-ion intercalation/deintercalation process is calculated using an approach similar to that due to volumetric thermal expansion. The thermal stress analysis of an isotropic media can be described by Hooke's law with additional thermal expansion term[83]:

$$\varepsilon_{ij} = \frac{1}{E}[(1+\nu)\sigma_{ij} - \nu\sigma_{kk}\delta_{ij}] + \alpha\Delta T\delta_{ij} \tag{3.1}$$

where ε_{ij} and σ_{ij} represent the strain and stress tensor components, respectively; E is Young's modulus, ν is Poisson's ratio, δ_{ij} is Kronecker delta, α is the thermal expansion coefficient, and ΔT represents the temperature difference from the original value.

Analogously, in the case of small deformation, a stress-strain relationship including a concentration diffusion in a isotropic media nt can be represented as [84]:

$$\varepsilon_{ij} = \frac{1}{E}[(1+\nu)\sigma_{ij} - \nu\sigma_{kk}\delta_{ij}] + \frac{\Delta c\Omega}{3}\delta_{ij} \tag{3.2}$$

where Ω is the partial molar volume and $\Delta c=c-c_0$ is the concentration change of the diffusing species from original value, c_0. c is the concentration of the diffusing species.

For a spherical particle, there are only two independent components in the stress tensor: the radial component (σ_r) and the tangential component (σ_t). Therefore, the equilibrium condition for the stress tensor in a particle is simplified as follows [75]:

$$\frac{d\sigma_r}{dr}+\frac{2}{r}(\sigma_r-\sigma_t)=0 \tag{3.3}$$

Also, strain-stress relations can be writes as according to Eq.(3.2) for a spherical particle[75],

$$\begin{aligned}\varepsilon_r &= \frac{1}{E}(\sigma_r-2\nu\sigma_t)+\frac{\Omega}{3}\Delta c \\ \varepsilon_t &= \frac{1}{E}[\sigma_t-\nu(\sigma_t+\sigma_r)]+\frac{\Omega}{3}\Delta c\end{aligned} \tag{3.4}$$

The stresses can be written as a function of strains,

$$\begin{aligned}\sigma_r &= \frac{E}{(1+\nu)(1-2\nu)}[(1-\nu)\varepsilon_r+2\nu\varepsilon_t-(1+\nu)\frac{\Delta c\Omega}{3}] \\ \sigma_t &= \frac{E}{(1+\nu)(1-2\nu)}[\nu\varepsilon_r+\varepsilon_t-(1+\nu)\frac{\Delta c\Omega}{3}]\end{aligned} \tag{3.5}$$

Also, strains can be related to the displacement u as following:

$$\begin{aligned}\varepsilon_r &= \frac{du}{dr} \\ \varepsilon_t &= \frac{u}{r}\end{aligned} \tag{3.6}$$

By substituting Eq.(3.6) into Eq.(3.5), the stress tensor can be expressed in terms of displacement *u* as follows:

$$\sigma_r = \frac{E}{(1+v)(1-2v)}[(1-v)\frac{du}{dr} + 2v\frac{u}{r} - (1+v)\frac{\Delta c\Omega}{3}]$$
$$\sigma_t = \frac{E}{(1+v)(1-2v)}[v\frac{du}{dr} + \frac{u}{r} - (1+v)\frac{\Delta c\Omega}{3}] \quad (3.7)$$

Substitute Eq.(3.7) into the equilibrium condition (Eq.(3.3)) yields the displacement equation which is shown as following:

$$\frac{d^2u}{dr^2} + \frac{2}{r}\frac{du}{dr} - \frac{2u}{r^2} = \frac{1+v}{1-v}\frac{\Omega}{3}\frac{dc}{dr} \quad (3.8)$$

Integrating Eq.(3.8) yields:

$$\frac{du}{dr} + 2\frac{u}{r} = \frac{1+v}{1-v}\frac{\Omega}{3}c + Z_1 \quad (3.9)$$

Integrating Eq.(3.9) yields:

$$u = \frac{1}{r^2}(\int \frac{1+v}{1-v}\frac{\Omega}{3}cr^2dr + \frac{Z_1r^3}{3} + Z_2) \quad (3.10)$$

where Z_1 and Z_2 are integration constants. These two constants can be obtained from the two boundary conditions: the radial stress is zero on the particle surface ($r=R_0$)

$$\sigma_r\Big|_{(r=R_0)} = 0 \quad (3.11)$$

and the stress remains finite at the particle center ($r=0$), that is:

$$\frac{d\sigma_r}{dr}\Big|_{(r=0)} = 0 \quad (3.12)$$

Substituting the solution for *u* into Eq.(3.5), results in the following expressions for the two stress components:

$$\sigma_r = \frac{2\Omega E}{3(1-v)}[\frac{1}{R_0^3}\int_0^{R_0} cr^2 dr - \frac{1}{r^3}\int_0^r c\zeta^2 d\zeta]$$
$$\sigma_t = \frac{\Omega E}{3(1-v)}[\frac{2}{R_0^3}\int_0^{R_0} cr^2 dr + \frac{1}{r^3}\int_0^r c\zeta^2 d\zeta - c] \quad (3.13)$$

where ζ is integration variable.

Finally, the hydrostatic stress, σ_h, is defined and given as follows[75, 84]:

$$\sigma_h = \frac{\sigma_r + 2\sigma_t}{3} = \frac{2\Omega E}{9(1-v)}(\frac{3}{R_0^3}\int_0^{R_0} cr^2 dr - c) \quad (3.14)$$

Porous electrode model:

The porous electrode model (the pseudo two dimensional (P2D) model) has been applied to simulate the behavior of Li-ion batteries in many literatures.[19, 20, 85] The mass balance and the charge balance are considered in the both solution phase and the solid phase. We only briefly introduce the model here as follows. A detailed explanation of the porous electrode models can be found elsewhere.[19, 20, 85]

The mass balance for Li^+ in the electrolyte is given as follows:

$$\varepsilon_{2,j}\frac{\partial c_{Li^+}}{\partial t} = -\nabla(-D_{eff,Li^+,j}\nabla c_{Li^+}) + \frac{1-t^+}{F}I_j,\ j = p,s,n \quad (3.15)$$

where $\varepsilon_{2,j}$ is the porosity in cell component *j* (*j*=*p* for the cathode, *j*=*s* for the separator, and *j*=*n* for the anode), c_{Li^+} is the concentration of Li^+, $D_{eff,Li^+,j}$ is the effective diffusivity of Li^+ in the electrolyte, t^+ is the transport number of Li^+, F is Faraday's

constant, and I_j is the local total current density (A m^{-3}). The potential in the solid phase, ϕ_1, is given by Ohm's law as follows:

$$\nabla \cdot (-\sigma_{eff,j} \nabla \phi_1) = -I_j, \; j = p, n \tag{3.16}$$

where $\sigma_{eff,j}$ is the effective conductivity in the solid phase.

The solution phase potential, ϕ_2, is given by:

$$\nabla \cdot (\kappa_{eff,j} \nabla \phi_2 - 2\frac{\kappa_{eff,j} RT(1-t^+)}{F}(1+\frac{\partial \ln f}{\partial \ln c_{Li^+}})\nabla \ln c_{Li^+}) = I_j, \; j = p, s, n \tag{3.17}$$

where $\kappa_{eff,j}$ is the effective conductivity in the solution phase, R is the gas constant, T is the temperature, f is the ionic activity coefficient.

The local total current density, I_j, is the sum of current densities for all types of particles

$$I_j = \sum_{k}^{k_j} a_{k,j} i_{k,j}, \; j = p, n \tag{3.18}$$

where k_j is particle types in region j. In the positive electrode, there are two types of particles: LMO and NCA; in the negative electrode, there is only one particle type. $a_{k,j}$ is the specific surface area of types particle k and is defined as

$$a_{k,j} = \frac{3\varepsilon_{1,k,j}}{R_{s,k,j}} \tag{3.19}$$

where $\varepsilon_{1,k,j}$ is the volume fraction of the particles type *k* in region *j*, and $R_{s,k,j}$ is the radius of the particle type *k*. $i_{k,j}$ is the local transfer current for the particles type *k* and is described by the Butler-Volmer expression as follows:

$$i_{k,j} = i_{0,k,j}[\exp(\frac{\alpha_{a,Li}F}{RT}\eta_{k,j}) - \exp(-\frac{\alpha_{c,Li}F}{RT}\eta_{k,j})] \tag{3.20}$$

where $i_{0,k,j}$ is the exchange current density for particles type *k* in region *j* and is defined as:

$$i_{0,k,j} = Fk_{Li,k,j}c_{surf,k,j}^{0.5}\left(c_{\max,k,j} - c_{surf,k,j}\right)^{0.5}c_{Li^+}^{0.5} \tag{3.21}$$

where $k_{Li,k,j}$ is the reaction rate constant for the particles type *k*, $c_{surf,k,j}$ is the surface concentration of Li^+ for the particles type *k*, $c_{max,k,j}$ is the maximum concentration of Li^+ in the particles type *k*. The over-potential for particle type *k* in region *j* is given by:

$$\eta_{k,j} = \phi_1 - \phi_2 - U_{k,j} - i_{k,j}R_{conc,k,j} \quad \eta_{k,j} = \phi_1 - \phi_2 - U_{k,j} - i_{k,j}R_{conc,k,j} \tag{3.22}$$

where $U_{k,j}$ is open-circuit potential for particle type *k* in region *j*, $R_{conc,k,j}$ is the contact resistance between the bulk conductor and the surface of particle type *k*. The effective properties are discussed and presented in the Appendix B.

Diffusion in the solid phase:

The diffusion equation is modified by including the stress-driven diffusion. The pore wall flux, J_k, for particles type *k* including the stress-driven diffusion can be expressed as following[75, 84]:

$$J_k = -D_{s,k}(\nabla c_{s,k} - \frac{\Omega c_{s,k}}{RT}\nabla\sigma_{h,k}) \tag{3.23}$$

where $D_{s,k}$ is the diffusion coefficient in particles type *k*, $c_{s,k}$ is Li ion concentration in particles type *k*, and σ_h is the hydrostatic stress. The mass balance for Li ions in particles type *k* is given by:

$$\frac{\partial c_{s,k}}{\partial t} = -\nabla \cdot J_k \tag{3.24}$$

with two boundary conditions as following:

$$\begin{aligned} J_k\Big|_{(r=0)} &= 0 \\ J_k\Big|_{(r=R_{0,k})} &= \frac{i_k}{F} \end{aligned} \tag{3.25}$$

Substitute Eq.(3.23) into Eq.,(3.24)

$$\frac{\partial c_{s,k}}{\partial t} = -\nabla \cdot (-D_{s,k}(\nabla c_{s,k} - \frac{\Omega c_{s,k}}{RT}\nabla \sigma_{h,k})) \tag{3.26}$$

Substitute Eq.(3.14) into Eq.(3.26) and expand in the spherical coordinates yields the modified diffusion equations:

$$\frac{\partial c_{s,k}}{\partial t} = D_{s,k}[\frac{\partial^2 c_{s,k}}{\partial r^2} + \frac{2}{r}\frac{\partial c_{s,k}}{\partial r} + Z_3(\frac{\partial c_{s,k}}{\partial r})^2 + Z_3 c_k(\frac{\partial^2 c_{s,k}}{\partial r^2} + \frac{2}{r}\frac{\partial c_{s,k}}{\partial r}))] \tag{3.27}$$

with two boundary conditions as following

$$\begin{aligned} \frac{\partial c_{s,k}}{\partial r}\Big|_{(r=0)} &= 0 \\ -D_{s,k}(1+Z_3 c_{s,k})\frac{\partial c_{s,k}}{\partial r}\Big|_{(r=R_{0,k})} &= \frac{i_k}{F} \end{aligned} \tag{3.28}$$

where

$$Z_3 = \frac{2\Omega^2 E}{9RT(1-\nu)} \tag{3.29}$$

In this way, to estimate the stress profile in the P2D model, we only need to modify the diffusion equation in the solid phase as the Eq.(3.27) with the two boundary conditions in Eq.(3.28). When the P2D model is solved as usual without adding more variables [19, 20, 85], the stress profile can be obtained according to Eq.(3.13).

3.3 Results and Discussion

In order to focus on analyzing the effect of the adding NCA on the LMO material, we only consider and discuss the stress generation inside the LMO particles. First, we show the simulated results for the pure LMO/Carbon cell. And then, the investigations for the cells with mixed electrode (LMO and NCA) are presented later. The properties of the materials and parameters used in the following simulations are given in Tables 3.1 and 3.2.

Figure 3.2 shows the simulated results for a pure LMO/Carbon cell discharged at C/2 to 3.0 V. The 1 C-rate is given as 10.75A/m^2. Figure 3.2 (a) shows the distribution of the concentration of lithium ions on the surface of the particles in the cathode at selected times. As shown in Figure 3.2 (a), the surface concentration of particles near the separator (x=1) is higher than that of the other particles. This indicates that the Li ion insertion is not homogeneous along the positive electrode and more Li ions are inserted into the particles near the separator.

Figure 3.2 (b) shows the distribution of the maximum radial stress in the particles in the positive electrode at the same selected times as in Figure 3.2 (a). The maximum radial stress is the largest radial stress inside a particle at the given time. The stress profiles

presented in shows different trends compared to the surface SOC distribution presented in. The stress in the particles near the separator is not always the largest one. This is different from that of the $LiCoO_2$ cathode as reported by Renganathan et al.[79]

It should be noted that the maximum radial stress is located at the center of the particle. This can be verified as follows. Taking the derivative of the radial stress shown in Eq. (3.13) with respect to *r* yields:

$$\frac{d\sigma_r}{dr} = \frac{2\Omega E}{3(1-v)}\left(-\frac{\int_0^r \frac{dc}{dr} r^3 dr}{r^4}\right) \tag{3.30}$$

Since $\frac{dc}{dr}$>0 during Li insertion, then $\frac{d\sigma_r}{dr}$ is less than zero in the particle. It means that the maximum radial stress in a particle is located at the center and is given by

$$\sigma_{r,\max} = \frac{2\Omega E}{9(1-v)}\left[\frac{3}{R_0^3}\int_0^{R_0} cr^2 dr - c\big|_{r=0}\right] \tag{3.31}$$

The two terms within the bracket in Eq.(3.31) are the average concentration and the concentration at the center of the particle, respectively. During discharge (Li insertion into the positive electrode particles), the concentration at the center of the particle is the lowest, that is, the average concentration is greater than the central concentration. The maximum radial stress obtained from Eq. (3.31)in a particle is a positive value, which means that the radial stress is a tensile stress during Li insertion. Inversely, during charge, the radial stress is negative and minimum (maximum in the absolute value) at the center of the particle, that is, the radial stress within the particle is a compressive stress and the maximum compressive radial stress is at the center of particle. In the following

discussion, the maximum radial stress is the absolute value of the maximum (in magnitude) radial stress inside particle. It should be kept in mind that the radial stress is a tensile stress during Li insertion and is a comprehensive stress during Li extraction.

The maximum and minimum tangential stresses can be obtained as follows. Taking the derivative of the tangential stress shown in Eq. (3.13) with respect to *r* yields:

$$\frac{d\sigma_t}{dr} = \frac{\Omega E}{3(1-v)}\left(-\frac{3\frac{dc}{dr}r^4 + \int_0^r \frac{dc}{dr}r^4 dr}{4r^4}\right) \tag{3.32}$$

Since $\frac{dc}{dr}$ >0 during Li insertion, $\frac{d\sigma_t}{dr}$ is less than zero. Therefore, the maximum tangential stress in a particle is located at the center (r=0) and the minimum tangential stress is located at the particle surface (r=R_0). The maximum and the minimum tangential stresses are given as following:

$$\begin{aligned}\sigma_{t,\max} &= \frac{2\Omega E}{9(1-v)}\left[\frac{3}{R_0^3}\int_0^{R_0} cr^2 dr - c\Big|_{r=0}\right] \\ \sigma_{t,\min} &= \frac{\Omega E}{3(1-v)}\left[\frac{3}{R_0^3}\int_0^{R_0} cr^2 dr - c\Big|_{r=R_0}\right]\end{aligned} \tag{3.33}$$

Compare Eqs. (3.31) and (3.33), we can see that the maximum tangential stress is equal to the maximum radial stress and both are tensile stresses during discharging process, similar to the numerical results reported in the literature [73]. The minimum tangential stress is less than zero during discharge, because that the concentration of Li ions on the particle surface is greater than elsewhere within the particle. Since the minimum tangential stress is negative, it is the maximum compressive stress during discharge. If

the stress-driven diffusion is ignored in the diffusion equation, the analytic solution for the concentration distribution in a spherical particle can be obtained as follows:[86]

$$c_{s,k}(r,t) = c_{s,p,avg}(t) - \frac{i_k R_{0,k}}{FD_{s,k}} \\ [\frac{1}{2}(\frac{r}{R_{0,k}})^2 - \frac{3}{10} - 2\frac{R_{0,k}}{r}\sum_{n=1}^{\infty}\frac{\sin(\frac{\lambda_n r}{R_{0,k}})}{\lambda_n{}^2\sin(\lambda_n)}\exp(\frac{-D_{s,k}\lambda_n{}^2 t}{R_{0,k}^2})] \tag{3.34}$$

where the average concentration $c_{s,p,avg}(t) = \frac{3}{R_0^3}\int_0^{R_0} cr^2 dr$ and the eigenvalue λ_n can be obtained by solving the eigenequation: tan (λ_n)= λ_n . The difference between the average concentration and the central concentration can be obtained from Eq. (3.34) as follows:

$$c_{s,p,avg}(t) - c\big|_{r=0} = \frac{i_k R_{0,k}}{FD_{s,k}}(-\frac{3}{10} - 2\sum_{n=1}^{\infty}\frac{1}{\lambda_n\ \sin(\lambda_n)}\exp(\frac{-D_{s,k}\lambda_n{}^2 t}{R_{0,k}^2})) \tag{3.35}$$

The difference between the average concentration and the surface concentration is given by:

$$c_{s,p,avg}(t) - c\big|_{r=R_0} = \frac{i_k R_{0,k}}{FD_{s,k}}(\frac{2}{10} - 2\sum_{n=1}^{\infty}\frac{1}{\lambda_n{}^2}\exp(\frac{-D_{s,k}\lambda_n{}^2 t}{R_{0,k}^2})) \tag{3.36}$$

Substitution Eqs.(3.35) and (3.36) into Eq.(3.33), we have:

$$abs(\sigma_{t,\max}) - abs(\sigma_{t,\min}) = \\ -\frac{2\Omega E}{3(1-v)}\frac{i_k R_{0,k}}{FD_{s,k}}\sum_{n=1}^{\infty}(\frac{2}{\lambda_n\sin(\lambda_n)} + \frac{3}{\lambda_n{}^2})\exp(\frac{-D_{s,k}\lambda_n{}^2 t}{R_{0,k}^2}) < 0 \tag{3.37}$$

Eq.(3.37) shows that the maximum compressive tangential stress ($\sigma_{t,\min}$) is greater than the maximum tensile radial/tangential stress ($\sigma_{t,\max}/\sigma_{r,\max}$) during discharge. But, the

difference shown in Eq.(3.37) becomes negligible when the concentration gradient has been well developed ($t > \frac{R_{0,k}^2}{D_{s,k}}$). This is similar to the numerical results reported by Christensen et al.[73] Cheng et al. have also derived that the steady value of these two maximum stresses are the same if distribution of insertion current density and stress-driven diffusion are neglected.

The distributions of the insertion current density for LMO in the positive electrode ($i_{\mathrm{LMO},p}$) at the selected time were presented in Figure 3.2 (c). The figure shows that the distributions of maximum radial stress and the insertion current density for LMO have the same patterns. For example, at t=1000s, the both the radial stress and the insertion current density for LMO near the separator are maximum in the cathode. Moreover, it can be found that the maximum radial stress is almost proportional to the insertion current density at each point in the cathode. The same phenomena were found in the stress studies with a single particle model where the maximum stress inside a particle almost linearly increases with the insertion current density [73, 74].

Figure 3.3 shows the maximum radial stresses in LMO particles in a pure LMO electrode vs. time at the interface between the cathode and the separator (Sep) and the interface between the current collector and the cathode (CC) during a C/2 discharge. The results indicate that although the stress in the particle at the interface between the cathode and the separator is not always the largest during the C/2 discharge, the largest tensile insertion stress (around 1000s) occurs at this interface. Since the particle fracture is more related to the largest stress the particle has suffered, therefore, the fracture and loss integrity occur more likely in the particles near the separator.[80] The fluctuation of the stress profile on a given position shown in Figure 3.3 is similar to Figure 1 in the

reference [74] and Figure 6 in reference [80]. As discussed earlier, this stress distribution is due to the change of insertion current density on the particle surface over time.

Figure 3.4 shows the maximum radial stresses as functions of applied current obtained from two different models: a single particle model and a P2D model. The maximum radial stresses here are referred to maximum radial stress in the whole electrode during the discharge process at a given applied current. In the single particle model, the distribution of the transfer current is ignored due to the assumptions of the constant electrolyte concentration and the constant solution phase potential in the cell. . In the single particle model, we only solve the Eq.(3.27) with two boundry coditions in Eq.(3.28). The insertion current density i_k on the particle surface is given by:

$$i_k = \frac{I_{app} R_{0,LMO}}{3\varepsilon_{1,LMO} l_p} \tag{3.38}$$

The stress profile is calculated based on the Eq.(3.13). As shown in Figure 3.4, the simulated maximum radial stress obtained from a P2D model is higher than that obtained from a single particle model, especially at the high C-rates. This is because that the non-uniform distribution in the transfer current in the cathode is considered in a P2D model as discussed above. It is indicated that the concentration and potential gradient in the solution phase plays an important role in the mechanical behavior of a cell. Also, the electrode design parameters, such as: the porosity and the thickness, which affect the transport of Li ions in the solution need to be carefully chosen based on the application of the cell. The effects of these parameters on the cell's mechanical behavior have been investigated in our previous work.[79]

Figure 3.5 shows the simulated maximum radial stress for LMO particles at selected positions (CC: near the current collector; Sep: near the separator) in a mixed electrode (LMO:NCA = 0.67:0.33, volume fraction) which is discharged at C/2 to 3 V. Although the cell capacity increases by increasing the fraction of NCA in the electrode, the 1 C-rate current for all mixed electrodes in this study is given as the same value in the pure LMO cell, which is 10.75A/m^2. The stress profiles shown in for the LMO particles in a mixed electrode are similar to those shown in for a pure LMO electrode during a C/2 discharge expect for the end part of discharge (time is greater than 5500s). As shown in, at the end part of discharge, the stress in the LMO particles is reduced significantly. This is because that during the end part of discharge, most Li ions are inserted into the NCA particles due to the OCP difference between LMO and NCA. As shown in Figure 3.11, the open circuit potential of NCA in the discharged state is much lower than that of LMO.

Figure 3.6 shows the simulated maximum stresses in a pure LMO cathode and a mixed cathode (LMO:NCA = 0.67:0.33, volume fraction) as functions of time during a 1C discharge/charge cycle. The black line represents the stress profile obtained from a blended material cathode; the green line is maximum stress profile for the pure LMO cathode. As shown in Figure 3.6 (red ellipse), the stress of LMO particle in the discharged state is reduced due to mixed with the NCA particles compared that obtained from a cell with a pure LMO cathode.

Some experiment work has showed that the dissolution of Mn from spinel LMO is a serious process in a discharged state during cell cycling.[54, 87, 88] Mn dissolution into the electrolyte due to acid attack and a disproportionation reaction at the particle surface is most likely to happen with more Mn^{3+} inside particle when the cell is in the discharged

state. If there is a protective layer on the particle surface such as a coating layer or a SEI layer, the Mn dissolution can be reduced.[61] As determined by experiments, the inactive layer is always formed on the LMO particle surface due to the Mn dissolution and the electrolyte oxidation.[8, 89] However, unlike the bulk LMO partilces which have been treated at high temperature, the new formed layer may be weak and be easily destroyed due to the particle expansion and contraction as shown in Figure 3.7. Therefore, the decrease in the stress in the discharged state for LMO particles in the mixed cathode may suppress the fracture of the SEI layer, because the reduced stress indicates the change of particle displacement decrease. Therefore, the existence of the layer in the discharged state can effetively protect the LMO surface from the acid attack and reduce the Mn dissolution. Moreover, if the stress on the particle surface contributed to the Mn dissolution directly due to the increase of strain engergy, the Mn dissolution would be surpressed when the stress is reduced. As discussed above, the reduction of the stress in a discharged state can explain the experimental obverations that the perfromance of LMO based electrode are improved by adding NCA [30].

The maximum radial stress of the cell with mixed electctrode (LMO:NCA = 0.67:0.33, volume fraction) during a constant current dischage/charge cycles (CC-CC protocol) at 1 C is shown in Figure 3.8. The results indicate that the stresses in the latter cycles are simliar to that in the first cycle in this study. This is because the current is low, the effect of previous Li insetrion and extraction on the stress are vanished in a short timescale.[73] The maximum radial stress in a cell cycled with the CC discharge-CC charge protocol is presented in the Figure 3.9. This protocol consists of a contant current discharge at 1 C to 3.0 V, followed by a contant current charge at 1 C to a selected cutoff

charge voltge, and then a constant voltage charge until the current drops to the cutoff current. Similarly to the CC-CC protocol cycle, there is no stress accumulation during the cell cycling in this study. Also, the simulation shows that the stress generation during the CV charge with a cutoff voltage of 4.3 V is similar to that with a cutoff voltage of 4.2 V.

The simulatated maximum stress profiles for the mixed LMO and NCA electrodes with four different volume ratios are shown in Figure 3.10. The following volume ratios between LMO and NCA are selected in this study: LMO:NCA = 0.9:0.1, 0.67:0.33, 0.5:0.5, 0.33: 0.67. The cells are discharged at 3C to 3.0 V. As expected, the reduced stress region increases by increasing the volume fraction of NCA. But it is also observed from that the maximum stress during discharge (as indicated by the dash arrow) increase with adding more NCA into the mixed electrode. Therefore, the tradeoff between the decrease in the stress in the end part of discharge and the increase in the maximum stress has to be considered when determining the volume fraction of NCA in the mixed electrode.

3.4 Conclusions

A mathematical model is developed in this study to understand the stress generation inside the LMO particle during discharge/charge in a Li-ion battery with a pure LMO or a mixed electrode (LMO and NCA) cathode. Simulation results for the pure LMO/Carbon full cell show that the stress generation inside LMO particle is non-uniform within the positive electrode. The results also indicate that the fracture or loss of particle integrity potentially occurs in the particles near the separator. The stress profiles obtained from a single particle model and a porous electrode model show a significant difference for the

high C rate discharge. This indicates that the single particle model cannot be used because of the non-uniform distributions in the concentration and the potential in the electrolyte in the high current rate studies. Simulation results for a mixed electrode show that the stress generated in the LMO particles is significantly reduced at the end of discharge in a mixed LMO and NCA electrode due to the OCP difference between the LMO and NCA. This stress reduction might partially explain why experiment invesigations show that the performance of the LMO based electrodes can be improved by adding NCA. Simulations for mixed electrodes with different blend ratios show that the reduced stress region increases by increasing the NCA ratio.

Table 3.1 Properties for the Active Materials

Parameters	Values		
	LMO	NCA	Carbon
c_{max}(mol m^{-3})	24161.23 [c]	49459.2 [c]	26389[d]
D_s (m^2 s^{-1})	1.0e-13[a]	See Eq. A-7 [a]	3.9e-14[d]
k_{Li} ($mol^{-0.5}$ $m^{2.5}$ s^{-1})	5.0e-10 [a]	1e-10 [a]	2.334e-11[c]
R_0(m)	1.7e-6 [a]	2.5e-6 [a]	12.5e-6[d]
θ^0	0.19[c]	0.412[c]	0.65[c]
R_{conc} (Ω m^2)	0.05 [a]	0.04 [a]	0[c]
E (GPa)	10 [b]	-	-
v	0.3 [b]	-	-
Ω (mol m^{-3})	2.29e4 [b]	-	-

Table 3.2 Model Parameters

Parameters	Values		
	Positive	Separator	Negative
ε_1	0.4166 [a]	-	0.428[c]
ε_2	0.4 [a]	0.37 [a]	0.4[c]
L (m)	50e-6 [a]	50e-6 [a]	70e-6[c]
σ (S m^{-1})	10 [a]	-	100[d]
τ	2.89 [a]	3.15 [a]	2.5[c]
α_a	0.5[c]		
α_c	0.5[c]		
t^+	0.363[a]		
$c^0_{Li^+}$ (mol m^{-3})	1000[a]		
D (m^2 s^{-1})	See Eq. A-3 [a]		
κ (mol m^{-3})	See Eq. A-4 [a]		
F (C equiv^{-1})	96487		
R (J mol^{-1} K^{-1})	8.314		
T (K)	298.15		

[a] obtained from Ref [[82]]; [b] obtained from Ref. [[75]]; [c] assumed; [d] obtained from Ref. [40].

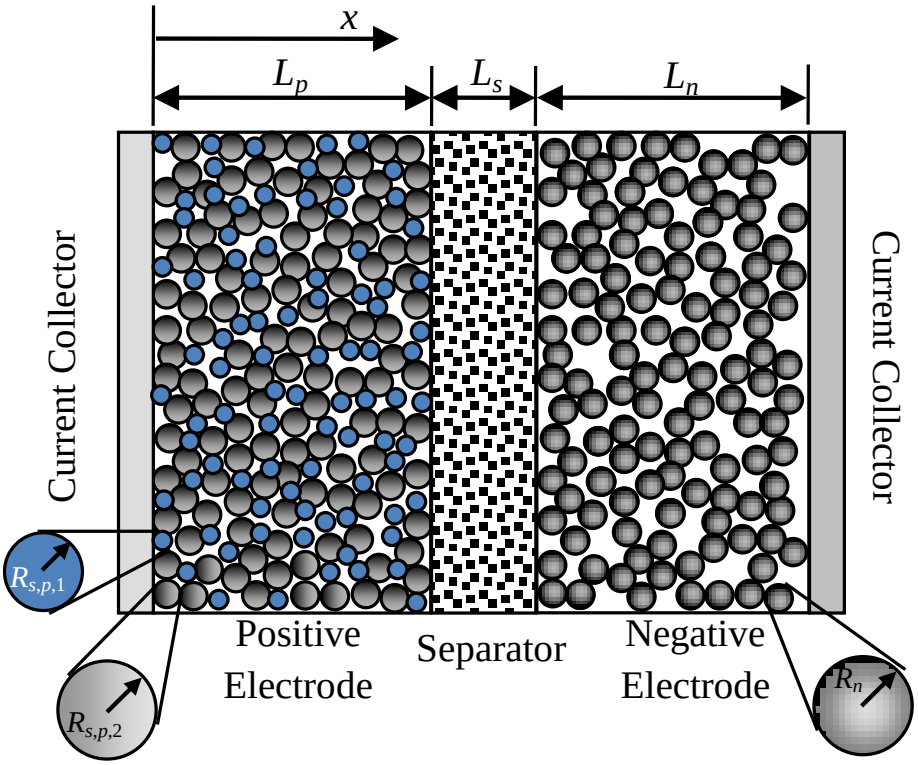

Figure 3.1 Schematic of a Li-ion battery.

(a)

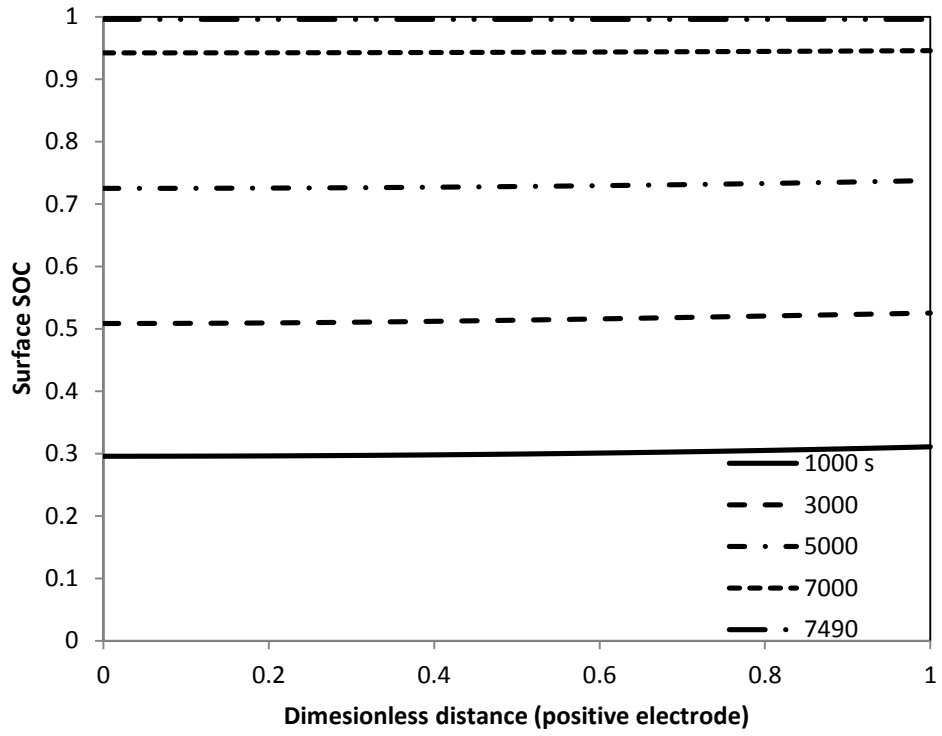
Surface SOC
1
0.9
0.8
0.7
0.6
0.5
0.4
0.3
0.2
0.1
0
0
0.2
0.4
0.6
0.8
1
Dimesionless distance (positive electrode)
1000 s
3000
5000
7000
7490

(b)

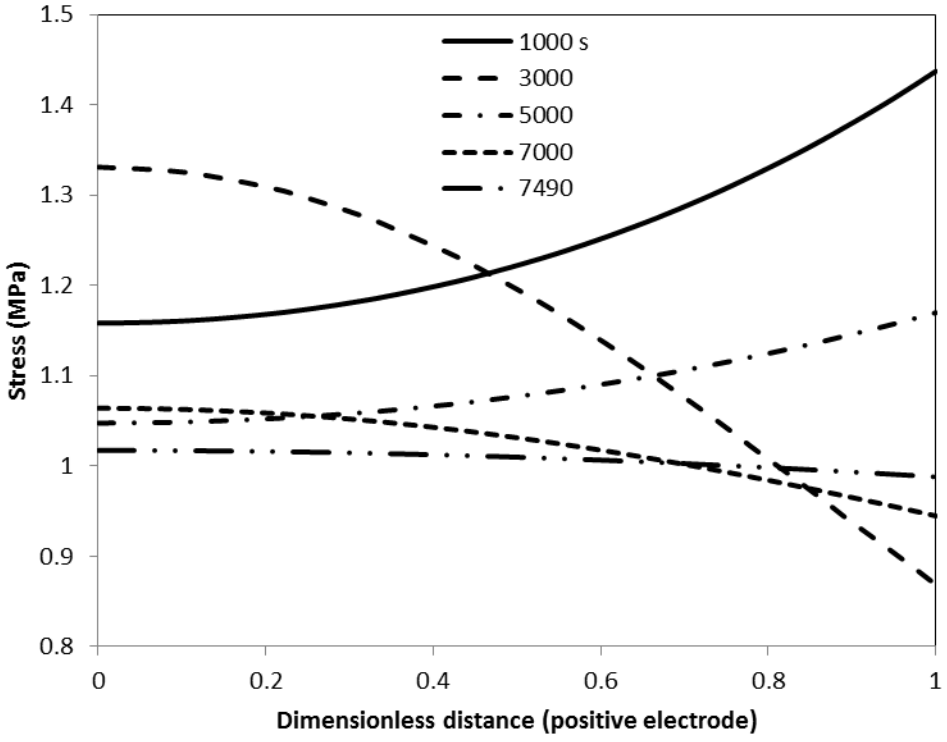
Stress (MPa)
1.5
1.4
1.3
1.2
1.1
1
0.9
0.8
0
0.2
0.4
0.6
0.8
1
Dimensionless distance (positive electrode)
1000 s
3000
5000
7000
7490

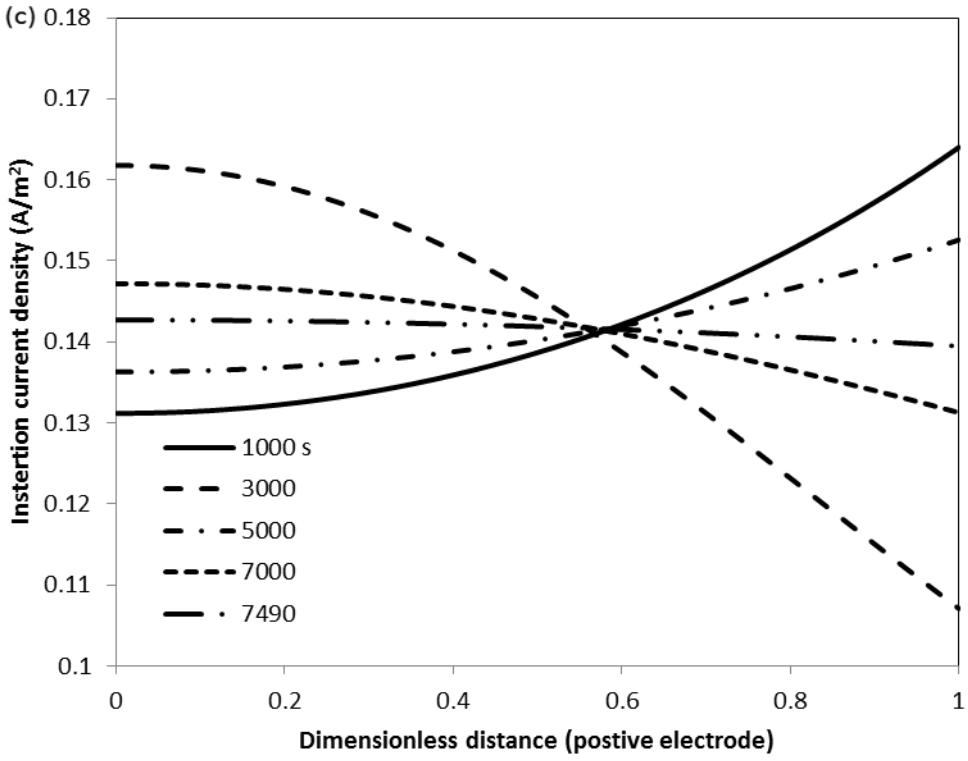

Figure 3.2 Simulated Li insertion into LMO particle in a pure LMO/carbon cell discharged to 3.0 V with C/2.(a) Surface state of charge; (b) Maximum radial stresses; (c) Insertion current in the LMO particle across thickness of cathode at selected time (t=1000, 3000,5000,7000,7490 s).

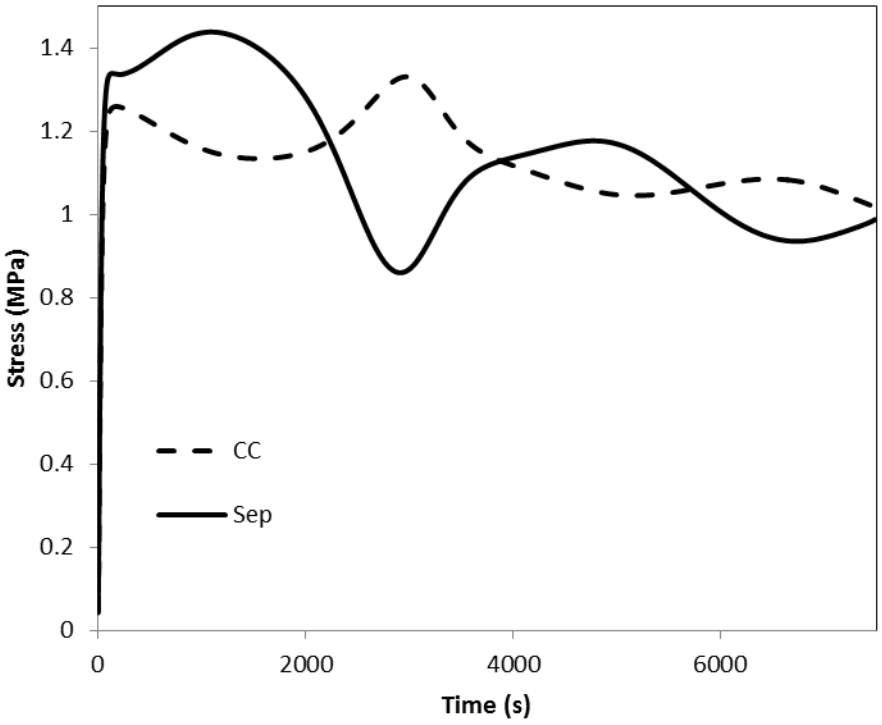

Figure 3.3 Maximum radial stress vs. time for LMO particles at different positions: current collector (dash line) and separator (solid line) in a pure LMO electrode discharged at C/2 to 3.0 V.

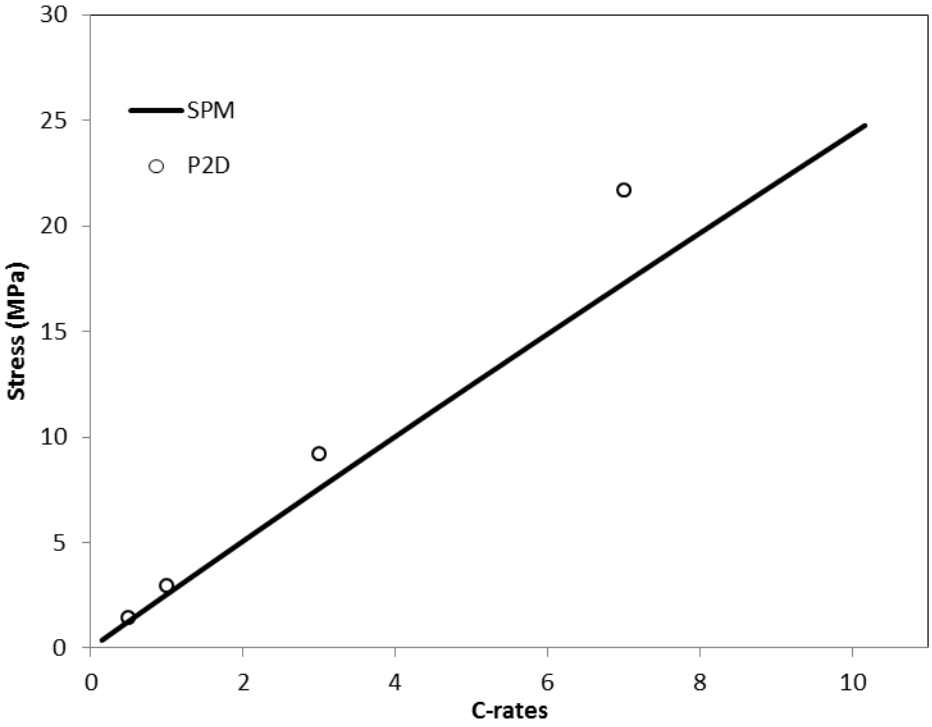

Figure 3.4 Maximum radial stress vs. C-rates calculated with two different models: porous electrode model (circle) and single particle model (solid line).

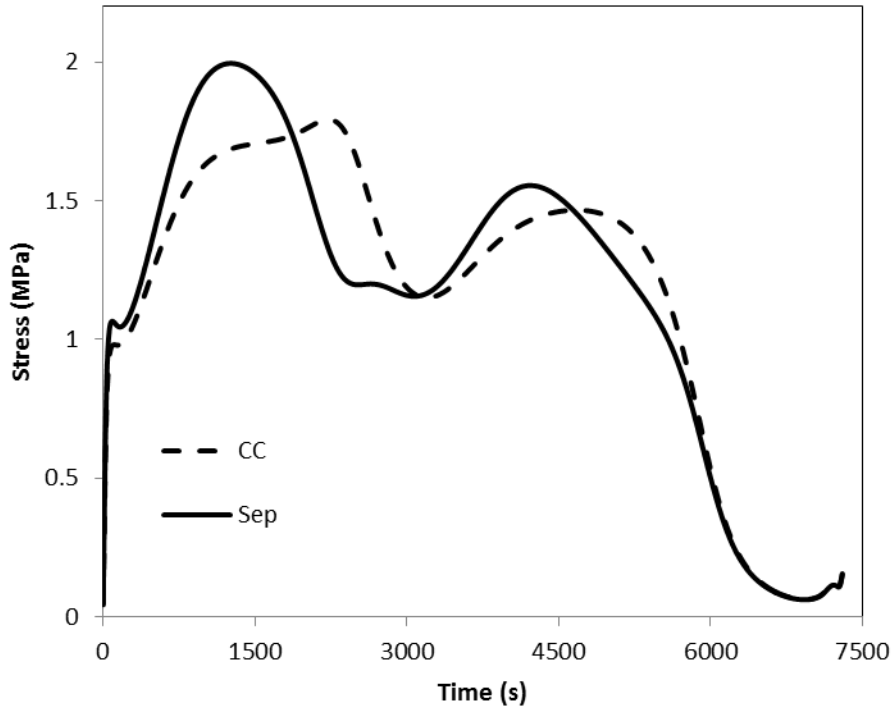

Figure 3.5 Stress profile of LMO particle at different position: current collector (dash line) and separator (solid line) in mixed electrode (LMO:NCA=0.67:0.33, volume fraction) with C/2 discharged to 3.0 V.

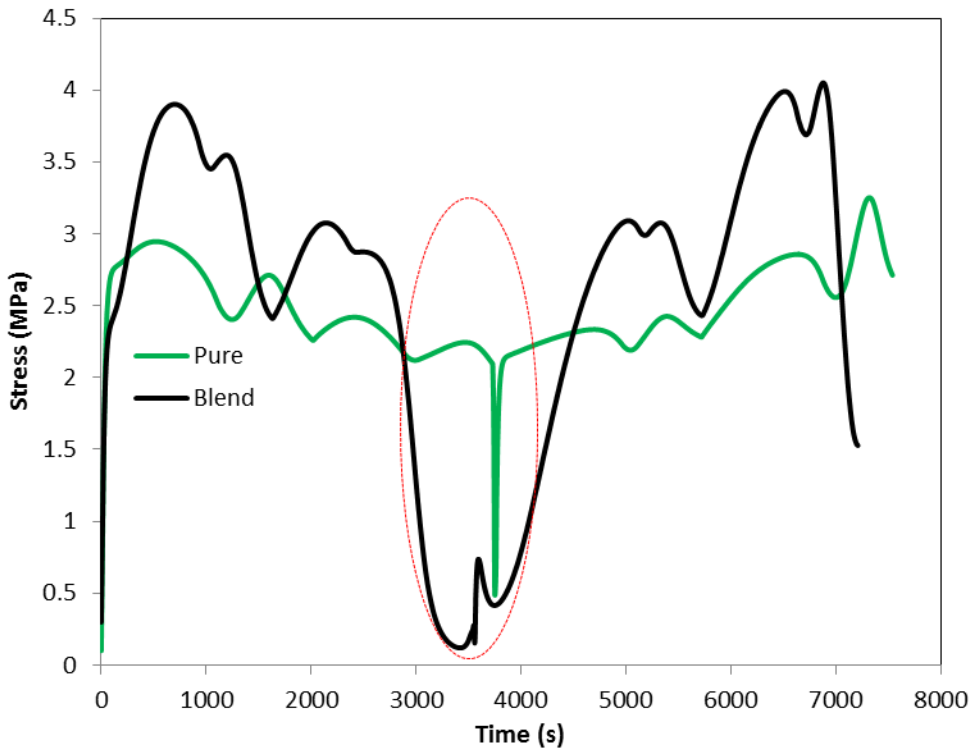

Figure 3.6 Maximum radial stress inside LMO particle vs. time with 1C discharge/charge cycling of mixed electrode (black, LMO:NCA=0.67:0.33, volume fraction) or pure electrode (green)/ carbon full cell between 3.0 V and 4.3 V. The ellipse indicated the stress reduction region in the mixed electrode compared to pure electrode during cycling.

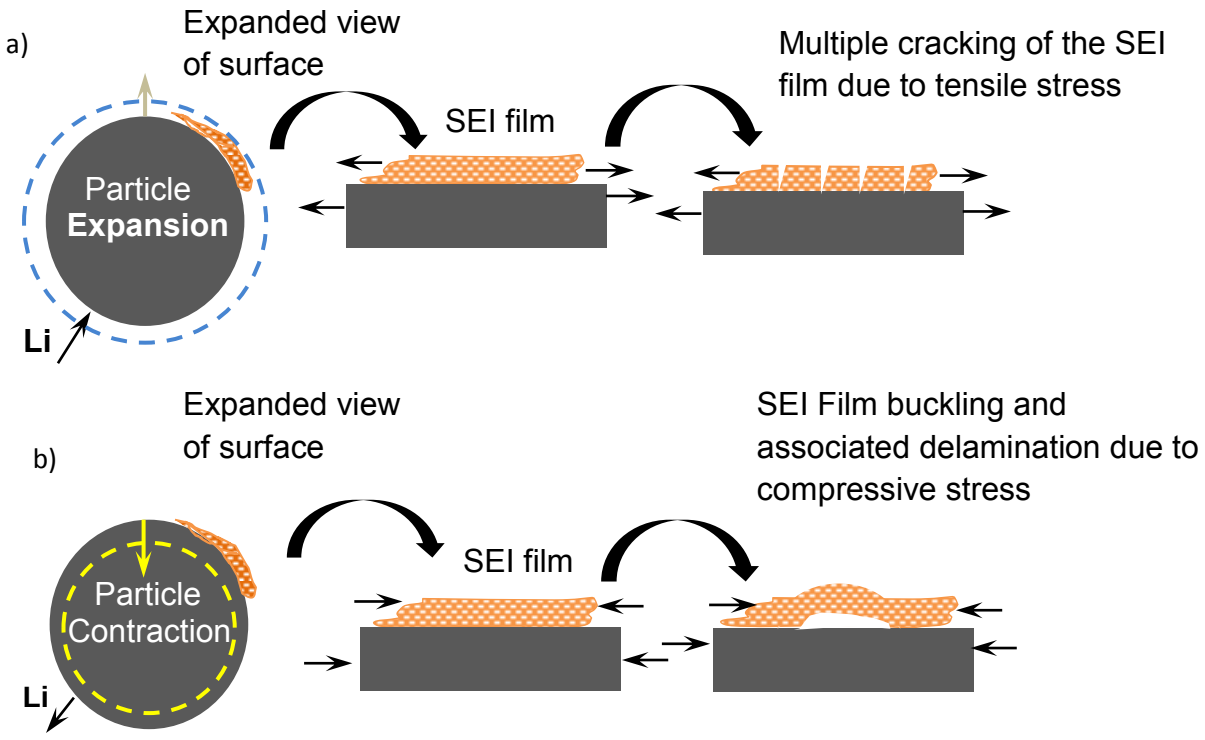

Figure 3.7 Schematic of failure that may occur in LMO particle surface due to Li insertion/extraction: (a) Li insertion (discharge); (b) Li insertion (charge).

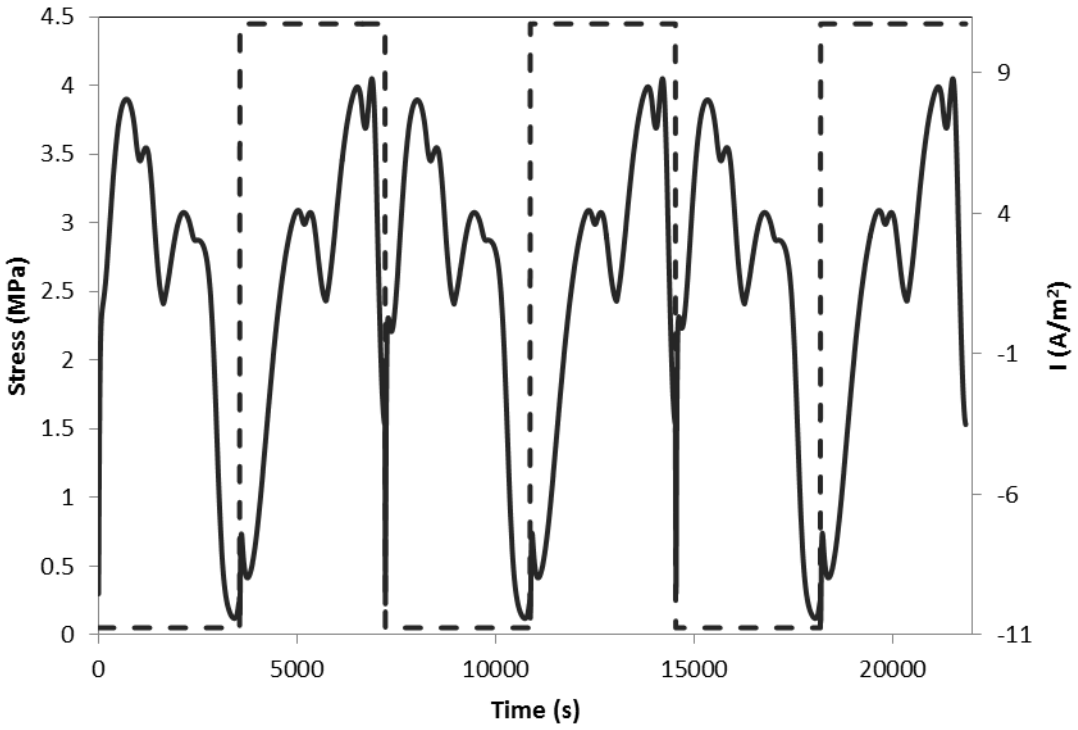

Figure 3.8 Simulated stress generation inside LMO particle with 1C discharge/charge cycling of mixed electrode (LMO:NCA=0.67:0.33, volume fraction) between 3.0 V and 4.3 V. The dash line is the applied current, corresponding to right axis. Positive current is charged process, and negative current is discharged process.

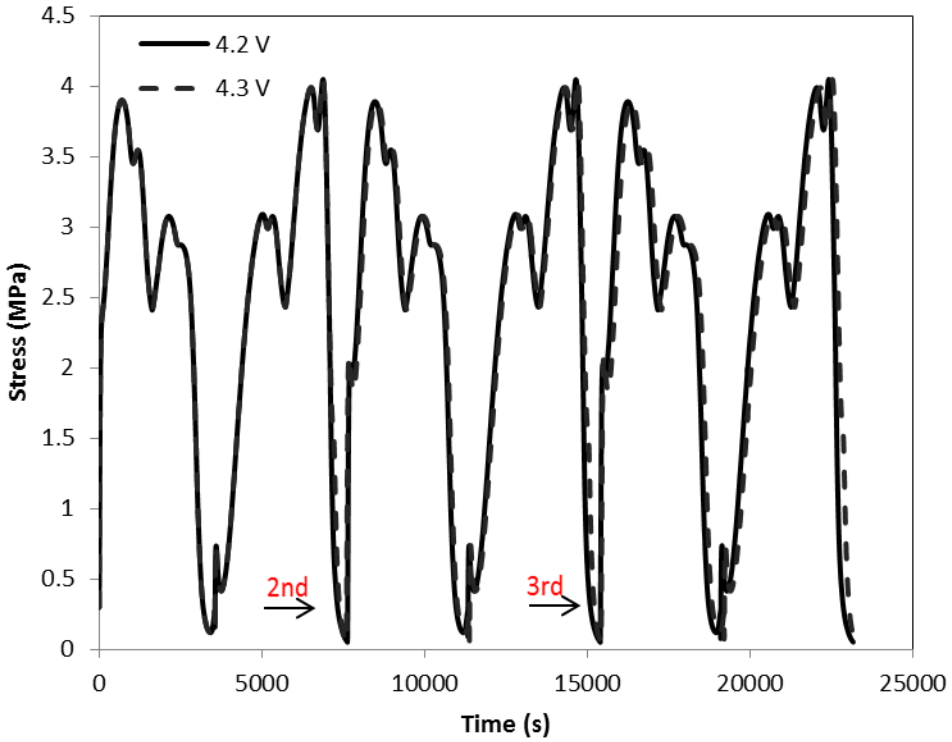

Figure 3.9 Simulated stress generation inside LMO particle in mixed electrode (LMO:NCA=0.67:0.33, volume fraction) with 1C discharge/ 1C charge to cut-off voltage and constant current charge to cut-off current. Two different cut-off charge voltages, 4.2 V (solid line) and 4.3 V (dash line) are applied. The arrow in the picture indicates a new cycle.

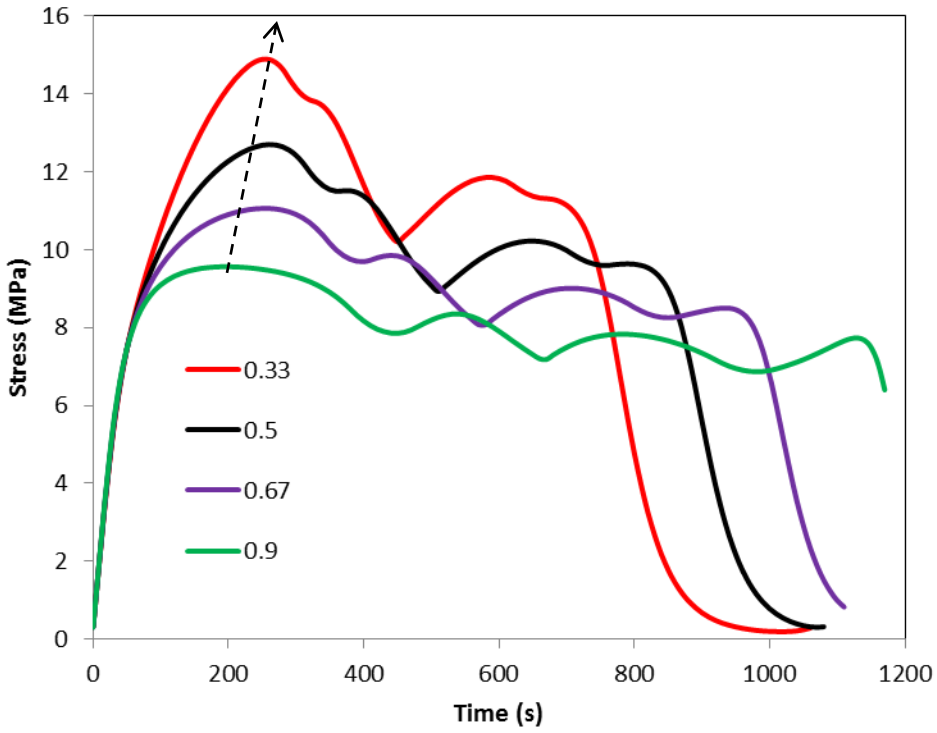

Figure 3.10 Simulation stress vs. time, of different blend ratio mixed electrode with 3C discharged to 3.0 V. 0.33-red, 0.5-black, 0.67-purple, 0.9-green of LMO volume fraction in mixed electrode. The dash arrow indicates the largest stress during the whole discharge process.

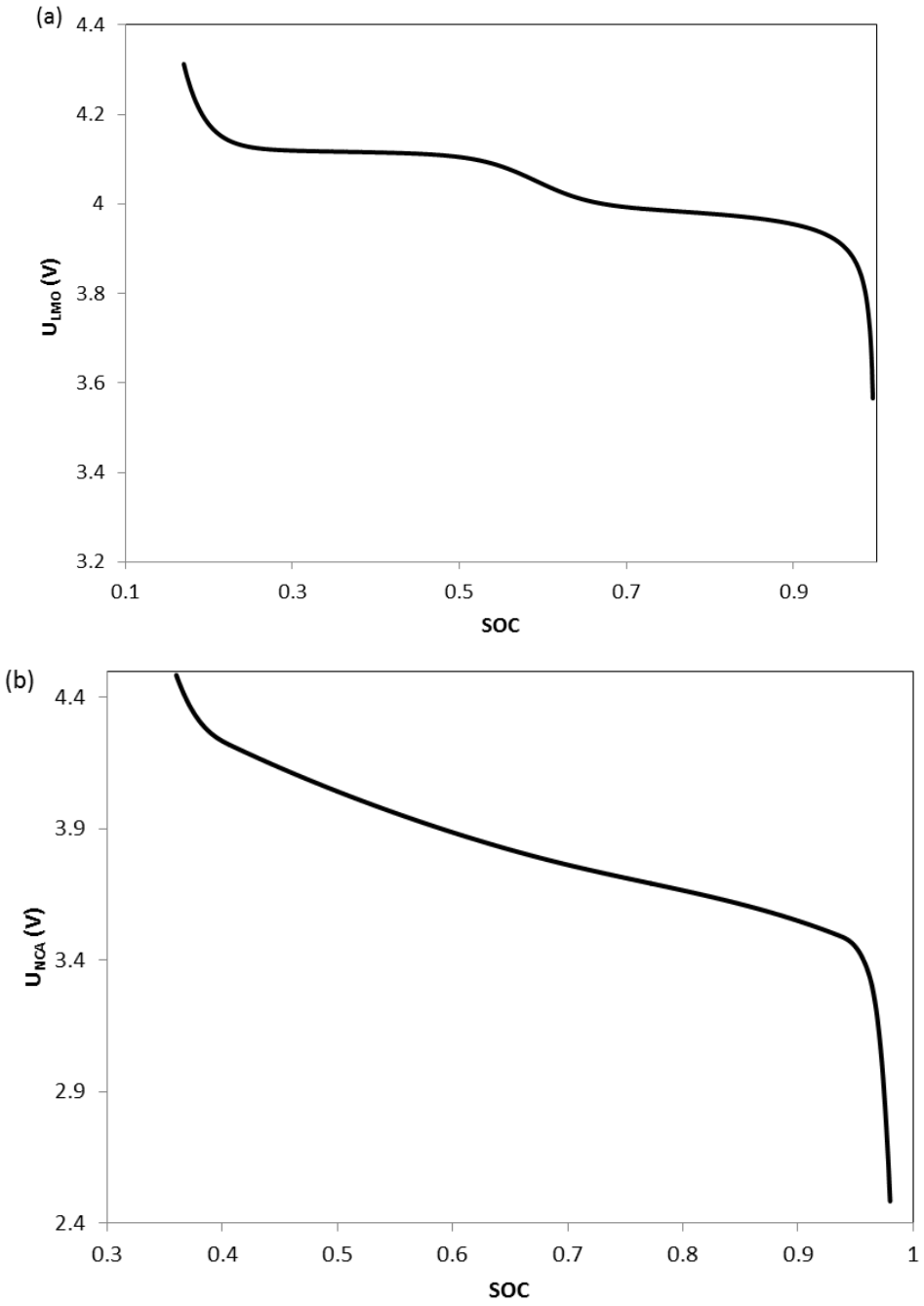

Figure 3.11 The open circuit potential profiles for (a) LMO; (b) NCA

4 Simulation and Analysis of Inhomogeneous Degradation in Large Format $LiMn_2O_4$/Carbon Cells

4.1 Introduction

Since the first commercial lithium-ion battery was released by Sony in 1991, Li-ion batteries have become the most desirable power sources for portable consumer electronics. Nowadays, to meet the challenge of the global warming and the finite nature of fossil fuels, Li-ion batteries are being intensively pursued for transportation application and stationary storage of renewable energies. However, current battery falls behind the life requirement due to the undesirable aging phenomena which do harm to the battery health condition during operation. For example, the life of Li-ion batteries used in hybrid electric/electric vehicles (EV/HEVs) is required over ten years.

The capacity degradation of Li-ion batteries is multifold. One of the most important reasons is the loss of the cyclable lithium due to the Li plating and the solid electrolyte film (SEI) layer formation on the carbonaceous anode [5, 6]. This SEI layer is mainly generated during the initial formation cycling of a fresh cell and prevents the further formation of the SEI film. But the damage of the SEI film due to the sink and expansion of the anode particle during cycling can still lead to new formation of SEI film on the newly opened site on the anode particle. The loss of active material is another important contribution to the capacity loss of Lithium ion batteries. It is found that most of the cathode active materials are not stable in the common organic electrolyte [9]. The

dissolution of transition metal from the cathode active material into the electrolyte has been intensively reported [9, 10]. In addition, particle fracture of the active material is observed due to electrochemical cycling [15-17]. The particle fracture not only leads to the loss of the active material, but also causes the increase of the resistance, and the loss of cyclable lithium. This is because that the particle fracture will generate more fresh active material surfaces on which the new SEI film is formed, in the meanwhile, the particle fracture can also lead to the loss connection of the active material particle to the conductor [18].

Furthermore, the cell degradation is found not homogeneous both in-thickness and in-plane direction of electrode. Kostecki et al. [24] reported that the gradual structural degradation of the graphite was most serious on the electrode surface. And, a thick layer of inorganic product was observed on the disordered carbon near the electrode/separator interface. In an 18650 cell, the postmortem SEM images show that the particle fracture is more pronounced in the region closest to the separator region [80]. Unlike the study of inhomogeneous degradation in cross-section of the electrode, Cai et al. [90] recently conducted the in-situ observation on the electrode degradation in-plane direction on a large-format LMO/graphite cell. It was found that the loss of LMO active material is more serious at the electrode edge. However, the cause of the inhomogeneous degradation in-plane direction is still unclear and less studied.

The diagnostics of the cell degradation is still a challenging work today due to the complexity of the Li-ion batteries, especially, for the large-format batteries due to its highly non-uniform distributions in the concentration and the potential in-plane direction [91]. Luckily, mathematical modeling method provides us an effective way to explore

what happens inside Li-ion batteries. The prediction of thermal, electrical, electrochemical, and mechanical response of the battery using simulation is essential for understanding the behavior of batteries.

A pseudo two dimensional (P2D) model has been applied to study the in-thickness degradation [22, 23]. In this model, the gradients of the variables are assumed to be negligible in the other two directions which parallel to the current collectors. This assumption may be valid for small-scale cells, but it is not reasonable for large-format cells. Multi-dimensional models are desirable to understand the behavior in a large format cell. Chen et al. [92] have developed a multi-dimensional model to examine the temperature distribution across the large cell. Their model took into account the current distribution caused by temperature difference, but the effect of the Ohmic loss in the current collector was ignored. Baker et al. [93] developed a physics-based model to predict the three-dimensional (3-D) current and temperature distributions in a large format cell. Most importantly, the Ohmic loss in the current collector was considered for a large format cell in their model. To reduce the computation time, Harb et al. [94] decoupled the 3-D computational domain into a 1-D component in the thickness direction of the electrodes and a 2-D component in the in-plane dimensions of the collectors for a spirally wound lead-acid cell. The classic P2D model was applied to the 1-D component; on the other hand, the potential distribution in the current collector was simulated in the 2-D component. A similar method was implemented later by other groups for planar cells [95, 96]. However, in these studies, the cell misalignment and the edge effects were ignored. Recently, Tang et al. [97] developed a simplified 2D model to investigate the Li-plating in a cylindrical cell. The main simplifications in their model are that the electrode

was assumed as the solid film electrode and the electrolyte concentration was assumed as a constant. They found that Li-plating would be serious on the anode edge, and the anode extension is a simple but effective way to mitigate the Li plating.

However, the simulation work that investigated the degradation of the LMO cathode in a large-format cell has been rarely reported. To explore the inhomogeneous degradation behavior of LMO electrode in a large format cell, we develop a two-dimensional mathematical model by including non-uniform porous electrode properties and the edge effect. Our analysis is based on the model predicting chemical, electrochemical and mechanical situation that the cell has encountered.

4.2 Model Development

Figure 4.1 shows a two-dimensional schematic diagram of a Li-ion battery. One is height direction (in-plane), Y, and the other is thickness direction (in-thickness), X. The battery consists of two current collectors, a LMO cathode, a separator, a carbon anode, and electrolyte filled in the porosity. Similarity to other studies [93, 98], the terminal tabs are ignored. Current is assumed to flow in and out uniformly from the top of current collector. The length of LMO electrode is 10 cm. The length of carbon electrode is varied in the study. The extension or shortage of anode is equal at both edges. The length of extra electrolyte on the sides of LMO electrode is 1 cm. Other parameters of the cell can be found in the Table 4.1. The P2D model is solved in the 2-D domain.

The P2D model has been applied to simulate the behavior of Li-ion batteries in several papers [19, 20, 85]. The mass balance and the charge balance are considered in both the solution phase and the solid phase. We only briefly introduce the model here as

follows. A detailed explanation of the porous electrode models can be found elsewhere [19, 20, 85].

The mass balance for Li^+ in the electrolyte is given as follows:

$$\frac{\partial\left(\varepsilon_{2,i}c_{e,i}\right)}{\partial t}=\nabla\bullet\left(D_{\mathrm{e,eff},i}\nabla c_{e,i}\right)+\left(1-t_{+}^{0}\right)a_{i}J_{i},i=p,s,n,e \tag{4.1}$$

where $\varepsilon_{2,i}$ is the porosity in cell component i ($i=p$ for the cathode, $i=s$ for the separator, and $i=n$ for the anode, $i=e$ for the extra electrolyte area), c_e is the concentration of Li^+, $D_{e,eff}$ is the effective diffusivity of Li^+ in the electrolyte, t_+^0 is the transport number of Li^+, F is Faraday's constant, and J_i is the pore wall flux of lithium ions on the surface of the active material, a_i is the specific surface area of active material particle and is defined as follows:

$$a_{i}=\frac{3\varepsilon_{1,i}}{R_{s,i}} \tag{4.2}$$

where $\varepsilon_{1,i}$ is the volume fraction of active material in region i, and $R_{s,i}$ is the radius of active material particle. The potential in the solid phase, ϕ_1, is given by Ohm's law as follows:

$$\nabla\bullet\left(\sigma_{\mathrm{eff},i}\nabla\phi_{1,i}\right)=a_{i}FJ_{i},i=p,n \tag{4.3}$$

where $\sigma_{eff,i}$ is the effective conductivity in the solid phase.

The solution phase potential, ϕ_2, is given by:

$$\nabla\bullet\left(-\kappa_{eff,i}\nabla\phi_{2,i}+\frac{2RT\left(1-t_{+}^{0}\right)\kappa_{eff,i}}{F}\nabla\left(\ln c_{e,i}\right)\right)=a_{i}FJ_{i},i=p,s,n,e \tag{4.4}$$

where $\kappa_{eff,i}$ is the effective conductivity in the solution phase, R is the gas constant, T is the temperature.

The pore wall flux of Lithium, J_i , is described by the Butler-Volmer equation as follows:

$$J_i = k_{Li,i} c_{s,surf,i}^{0.5} \left(c_{\max,i} - c_{s,surf,i}\right)^{0.5} c_e^{0.5} [\exp(\frac{\alpha_a F}{RT}\eta_i) - \exp(-\frac{\alpha_c F}{RT}\eta_i)] \tag{4.5}$$

where $k_{Li,i}$ is the reaction rate constant, $c_{s,surf,i}$ is the surface Li^+ concentration of particles, $c_{max,i}$ is the maximum concentration of Li^+ in the particles. The over-potential for particle in region i is given by:

$$\eta_i = \phi_1 - \phi_2 - U_i \tag{4.6}$$

where U_i is open-circuit potential for particle in region i. The effective properties are discussed and presented in the Appendix C.

The material balance in the particles can be written using Fick's second law as follows:

$$\frac{\partial c_{s,i}}{\partial t} = \frac{1}{r^2}\frac{\partial}{\partial r}[D_{s,i} r^2 (\frac{\partial c_{s,i}}{\partial r})] \tag{4.7}$$

The boundary conditions for the solid phase diffusion are given by:

$$-D_{s,i}\left.\frac{\partial c_{s,i}}{\partial r}\right|_{r=0} = 0 \tag{4.8}$$

$$-D_{s,i}\left.\frac{\partial c_{s,i}}{\partial r}\right|_{r=R_{s,i}} = J_i \tag{4.9}$$

To further reduce the computation cost, we applied the three-term polynomial approximation for the Li diffusion in solid phase [99]:

$$\frac{dc_{s,\mathrm{avg},i}}{dt} = -\frac{3J_i}{R_{s,i}}, i = p, n \tag{4.10}$$

$$\frac{dq_{s,\mathrm{avg},i}}{dt} = -\frac{30D_{s,i}q_{s,\mathrm{avg},i}}{R_{s,i}^2} - \frac{45J_i}{2R_{s,i}^2}, i = p, n \tag{4.11}$$

$$c_{s,surf,i} - c_{s,\mathrm{avg},i} = \frac{8R_{s,i}q_{s,\mathrm{avg},i}}{35} - \frac{R_{s,i}J_i}{35D_{s,i}}, i = p, n \tag{4.12}$$

where $c_{s,\mathrm{avg},i}$ is volume averaged concentration in the particle, $q_{s,\mathrm{avg},i}$ is volume averaged flux in the particle.

The solution phase current and lithium flux at the current collector/electrolyte interfaces and the outer surfaces of the extra electrolyte are zero:

$$\vec{n} \cdot \left(-D_{\mathrm{e,eff},i} \nabla c_e\right) = 0 \tag{4.13}$$

$$\vec{n} \cdot \left(-\kappa_{eff,i} \nabla \phi_{2,i} + \frac{2RT\left(1 - t_+^0\right)\kappa_{eff,i}}{F} \nabla \left(\ln c_{e,i}\right) \right) = 0 \tag{4.14}$$

where $\vec{n}$ is the normal direction of the boundary.

Because the current is carried by the solution phase at the electrode/separator interface and electrode/flood electrolyte interface, the currents in the solid phase at these interfaces are zero:

$$\vec{n} \cdot \left(-\sigma_{\mathrm{eff},i} \nabla \phi_{1,i}\right) = 0 \tag{4.15}$$

The current is applied at the top of positive current collector, that is:

$$-\sigma_{\mathrm{cc},i}\frac{\partial \phi_{1,top,pos}}{\partial Y} = I_{app} \tag{4.16}$$

where I_{app} is applied current.

The potential at the top of the negative current collector, $\phi_{1,top,neg}$, is set to zero,

$$\phi_{1,top,neg} = 0 \tag{4.17}$$

The cell voltage, V_{cell}, is determined by:

$$V_{cell} = \phi_{1,top,pos} - \phi_{1,top,neg} \tag{4.18}$$

4.3 Results and Discussions

We first conducted a simulation for a full cell with a shorter anode. Then, we ran the same simulation but applied 1 mm anode extension. Finally, we ran simulations to show the influence of adjustable design parameters and electrolyte properties on the cathode performance in a cell with the anode extension.

Shortage of anode electrode- One of the major problems of Li-ion batteries is Li plating on the anode. It does not only cause loss of cell capacity, but also cause a cell safety problem due to the growth of Li dendrite. Previous works have shown that Li plating occurs seriously at the anode edge, if the anode is not extended over the cathode [97, 100]. To elaborate this phenomenon, Figure 4.2a shows the potential difference between the solid phase and the electrolyte, $\phi_1 - \phi_2$, at the edge point (Point A1 shown in the figure 4.1)as well as at an inner point (Point A2 shown in the figure 4.1) of anode during the cell charging. In this simulation, the anode edge is 0.4 mm shorter than the

cathode edge. The distance between the edge and inner points is about 1 cm. The charge rate is 1C. The cell voltage is also plotted to indicate the cell charged state. Figure 4.2a shows that the potential difference at the edge point is lower than that at the inner point. Furthermore, the potential difference at the anode edge is less than zero before the cell voltage reaches the cut-off charge voltage (4.2 V).This indicates that the Li plating will occur first on the anode edge as expected.

Figure 4.2b shows the potential differences along the interface of separator/anode (Sep/Anode) and anode/current collector (Anode/CC) at the end of charge. It is indicated from Figure 4.2b that the potential difference distribution is not uniform in the in-plane direction, and there is a sharp drop near the anode edge. Also, it is almost symmetric, despite ohmic resistance on the current collector.

Extension of anode electrode - The practice of manufacturing cells with a longer anode than the cathode is widely accepted as means of preventing Li plating on the anode edge. Experiment has shown that the anode over the cathode by 1 mm can effectively prevent the Li plating [97, 100]. We investigate the effect of anode extension on preventing Li plating in a cell with the anode extension of 1 mm over the cathode in the following study.

Similarly to Figure 4.2a, Figure 4.3a shows the potential difference ($\phi_1 - \phi_2$) at the edge point as well as at the inner point of anode as function of time during 1C charge. In contrast to the anode shortage case, this figure shows that the potential difference at the edge is never less than zero during a 1C charge. Figure 4.3a also shows that the potential difference curve at the edge point is higher than that at the inner point, which was also observed in the experiment work [91]. This indicates that the anode extension can

mitigates the Li plating at the edge of the anode. However, the potential difference at inner points in the two cases shows no big change. This indicates that the edge effect is only limited in the edge area.

Figure 4.3b shows the potential difference along the Separator/Anode interface at the end of charge (left axis). Similar to the anode shorter case, the potential difference has a non-uniform distribution in plane direction. However, the potential difference shows an inverse distribution type. This indicated the edge effect is very sensitive to the electrode mismatch. The study with various anode extensions will be presented later.

Figure 4.3b also shows the state of charge (SOC) distribution along the Separator/Anode interface at the end of 1C charge (right axis). The SOC in this study is referred to $c_{s,\mathrm{avg}}$. As shown in Figure 4.3b, there is a big SOC jump near the edge of the anode. The SOC in the inner part of the anode is about 0.77, whereas the SOC at the edge of the anode is about 0.23 which is just a little higher than that before the cell was charged. It indicates that the edge of the anode is less utilized for lithium insertion in the case with anode extension.

Cathode performance- As shown above, the Li plating at the anode edge problem can be solved by extending the anode over the cathode edge. It is also important to investigate the performance of LMO cathode in the cell with the anode extension. Figure 4. 4 shows the potential difference at the edge point (Point C1 shown in the figure 1) and the inner point (Point C2 shown in the figure 1) of the cathode during a 1C charge. The distance between the edge and inner points is about 1 cm. The cell voltage is also plotted in Figure 4.4. As shown in Figure 4.4, the potential difference at the edge is higher than that at the inner point. Moreover, the potential difference at the edge is over 4.3 V at the end

of a 1C charge, which may lead to electrolyte oxidation at the cathode edge. It was found that the electrolyte oxidation will induce the LMO degradation [10], therefore, LMO may deteriorate more seriously at the cathode edge.

Figure 4.5 shows the SOC during cycling at two different positions: at the edge point and at the inner point of the cathode. The cell was cycled at 1C charge/discharge between 3.0 V and 4.2 V. It can be seen from Figure 4.5 that the LMO particles at the edge suffer a wider SOC range. These particles are both charged to lower SOC (over-charge) and discharged to higher SOC (over-discharge). As discussed earlier, the potential difference is higher at the electrode edge during charge, so it would lead the particles at edge to be overcharged. The over-discharge may be because that the particles at the edge are exposed to more carbon. It was found that the over-discharge in a cell with a LMO cathode will lead to the J-T distortion in the LMO cathode [87]. The higher SOC at the end of discharge shown in Figure 4.5 will increase the possibility of the J-T distortion at the cathode edge. From this point of view, the LMO degradation may be more pronounced at the edge.

The mechanical degradation such as the particle fracture in the active material is another contribution to the cell capacity loss. The lithium insertion/deinsertion will induce stress inside the active material particles. If the stress surpasses the yield stress of the material, the particle will crack. The insertion-induced stress can be qualitatively calculated based on the classic mechanical equations [73, 74]. Similar to Zhang et al. [75], the insertion-induced stress is estimated by the following equations:

$$\sigma_r = \frac{2\Omega E}{3(1-v)}[\frac{1}{R_0^3}\int_0^{R_s} cr^2 dr - \frac{1}{r^3}\int_0^r cr^2 dr]$$
$$\sigma_t = \frac{\Omega E}{3(1-v)}[\frac{2}{R_0^3}\int_0^{R_s} cr^2 dr - \frac{1}{r^3}\int_0^r cr^2 dr - c] \quad (4.19)$$

where σ_r and σ_t are the radial and tangential components of the stress tensor, Ω is the partial molar volume of LMO, E is Young's modulus, v is Poisson's ratio. As shown in our previous work [101], the maximum radial stress and the maximum tangential stress are located at the particle center ($r=0$) and the particle surface ($r=R_s$), respectively. We also found that if we neglect the stress-driven diffusion, the maximum radials tress and the maximum tangential stress are very close. In the following discussion, we only show the maximum tangential stress (the surface tangential stress, $\sigma_{t,surf} = \sigma_t\left(r = R_0\right)$). The maximum tangential stress on the particle surface from Eq.(4.19) can be written as:

$$\sigma_{t,surf} = \frac{\Omega E}{3(1-v)}(c_{s,\text{avg}} - c_{s,\text{surf}}) \quad (4.20)$$

So, we can estimate the tangential stress on the particle surface from our current model without modification. Although the stress-driven diffusion is not included in our model, it is still a good reflection of insertion-induced stress. It has been shown that the concentration profile within particle will not change very much without stress-driven diffusion [73, 75].

The estimated insertion-induce stress (the absolute value) as function of time is presented in Figure 6 during the cell cycling shown in Figure 4.5. During charge (e.g. 0-3600s) the particles at the edge are found to suffer a much higher maximal stress than those particles at the inner. In contrast, during discharge (e.g. 3600-7200s) the insertion-

induced stresses are very close for the particles at the electrode edge and the inner place. Since the particle fracture is related to the maximal stress the particle has suffered, Figure 6 shows that the particle fracture potentially occurs at the electrode edge. It can be found that the insertion-induced stress is related to the SOC as shown in Figure 4.5. During charge, the SOC vs. time curve in Figure 4.5 has a high slope (in magnitude) at the edge point than that at the inner point and the particle shows larger stress at the electrode edge in Figure 4.6. On the other hand, during discharge the SOC change at the edge is almost identical to that at the inner part and the stresses are close at both places. The SOC change rate at a given point is determined by the pore wall flux on the particle surface. Our previous study showed that in the porous electrode the insertion-induced stress is proportional to the pore wall flux on the particle surface which is similar to the case that in a single particle model the insertion-induced stress is proportional to the applied current [101].

Figures 4.4-6 together suggest that the degradation of LMO electrode would be more pronounced at the edge due to the following effects: the larger potential difference, the wider SOC range, and the higher insertion-induced stress. The model simulated inhomogeneous degradation mentioned above is in agreement with the experimental observation by Cai at al. [90]. They reported that LMO degradation was dominated at the electrode edge. They also suggested that electrolyte solution loss (dry-out) and non-uniform temperature distribution may be the reason that causes the capacity losses. But we believe that our simulation results can explain better why the degradation of LMO electrode in large-format cell is inhomogeneous.

In the following discussions, we investigated the effects of the adjustable design parameters and the electrolyte properties on the degradation at the cathode edge. The case studies below include varying the following parameters: the anode extension, the capacity ratio, the porosity, the electrode thickness, the diffusion coefficient in the electrolyte, and the conductivity of the electrolyte. For simplification, only the predicting potential differences at the edge of cathode are presented in the following part, as the cycling SOC range and the insertion-induced stress are related to the potential difference.

Effects of adjustable design parameters- Figure 4.7 shows the potential difference at edge of the cathode during 1C charge with various extensions of the anode. All the other parameters are held as the same as in the base case (1 mm), except for the tiny change in the capacity ratio due to the change in the anode length. It can be observed from Figure 4.7 that as the anode extension increases, the potential difference increases at the edge of the cathode. Therefore, the higher anode extension may increase the electrolyte oxidation at the cathode edge. This indicates that although the high anode extension helps reduce the Li plating at the anode edge, it may cause serious LMO degradation at the cathode edge. If a cell is cathode limited as those for high-power application, the cell capacity loss will be faster due to loss of LMO cathode. Figure 4.7 also shows that the anode extension does not affect the charging time. This is because that the cell considered here is cathode limited. Also, the utilization of the extension part of anode is very low as discussed earlier. These results highlight the importance of choosing optimum design of the anode extension length, which not only can prevent the Li-plating at the edge of the anode, but also has less possibility to increase the degradation of the cathode at the edge.

Moreover, these results indicate the edge effect due to electrode mismatch and the loss of LMO at the edge would enhance the other, which cause serious damage penetrating into the electrode. Cai et al. [90] reported that the serious degradation of LMO was observed at 10 mm from edge after 400 cycles. As discussed earlier, the electrode mismatch leads to the loss of active LMO at the edge which in turn increase the mismatch of the electrodes. Consequently, the increase of mismatch of the electrodes will continue result in the degradation of active LMO at the edge, as shown in Figure 4.7. Although the edge effect is limited in the small area close to edge as shown in Figure 4.2b and 4.3b, the combination of the loss of active LMO and the increase of the extent of electrodes mismatch will cause the degradation of the LMO moves to the inner part of the cathode.

Next, figure 4.8 shows the effect of capacity ratio on the cathode performance. The capacity ratio is defined as the ratio of the loading of the anode to the loading of the cathode. The capacity ratio was adjusted by changing the thickness of the anode, and other design parameters were kept the same as those in the base case (capacity ratio =1.3). As indicated in Figure 4.8, the capacity ratio has not significant influence on the potential difference at the edge of the cathode.

The effect of the electrode porosity on the potential difference at the edge of the cathode is illustrated in Figure 4.9. Various porosity values of the cathode and the anode were investigated. The porosity was adjusted by changing the electrode thickness and keeping the capacity ratio as constant. The other parameters were kept the same as those in the base case ($\varepsilon_{2,p}$ =0.416, $\varepsilon_{2,n}$=0.63). As shown in Figure 4.9, the potential difference does not change significantly as the porosity change in the electrode.

Figure 4.10 shows the effect of the thickness of the cathode on the potential difference at the edge of cathode. The thickness of the anode was changed accordingly with the change in the thickness of the cathode to keep the capacity ratio as constant. All the other parameters are the same as those in the base case (145 um). The charge rate is 1C. Here the applied current of 1C rate changes accordingly with the change in the thickness of the cathode. This study indicates that the potential difference at the edge of the cathode is less dependent on the electrode thickness.

Influence of electrolyte properties- We also investigated the effect of electrolyte properties on the potential difference at the cathode edge, although the improvement of these intrinsic electrolyte properties is difficult. Figure 4.11 shows the effect of Li ion diffusion coefficient in the electrolyte (a) and the electrolyte conductivity (b) on the potential difference at the edge of cathode. It can be observed from Figure 4.11 that as these two properties increases, the potential difference at the cathode edge decreases. When the diffusion coefficient and the conductivity in the electrolyte increase, the polarization loss decreases. Therefore, the potential difference decreases. However, the improvement is limiting, especially for the increase of diffusion coefficient. Together with the case studies presented above, it can be concluded that the cathode edge effect is dominated by the extent of mismatch between the cathode and the anode. It should be noted that the design like increase the capacity ratio and the diffusivity and ionic conductivity of the electrolyte will reduce the Li plating on the anode [97, 100].

4.4 Conclusions

A two-dimensional model considering the porous electrode property and electrode mismatch was developed to understand the inhomogeneous degradation of LMO

electrode in the large formation cells. First, this model is used to investigate the effect of the anode extension on the Li plating at the edge of anode. The anode extension can significantly reduce the possibility of Li-plating on the anode. However, the utilization of the extension part of the anode for Li insertion is very low. And the anode extension has no effect on the behavior of the bulk electrodes. Then, the model is used to predict the potential difference, state of charge, and the maximum tangential stress at the edge and the inner part of the cathode. From our simulation, it was found that the design of anode extension over cathode will increase the potential difference, cycling SOC range and insertion-induced stress for particles near the edge of cathode, although it help prevent the Li plating at the edge of anode in the anode shortage case. Therefore, the loss of LMO is more pronounced near the electrode edge as the experimental observations. Simulations also were conducted with different design adjustable parameters (anode extension length, capacity ratio, porosity and electrode thickness) and electrolyte properties (diffusion coefficient and conductivity). Among them, the cathode performance is most sensitive to the extent of cell mismatch. The larger anode extension would increase the potential of LMO degradation at the edge of cathode. Therefore, we point out that the longer extension is not always better for improvement of cell life and optimum design of anode extension length should be chosen.

Table 4.1 Properties for the Active Materials

Parameters	Values	
	LMO	Carbon
c_{max} (mol m^{-3})	22860 [a]	30540 [a]
D_s (m^2 s^{-1})	1.0×10^{-13} [a]	2.0×10^{-13} [a]
k_{Li} ($mol^{-0.5}$ $m^{2.5}$ s^{-1})	5.0×10^{-10} [c]	1.764×10^{-11} [b]
R_s (m)	8.5×10^{-6} [a]	12.5×10^{-6} [a]
θ^0	0.98 [d]	0.01 [d]
U (V)	See Eq. A-6	See Eq. A-7
E (GPa)	10 [e]	-
v	0.3 [e]	-
Ω (mol m^{-3})	2.29×10^{4} [e]	-

Table 4.2 Model Parameters

Parameters	Values		
	Positive	Separator	Negative
ε_1	0. 37 [a]	-	0.511[a]
ε_2	0.416 [a]	0.45 [b]	0.36 [a]
L (m)	145×10^{-6} [a]	25×10^{-6} [b]	85×10^{-6} [a]
L_{cc} (m)	15×10^{-6} [f]	-	10×10^{-6} [f]
σ (S m^{-1})	3.8 [a]	-	100 [a]
σ_{cc} (S m^{-1})	3.78×10^{7} [f]	-	5.96×10^{7} [f]
Brugg	1.5 [a]	1.5 [a]	1.5 [a]
α_a	0.5 [d]		
α_c	0.5 [d]		
t_+^0	0.363 [a]		
$c_{Li^+}^0$ (mol m^{-3})	1000 [a]		
D (m^2 s^{-1})	See Eq. A-3		
κ (mol m^{-3})	See Eq. A-4		
F (C equiv^{-1})	96487		
R (J mol^{-1} K^{-1})	8.314		
T (K)	298.15		

[a] obtained from Ref.[102]; [b] obtained from Ref.[103]; [c] obtained from Ref.[82] ;

[d]assumed; [e] obtained from Ref.[75]; [f] obtained from Ref.[95].

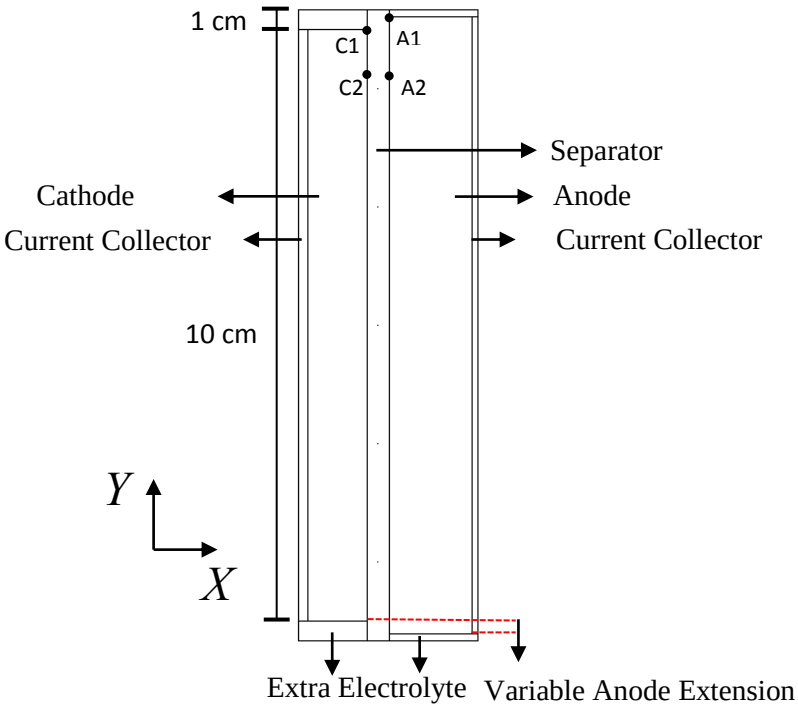

Figure 4.1 Schematic of a Li-ion battery in two-dimensional domain (not to scale)

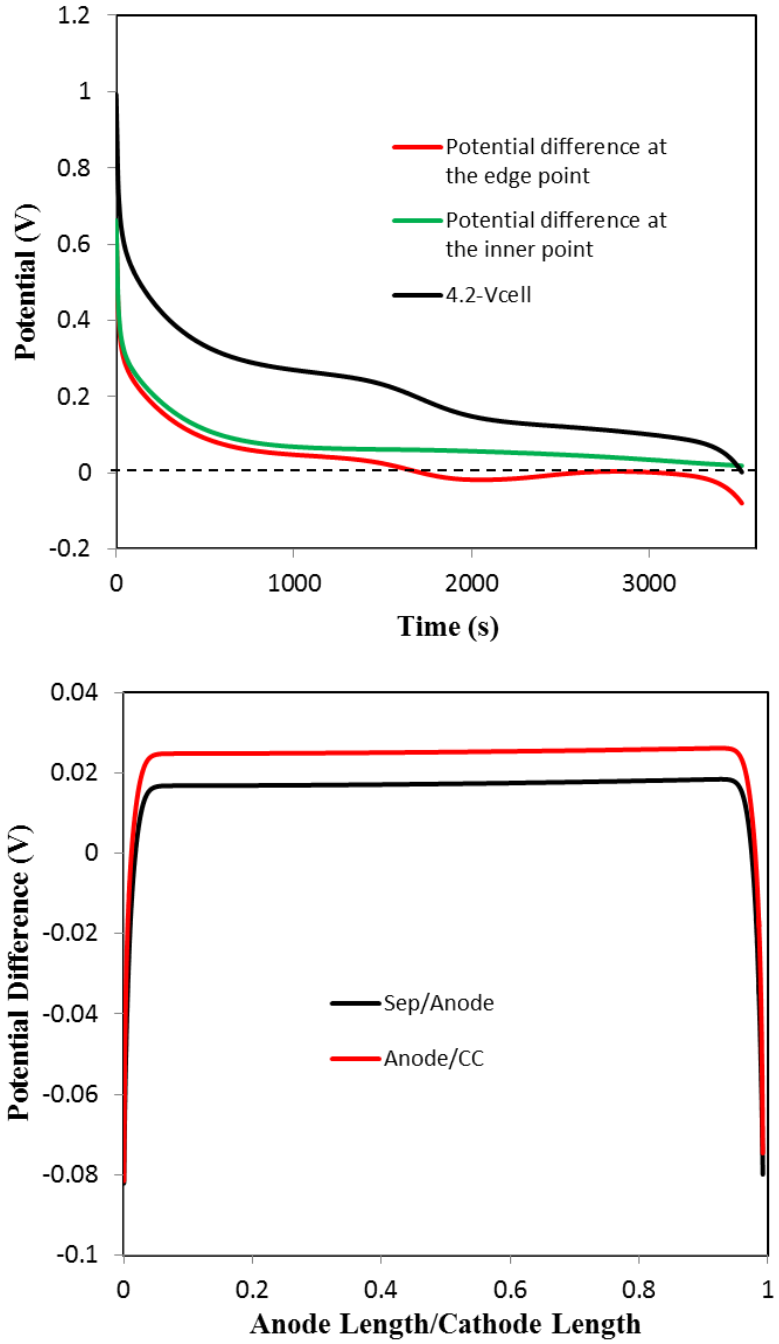

Figure 4.2 (a) The potential difference, $\phi_1 - \phi_2$, at the edge point as well as at the inner point of anode and the cell voltage as function of time; (b) The potential difference at the interfaces between separator and anode (Sep/Anode) and between anode and current collector (Anode/CC) at the end of first charge for a cell with anode 0.4 mm shorter than cathode.

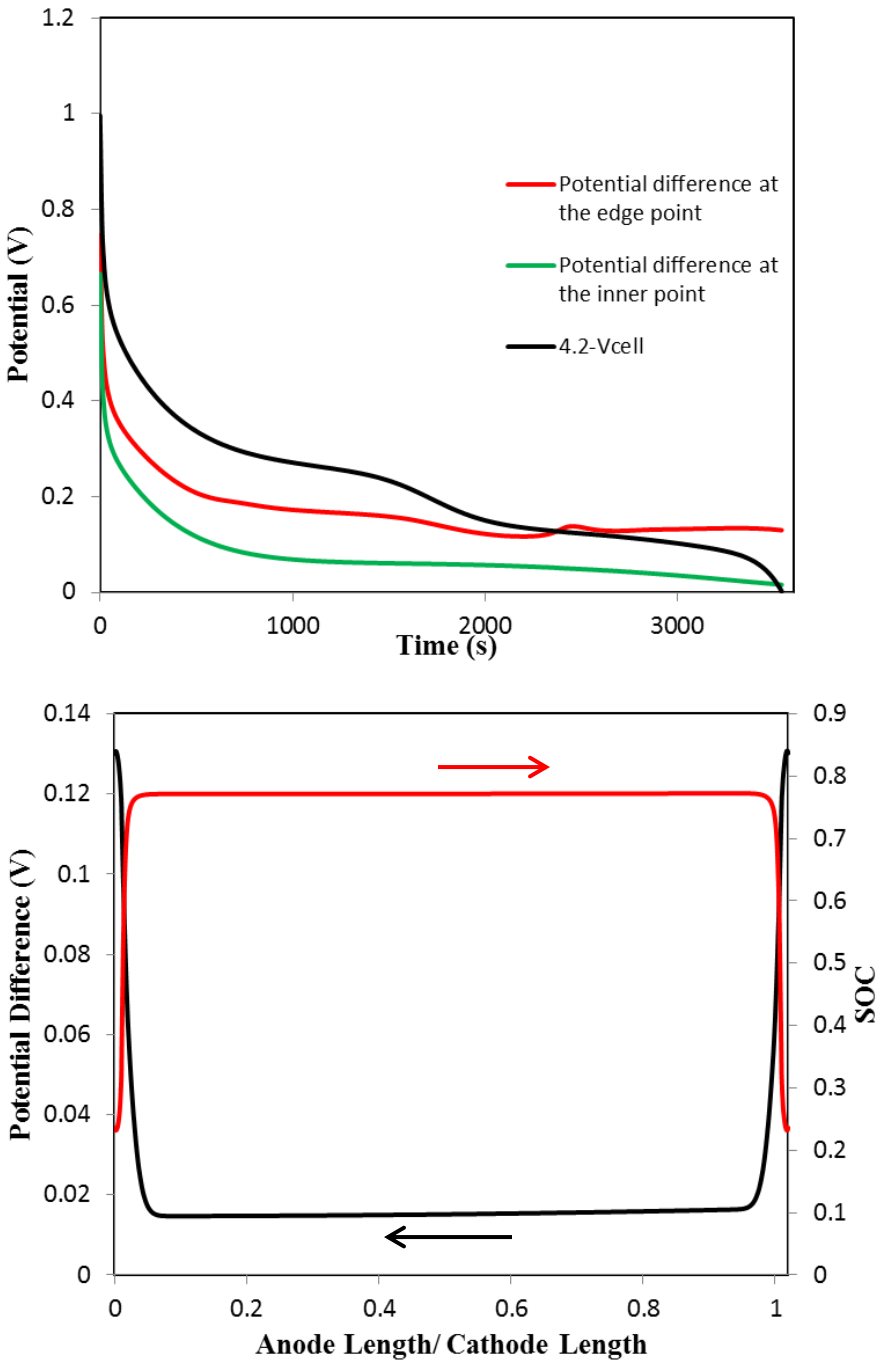

Figure 4.3 (a) The potential difference, $\phi_1 - \phi_2$, at the edge point as well as at the inner point of anode and the cell voltage as function of time; (b) The potential difference (right) and SOC (left) distribution along the anode/separator interface at the end of first charge for a cell with anode 1 mm extension over cathode.

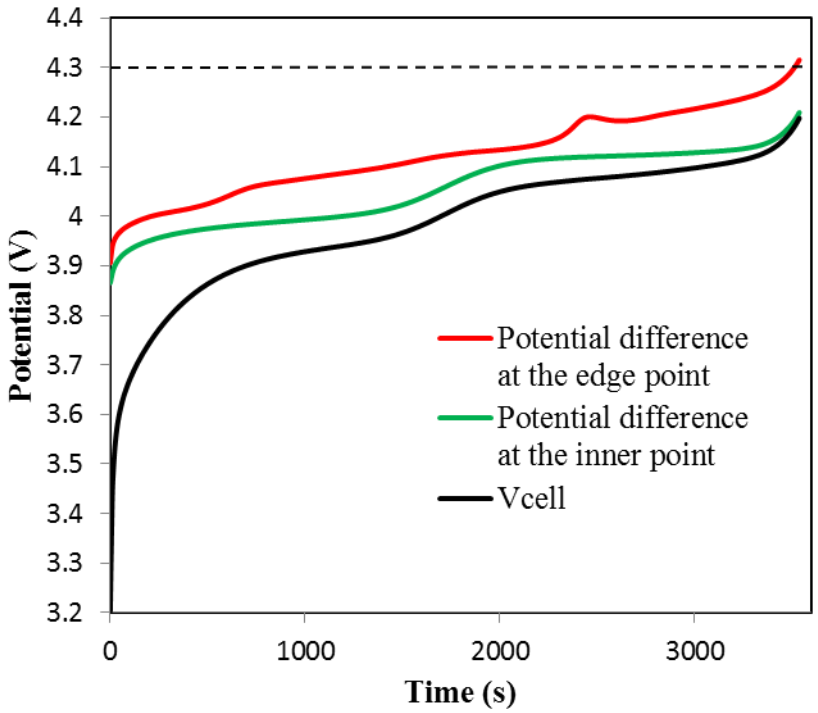

Figure 4.4 The potential difference, $\phi_1 - \phi_2$, at the edge point as well as at the inner point of cathode and the cell voltage as function of time during 1C charge for a cell with anode 1 mm extension over cathode.

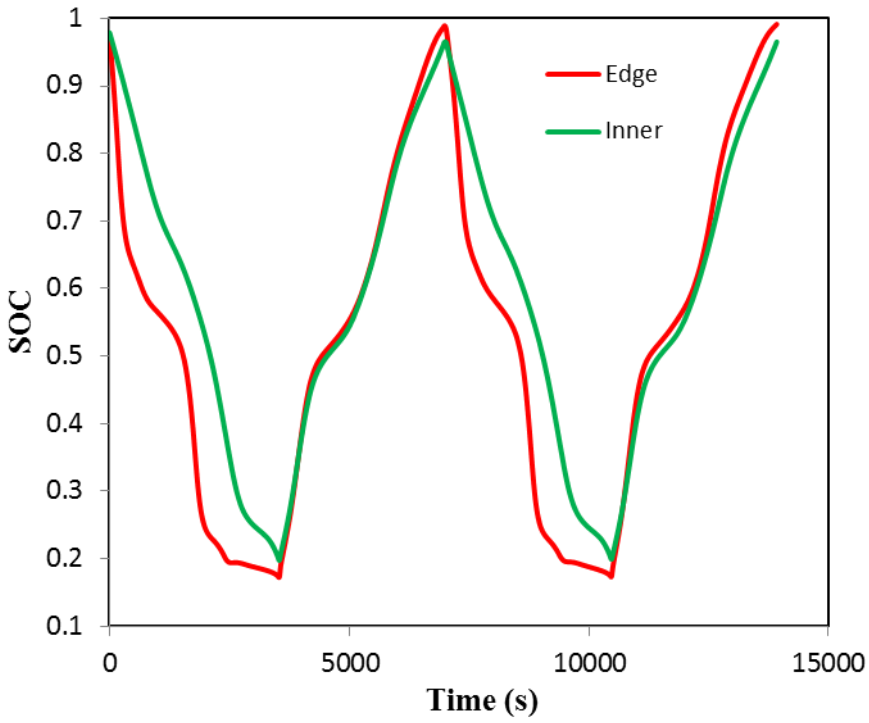

Figure 4.5 State of charge (SOC) vs. time at the edge point (Edge) as well as at the inner point (Inner) of cathode during 1C charge for a cell with anode 1 mm extension over cathode.

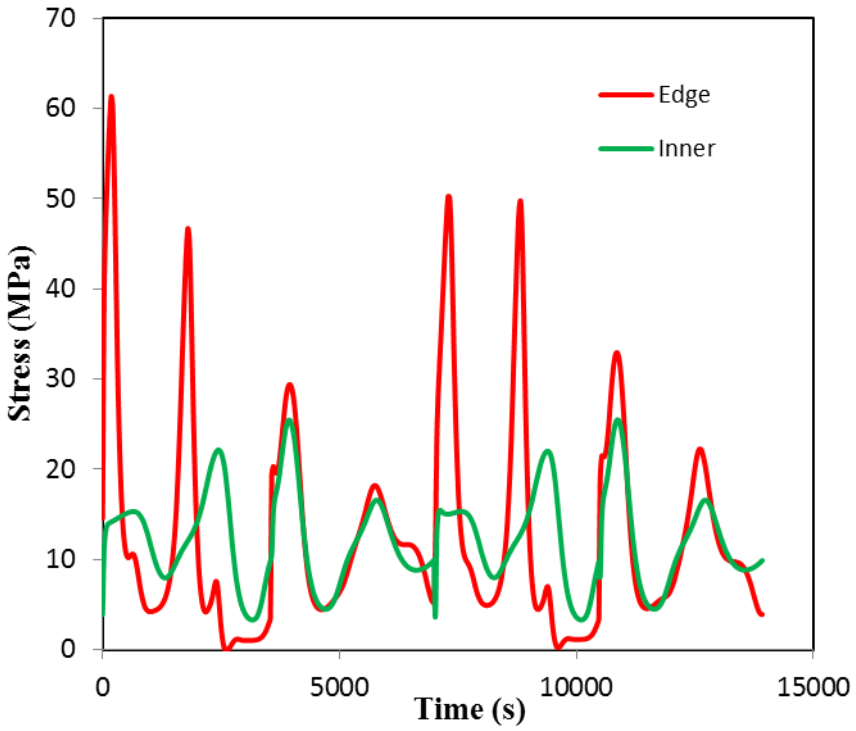

Figure 4.6 The estimated insertion-induced stress as function of time at the edge point (Edge) as well as at the inner point (Inner) of cathode during 1C charge for a cell with anode 1 mm extension over cathode.

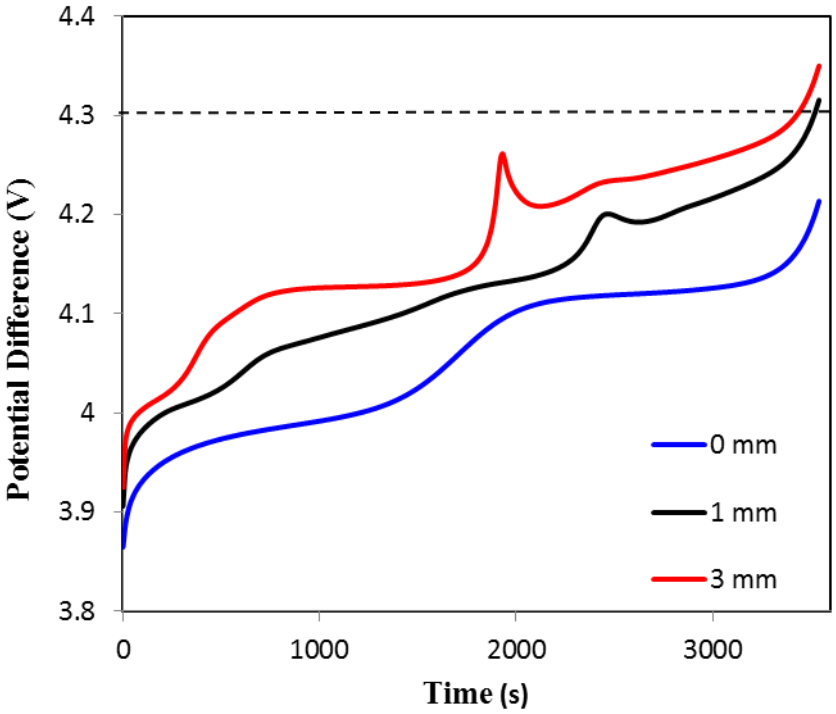

Figure 4.7 The potential difference at the edge of cathode against time during 1C charge for a cell with various anode extension lengths over cathode.

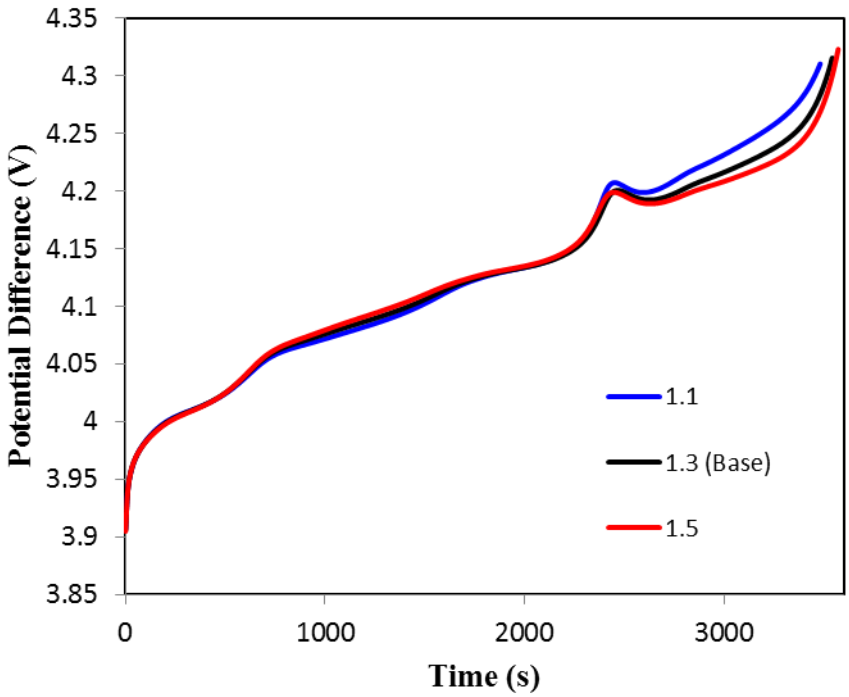

Figure 4.8 The effect of capacity ratio electrode on the magnitude of potential difference at the edge of cathode for a cell with anode 1 mm extension over cathode.

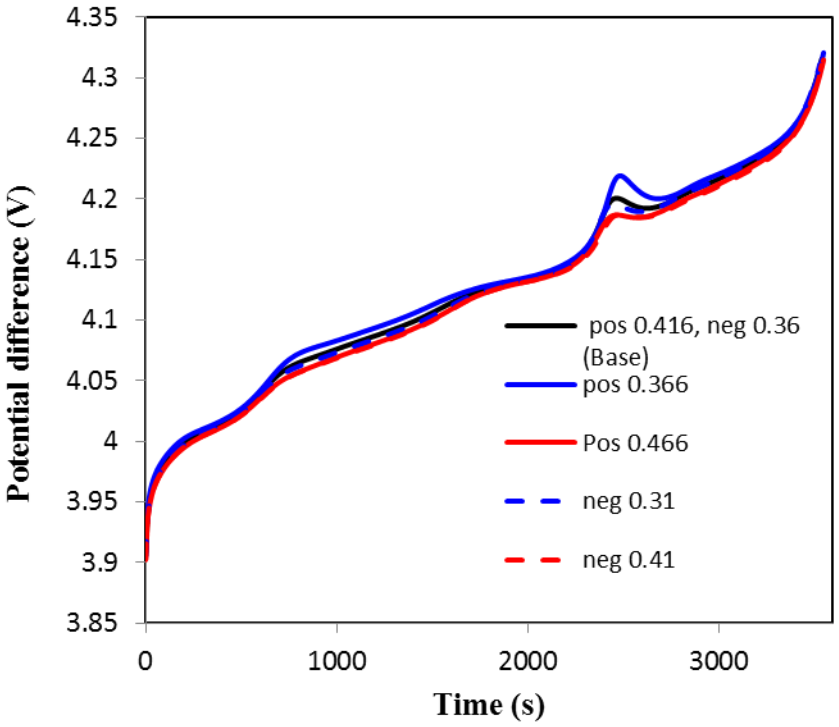

Figure 4.9 The effect of electrode porosity electrode on the magnitude of potential difference at the edge of cathode for a cell with anode 1 mm extension over cathode.

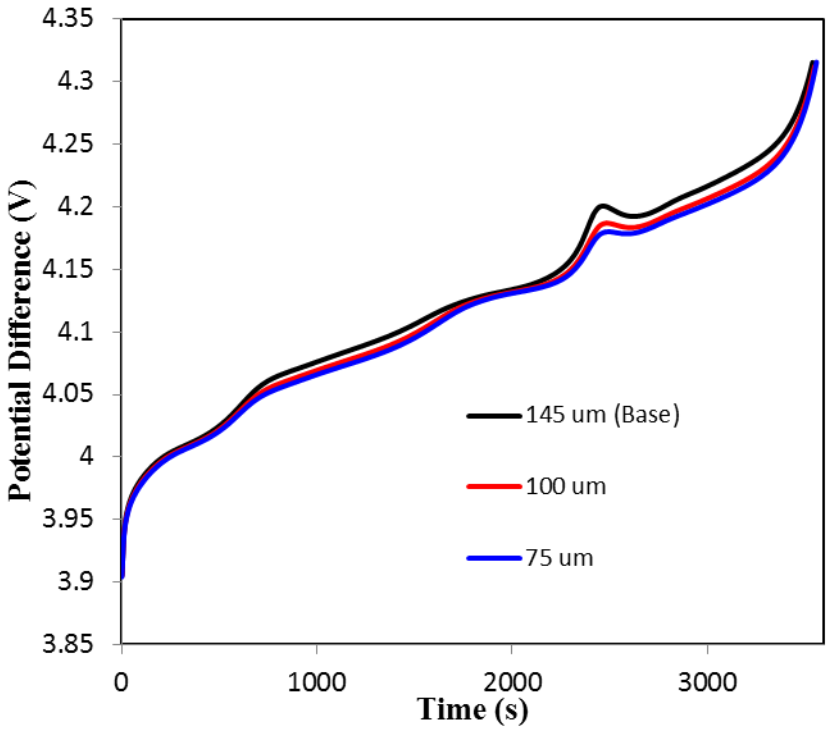

Figure 4.10 The effect of thickness of the positive electrode on the magnitude of potential difference at the edge of cathode for a cell with anode 1 mm extension over cathode.

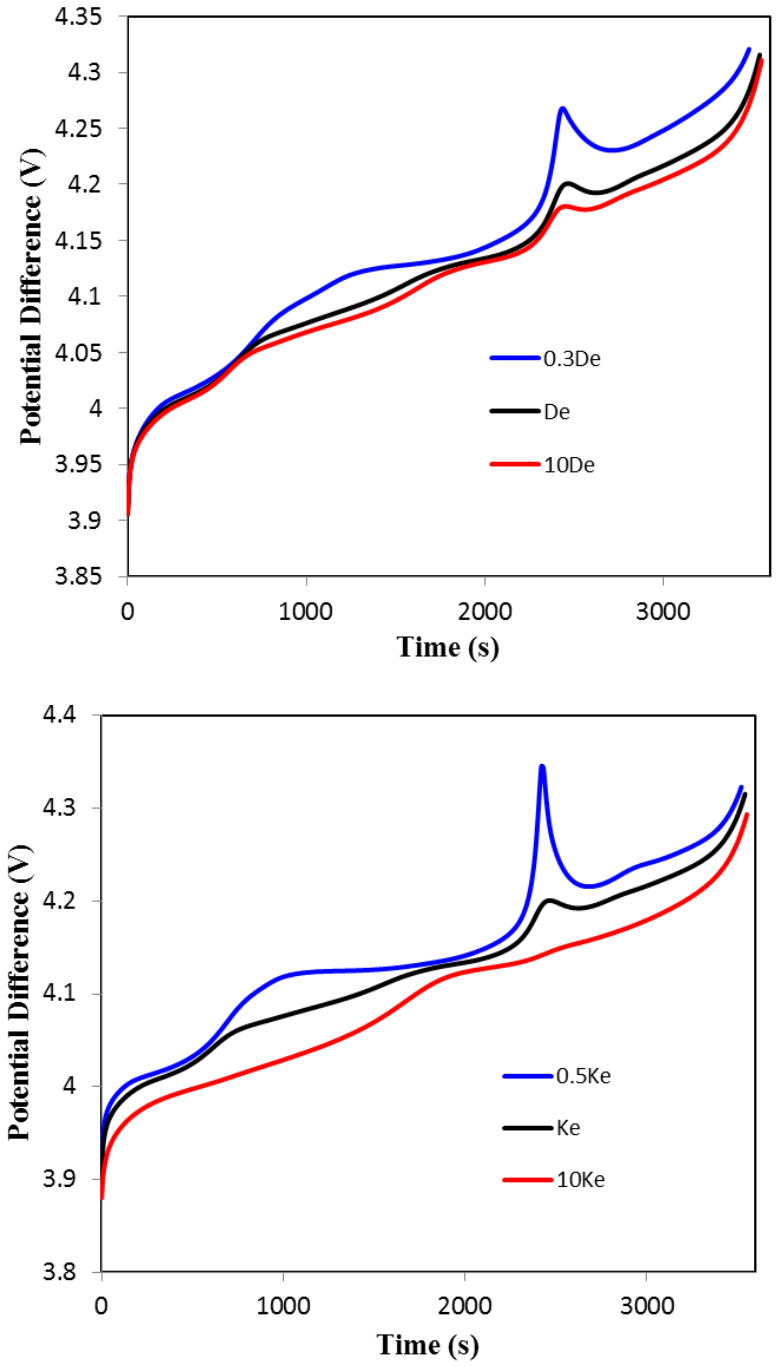

Figure 4.11 Investigate the effect of electrolyte properties on the over-potential behavior at the edge of cathode (a) the effect of Li ion solution diffusion coefficient; (b) the effect of electrolyte conductivity.

References

[1] J.B. Goodenough, Y. Kim, J Power Sources, **196** (2011) 6688-6694.

[2] J.B. Goodenough, Y. Kim, Chem Mater, **22** (2010) 587-603.

[3] P. Arora, R.E. White, M. Doyle, J Electrochem Soc, **145** (1998) 3647-3667.

[4] J. Vetter, P. Novak, M.R. Wagner, C. Veit, K.C. Moller, J.O. Besenhard, M. Winter, M. Wohlfahrt-Mehrens, C. Vogler, A. Hammouche, J Power Sources, **147** (2005) 269-281.

[5] M. Broussely, S. Herreyre, P. Biensan, P. Kasztejna, K. Nechev, R.J. Staniewicz, J. Power Sources, **97-8** (2001) 13-21.

[6] P. Ramadass, B. Haran, P.M. Gomadam, R. White, B.N. Popov, J Electrochem Soc, **151** (2004) A196-A203.

[7] D. Aurbach, J Power Sources, **89** (2000) 206-218.

[8] D. Aurbach, K. Gamolsky, B. Markovsky, G. Salitra, Y. Gofer, U. Heider, R. Oesten, M. Schmidt, J Electrochem Soc, **147** (2000) 1322-1331.

[9] W. Choi, A. Manthiram, J Electrochem Soc, **153** (2006) A1760-A1764.

[10] D.H. Jang, Y.J. Shin, S.M. Oh, J Electrochem Soc, **143** (1996) 2204-2211.

[11] D.H. Jang, S.M. Oh, J Electrochem Soc, **144** (1997) 3342-3348.

[12] E. Wang, D. Ofer, W. Bowden, N. Iltchev, R. Moses, K. Brandt, J Electrochem Soc, **147** (2000) 4023-4028.

[13] S. Komaba, N. Kumagai, Y. Kataoka, Electrochim Acta, **47** (2002) 1229-1239.

[14] H. Tsunekawa, S. Tanimoto, R. Marubayashi, M. Fujita, K. Kifune, M. Sano, J Electrochem Soc, **149** (2002) A1326-A1331.

[15] H.F. Wang, Y.I. Jang, B.Y. Huang, D.R. Sadoway, Y.T. Chiang, J Electrochem Soc, **146** (1999) 473-480.

[16] M.R. Lim, W.I. Cho, K.B. Kim, J Power Sources, **92** (2001) 168-176.

[17] S. Bhattacharya, A.R. Riahi, A.T. Alpas, J. Power Sources, **196** (2011) 8719-8727.

[18] R. Deshpande, M. Verbrugge, Y.T. Cheng, J. Wang, P. Liu, J Electrochem Soc, **159** (2012) A1730-A1738.

[19] M. Doyle, T.F. Fuller, J. Newman, J Electrochem Soc, **140** (1993) 1526-1533.

[20] T.F. Fuller, M. Doyle, J. Newman, J Electrochem Soc, **141** (1994) 1-10.

[21] R. Darling, J. Newman, J Electrochem Soc, **145** (1998) 990-998.

[22] P. Arora, M. Doyle, R.E. White, J Electrochem Soc, **146** (1999) 3543-3553.

[23] G. Sikha, B.N. Popov, R.E. White, J Electrochem Soc, **151** (2004) A1104-A1114.

[24] R. Kostecki, F. McLarnon, J Power Sources, **119** (2003) 550-554.

[25] R. Chromik, F. Beck, Electrochim Acta, **45** (2000) 2175-2185.

[26] H. Lee, S. Kim, J. Jeon, J.J. Cho, J Power Sources, **173** (2007) 972-978.

[27] A. Du Pasquier, A. Blyr, P. Courjal, D. Larcher, G. Amatucci, B. Gerand, J.M. Tarascon, J Electrochem Soc, **146** (1999) 428-436.

[28] S.T. Myung, K. Hosoya, S. Komaba, H. Yashiro, Y.K. Sun, N. Kumagai, Electrochim Acta, **51** (2006) 5912-5919.

[29] A. Antonini, C. Bellitto, M. Pasquali, G. Pistoia, J Electrochem Soc, **145** (1998) 2726-2732.

[30] T. Numata, C. Amemiya, T. Kumeuchi, M. Shirakata, M. Yonezawa, J Power Sources, **97-8** (2001) 358-360.

[31] Y.Y. Xia, Y.H. Zhou, M. Yoshio, J Electrochem Soc, **144** (1997) 2593-2600.

[32] T. Eriksson, A.M. Andersson, A.G. Bishop, C. Gejke, T. Gustafsson, J.O. Thomas, J Electrochem Soc, **149** (2002) A69-A78.

[33] D. Kim, S. Park, O.B. Chae, J.H. Ryu, Y.U. Kim, R.Z. Yin, S.M. Oh, J Electrochem Soc, **159** (2012) A193-A197.

[34] J. Park, J.H. Seo, G. Plett, W. Lu, A.M. Sastry, Electrochem Solid St, **14** (2011) A14-A18.

[35] C.H. Lu, S.W. Lin, Journal of Materials Research, **17** (2002) 1476-1481.

[36] L. Cai, Y. Dai, M. Nicolson, R.E. White, K. Jagannathan, G. GBhatia, J Power Sources, **221** (2013) 191-200.

[37] D. Guyomard, J.M. Tarascon, J Electrochem Soc, **140** (1993) 3071-3081.

[38] A. du Pasquier, A. Blyr, A. Cressent, C. Lenain, G. Amatucci, J.M. Tarascon, J Power Sources, **81** (1999) 54-59.

[39] W.H. Kong, H. Li, X.J. Huang, L.Q. Chen, J Power Sources, **142** (2005) 285-291.

[40] D. Aurbach, B. Markovsky, A. Shechter, Y. Ein-Eli, H. Cohen, J Electrochem Soc, **143** (1996) 3809-3820.

[41] R. Oesten, U. Heider, M. Schmidt, Solid State Ionics, **148** (2002) 391-397.

[42] C.G. Barlow, Electrochem Solid St, **2** (1999) 362-364.

[43] T. Kawamura, S. Okada, J. Yamaki, J Power Sources, **156** (2006) 547-554.

[44] R. Benedek, M.M. Thackeray, Electrochem Solid St, **9** (2006) A265-A267.

[45] J.C. Hunter, Journal of Solid State Chemistry, **39** (1981) 142-147.

[46] H. Yamane, T. Inoue, M. Fujita, M. Sano, J Power Sources, **99** (2001) 60-65.

[47] D. Aurbach, B. Markovsky, A. Shechter, Y. EinEli, H. Cohen, J Electrochem Soc, **143** (1996) 3809-3820.

[48] J.F. Yan, T.V. Nguyen, R.E. White, R.B. Griffin, J Electrochem Soc, **140** (1993) 733-742.

[49] K.E. Brenan, S.L. Campbell, L.R. Petzold, Numerical Solution of Initial Value Problems in Differential-Algebriac Equations, Elsevier, New York, 1989.

[50] Y.Y. Xia, T. Sakai, T. Fujieda, X.Q. Yang, X. Sun, Z.F. Ma, J. McBreen, M. Yoshio, J Electrochem Soc, **148** (2001) A723-A729.

[51] D. Aurbach, M.D. Levi, K. Gamulski, B. Markovsky, G. Salitra, E. Levi, U. Heider, L. Heider, R. Oesten, J Power Sources, **81** (1999) 472-479.

[52] D. Zhang, B.N. Popov, R.E. White, J Power Sources, **76** (1998) 81-90.

[53] S.R. Das, S.B. Majumder, R.S. Katiyar, J Power Sources, **139** (2005) 261-268.

[54] L.F. Wang, C.C. Ou, K.A. Striebel, J.J.S. Chen, J Electrochem Soc, **150** (2003) A905-A911.

[55] D.H. Jang, S.M. Oh, Electrochim Acta, **43** (1998) 1023-1029.

[56] M. Sano, T. Hattori, T. Hibino, M. Fujita, Electrochem Solid St, **10** (2007) A270-A273.

[57] B.H. Deng, H. Nakamura, M. Yoshio, J Power Sources, **180** (2008) 864-868.

[58] G. Amatucci, A. Du Pasquier, A. Blyr, T. Zheng, J.M. Tarascon, Electrochim Acta, **45** (1999) 255-271.

[59] M. Wohlfahrt-Mehrens, C. Vogler, J. Garche, J Power Sources, **127** (2004) 58-64.

[60] Y.L. Dai, L. Cai, R.E. White, J Electrochem Soc, **160** (2013) A182-A190.

[61] G.G. Amatucci, A. Blyr, C. Sigala, P. Alfonse, J.M. Tarascon, Solid State Ionics, **104** (1997) 13-25.

[62] J.M. Tarascon, W.R. Mckinnon, F. Coowar, T.N. Bowmer, G. Amatucci, D. Guyomard, J Electrochem Soc, **141** (1994) 1421-1431.

[63] P. Arora, B.N. Popov, R.E. White, J Electrochem Soc, **145** (1998) 807-815.

[64] G.H. Li, H. Ikuta, T. Uchida, M. Wakihara, J Electrochem Soc, **143** (1996) 178-182.

[65] G.G. Amatucci, N. Pereira, T. Zheng, I. Plitz, J.M. Tarascon, J Power Sources, **81** (1999) 39-43.

[66] W. Choi, A. Manthiram, Electrochem Solid St, **9** (2006) A245-A248.

[67] S.T. Myung, M.H. Cho, H.T. Hong, T.H. Kang, C.S. Kim, J Power Sources, **146** (2005) 222-225.

[68] H.Y. Tran, C. Taubert, M. Fleischhammer, P. Axmann, L. Kuppers, M. Wohlfahrt-Mehrens, J Electrochem Soc, **158** (2011) A556-A561.

[69] A. Manthiram, W. Choi, Electrochem Solid St, **10** (2007) A228-A231.

[70] A.J. Smith, S.R. Smith, T. Byrne, J.C. Burns, J.R. Dahn, J Electrochem Soc, **159** (2012) A1696-A1701.

[71] H. Gabrisch, J. Wilcox, M.M. Doeff, Electrochem Solid St, **11** (2008) A25-A29.

[72] W.I.F. David, M.M. Thackeray, L.A. Depicciotto, J.B. Goodenough, J Solid State Chem, **67** (1987) 316-323.

[73] J. Christensen, J. Newman, J Solid State Electr, **10** (2006) 293-319.

[74] J. Christensen, J. Newman, J Electrochem Soc, **153** (2006) A1019-A1030.

[75] X.C. Zhang, W. Shyy, A.M. Sastry, J Electrochem Soc, **154** (2007) A910-A916.

[76] Y.T. Cheng, M.W. Verbrugge, J Power Sources, **190** (2009) 453-460.

[77] R.E. Garcia, Y.M. Chiang, W.C. Carter, P. Limthongkul, C.M. Bishop, J Electrochem Soc, **152** (2005) A255-A263.

[78] S. Golmon, K. Maute, M.L. Dunn, Comput Struct, **87** (2009) 1567-1579.

[79] S. Renganathan, G. Sikha, S. Santhanagopalan, R.E. White, J Electrochem Soc, **157** (2010) A155-A163.

[80] J. Christensen, J Electrochem Soc, **157** (2010) A366-A380.

[81] A.F. Bower, P.R. Guduru, V.A. Sethuraman, J Mech Phys Solids, **59** (2011) 804-828.

[82] P. Albertus, J. Christensen, J. Newman, J Electrochem Soc, **156** (2009) A606-A618.

[83] S.P. Timoshenko, J.N. Goodier, Theory of Elasicity, McGraw-Hill, New York, 1970.

[84] F.Q. Yang, Mat Sci Eng a-Struct, **409** (2005) 153-159.

[85] L. Cai, R.E. White, J Power Sources, **196** (2011) 5985-5989.

[86] V.R. Subramanian, R.E. White, J Power Sources, **96** (2001) 385-395.

[87] M.M. Thackeray, Y. Shao-Horn, A.J. Kahaian, K.D. Kepler, J.T. Vaughey, S.A. Hackney, Electrochem Solid St, **1** (1998) 7-9.

[88] M.C. Tucker, J.A. Reimer, E.J. Cairns, J Electrochem Soc, **149** (2002) A574-A585.

[89] J.L. Lei, L.J. Li, R. Kostecki, R. Muller, F. McLarnon, J Electrochem Soc, **152** (2005) A774-A777.

[90] L. Cai, K. An, Z.L. Feng, C.D. Liang, S.J. Harris, J. Power Sources, **236** (2013) 163-168.

[91] E. Scott, G. Tam, B. Anderson, C. Schmidt, Paper 1282 presented at The Electrochemical Society Meeting, Orlando, FL, Oct 13, 2003.

[92] Y. Chen, J.W. Evans, J. Electrochem. Soc., **140** (1993) 1833-1838.

[93] D.R. Baker, M.W. Verbrugge, J. Electrochem. Soc., **146** (1999) 2413-2424.

[94] J.N. Harb, R.M. LaFollette, J. Electrochem. Soc., **146** (1999) 809-818.

[95] G.H. Kim, K. Smith, K.J. Lee, S. Santhanagopalan, A. Pesaran, J. Electrochem. Soc., **158** (2011) A955-A969.

[96] A. Awarke, S. Pischinger, J. Ogrzewalla, J. Electrochem. Soc., **160** (2013) A172-A181.

[97] M. Tang, P. Albertus, J. Newman, J. Electrochem. Soc., **156** (2009) A390-A399.

[98] J. Wu, V. Srinivasan, J. Xu, C.Y. Wang, J. Electrochem. Soc., **149** (2002) A1342-A1348.

[99] V.R. Subramanian, V.D. Diwakar, D. Tapriyal, J. Electrochem. Soc., **152** (2005) A2002-A2008.

[100] K. Eberman, P.M. Gomadam, J. Jain, E. Scott, ECS Transactions, **25** (2010) 47-58.

[101] Y.L. Dai, L. Cai, R.E. White, J. Power Sources, **submitted**.

[102] P. Arora, M. Doyle, A.S. Gozdz, R.E. White, J. Newman, J. Power Sources, **88** (2000) 219-231.

[103] K. Kumaresan, G. Sikha, R.E. White, J. Electrochem. Soc., **155** (2008) A164-A171.

[104] L.O. Valoen, J.N. Reimers, J. Electrochem. Soc., **152** (2005) A882-A891.

[105] M. Doyle, J. Newman, A.S. Gozdz, C.N. Schmutz, J.M. Tarascon, J Electrochem Soc, **143** (1996) 1890-1903.

Appendix A: Properties of Electrolyte and Electrode in Chapter 2

Transport properties:

The effective diffusion coefficient of species *i* in the electrolyte in region *j*, is determined by the following equation:

$$D_{eff,i} = D_i \varepsilon_{2,j}^{\text{brugg}_j}, \; i=\text{H}_2\text{O}, \text{Mn}^{2+}, \text{H}^+, \text{Li}^+ \quad j = pos, sep \tag{A.1}$$

where D_i denotes the diffusion coefficient of species *i* in the bulk electrolyte and brugg_j is the Bruggeman number of region *j*.

The effective conductivity of Li^+ in the electrolyte in region *j* is as following:

$$\kappa_{\text{eff},j} = \kappa \varepsilon_{2,j}^{\text{brugg}_j}, \; j = pos, sep \tag{A.2}$$

where κ is the conductivity of Li^+ in the bulk electrolyte.

The effective conductivity of the solid phase is as following:

$$\sigma_{\text{eff}} = \sigma \varepsilon_{1,pos}^{\text{brugg}_j} \tag{A.3}$$

where σ is the conductivity of the solid phase.

The concentration and temperature dependent Li^+ ionic conductivity, κ, and the diffusion coefficient , D_{Li^+} , in the electrolyte are given by:[104]

$$\kappa = 10^{-4} \times c_{Li^+} \left(\begin{array}{l} -10.5 + 0.668 \times 10^{-3} c_{Li^+} + 0.494 \times 10^{-6} c_{Li^+}^2 + 0.074T \\ -1.78 \times 10^{-5} c_{Li^+} T - 8.86 \times 10^{-10} c_{Li^+}^2 T - 6.96 \times 10^{-5} T^2 \\ +2.80 \times 10^{-8} c_{Li^+} T^2 \end{array} \right)^2 \tag{A.4}$$

$$D_{Li^+} = 10^{-4} \times 10^{-4.43 - \frac{54}{T - 229 - 5.0 \times 10^{-3} c_{Li^+}} - 0.22 \times 10^{-3} c_{Li^+}} \tag{A.5}$$

Electrode Thermodynamic data:

The open circuit potentials for the $LiMn_2O_4$ cathode as a function of state of charge is given by:[105]

$$\begin{aligned} U_p = {} & 4.19829 + 0.0565661 \tanh\left(-14.5546\theta + 8.60942\right) \\ & - 0.0275479 \left(\frac{1}{\left(0.998432 - \theta\right)^{0.492465}} - 1.90111 \right) \\ & - 0.157123 \exp\left(-0.04738\theta^8\right) + 0.810239 \exp\left(-40\left(\theta - 0.133875\right)\right) \end{aligned} \tag{A.6}$$

where the SOC is defined by:

$$\theta = \frac{c_{s,surf}}{c_{s,\max}} \tag{A.7}$$

Appendix B: Properties of Electrolyte and Electrode in Chapter 3

The effective ionic conductivity and diffusion coefficient in the binary electrolyte are determined by the following equations, respectively:[82]

$$\kappa_{\text{eff},j} = \frac{\kappa \varepsilon_{2,j}}{\tau_j}, \qquad j = p, s, n \tag{B.1}$$

$$D_{\text{eff},j} = \frac{D \varepsilon_{2,j}}{\tau_j}, \qquad j = p, s, n \tag{B.2}$$

where τ_j is the tortuosity of the porous electrode.

The concentration dependent ionic conductivity and the diffusion coefficient in the binary electrolyte are given by:[82]

$$\kappa = 0.84\left(\frac{1.134\frac{c_{Li^+}}{1000}}{1+0.2(\frac{c_{Li^+}}{1000})+0.08(\frac{c_{Li^+}}{1000})^4}+0.1\right) \tag{B.3}$$

$$D = 6.5\times10^{-10}\exp(-0.7\frac{c_{Li^+}}{1000}) \tag{B.4}$$

The effective conductivity in the solid phase is defined as

$$\sigma_{eff,j} = \sigma_j,\ j = p, n \tag{B.5}$$

The ionic activity coefficient, *f*, is given as following:[82]

$$1+\frac{\partial \ln f}{\partial \ln c_{Li^+}}=1+\frac{c_{Li^+}}{1000}\left[\begin{array}{l}\dfrac{-1.0178}{2(1+0.9831(\frac{c_{Li^+}}{1000})^{0.5})}\left(\dfrac{1}{(\frac{c_{Li^+}}{1000})^{0.5}}-\dfrac{0.9831}{1+0.9831(\frac{c_{Li^+}}{1000})^{0.5}}\right)\\ +1.5842\end{array}\right] \tag{B.6}$$

The Li diffusion coefficient in NCA particle[82] is given as follows:

$$D_{s,NCA}=3\times10^{-15}\left(\left(1+tanh\left(-20\left(\theta_{NCA}-0.73\right)\right)\right)+0.02\right) \tag{B.7}$$

The open circuit potentials for the $LiMn_2O_4$ cathode as functions of state of charge are given by:[105]

$$\begin{aligned}U_{LMO}=&\,4.199+0.05661\tanh\left(-14.555\theta_{LMO}+8.609\right)\\&-0.0275\left(\frac{1}{\left(0.998-\theta_{LMO}\right)^{0.492}}-1.901\right)\\&-0.157\exp\left(-0.0474\theta_{LMO}^{8}\right)+0.810\exp\left(-40\left(\theta_{LMO}-0.134\right)\right)\end{aligned} \tag{B.8}$$

The open circuit potential for NCA (fit to experimental data) is given by:

$0.36\le\theta_{NCA}\le0.410$,

$$\begin{aligned}U_{NCA}=&\,8.535-17.059\theta_{NCA}+21.038\theta_{NCA}^2-9.153\theta_{NCA}^3+9.875(\theta_{NCA}-0.700)^3\\&-2.176(\theta_{NCA}-0.550)^3-1331.866(\theta_{NCA}-0.410)^3;\end{aligned} \tag{B.9}$$

$0.410\le\theta_{NCA}\le0.55$,

$$\begin{aligned}U_{NCA}=&\,8.535-17.059\theta_{NCA}+21.038\theta_{NCA}^2-9.153\theta_{NCA}^3+9.875(\theta_{NCA}-0.700)^3\\&-2.176(\theta_{NCA}-0.550)^3;\end{aligned} \tag{B.10}$$

$0.55\le\theta_{NCA}\le0.7$,

$$U_{NCA} = 8.535 - 17.059\theta_{NCA} + 21.038\theta_{NCA}^2 - 9.153\theta_{NCA}^3 + 9.875(\theta_{NCA} - 0.700)^3; \quad \text{(B.11)}$$

$0.7 \le \theta_{NCA} \le 0.935$,

$$U_{NCA} = 8.535 - 17.059\theta_{NCA} + 21.038\theta_{NCA}^2 - 9.153\theta_{NCA}^3; \quad \text{(B.12)}$$

$0.935 \le \theta_{NCA} \le 0.959$,

$$\begin{aligned} U_{NCA} = {} & 8.535 - 17.059\theta_{NCA} + 21.038\theta_{NCA}^2 - 9.153\theta_{NCA}^3 + 9.875(\theta_{NCA} - 0.700)^3 \\ & - 5370.872(\theta_{NCA} - 0.935)^3; \end{aligned} \quad \text{(B.13)}$$

$0.959 \le \theta_{NCA} \le 0.980$,

$$\begin{aligned} U_{NCA} = {} & 8.535 - 17.059\theta_{NCA} + 21.038\theta_{NCA}^2 - 9.153\theta_{NCA}^3 + 9.875(\theta_{NCA} - 0.700)^3 \\ & - 5370.872(\theta_{NCA} - 0.935)^3 - 47690.304(\theta_{NCA} - 0.959)^3. \end{aligned} \quad \text{(B.14)}$$

And the open circuit potential for the carbon anode (fit to experimental data) is as follows:

$0.001 \le \theta_C \le 0.0109$,

$$\begin{aligned} U_C = {} & 0.113 - 0.0208\tanh(15.064\theta_C - 8.199) - 2.435(\theta_C - 0.440)^3 \\ & + 65.394(\theta_C - 0.154)^3 - 960.307(\theta_C - 0.0897)^3 \\ & - 1.006 \times 10^7 (\theta_C - 0.0109)^3; \end{aligned} \quad \text{(B.15)}$$

$0.0109 \le \theta_C \le 0.0897$,

$$\begin{aligned} U_C = {} & 0.113 - 0.0208\tanh(15.064\theta_C - 8.199) - 2.435(\theta_C - 0.440)^3 \\ & + 65.394(\theta_C - 0.154)^3 - 960.307(\theta_C - 0.0897)^3; \end{aligned} \quad \text{(B.16)}$$

$0.0897 \le \theta_C \le 0.154$,

$$\begin{aligned} U_C = {} & 0.113 - 0.0208\tanh(15.064\theta_C - 8.199) - 2.435(\theta_C - 0.440)^3 \\ & + 65.394(\theta_C - 0.154)^3; \end{aligned} \quad \text{(B.17)}$$

$0.0897 \le \theta_C \le 0.154$,

$$U_C = 0.113 - 0.0208\tanh(15.064\theta_C - 8.199) - 2.435(\theta_C - 0.440)^3 + 65.394(\theta_C - 0.154)^3; \quad (B.18)$$

$0.154 \le \theta_C \le 0.440$,

$$U_C = 0.113 - 0.0208\tanh(15.064\theta_C - 8.199) - 2.435(\theta_C - 0.440)^3; \quad (B.19)$$

$0.440 \le \theta_C \le 0.854$,

$$U_C = 0.113 - 0.0208\tanh(15.064\theta_C - 8.199); \quad (B.20)$$

$0.854 \le \theta_C \le 0.92$,

$$U_C = 0.113 - 0.0208\tanh(15.064\theta_C - 8.199) - 252.707(\theta_C - 0.854)^3; \quad (B.21)$$

where the SOC, θ, is defined by:

$$\theta_k = \frac{c_{surf,k}}{c_{\max,k}}, \quad k = LMO, NCA, C \quad (B.22)$$

Appendix C: Properties of Electrolyte and Electrode in Chapter 4

The effective ionic conductivity and diffusion coefficient in the binary electrolyte are determined by the following equations, respectively:

$$\kappa_{eff,i} = \varepsilon_i^{brugg_i} \kappa, \quad i = p,s,n,e \tag{C.1}$$

$$D_{e,eff,i} = \varepsilon_i^{brugg_i} D_e, \quad i = p,s,n,e \tag{C.2}$$

The concentration dependent ionic conductivity and the diffusion coefficient in the binary electrolyte are given by [104]:

$$\kappa = 10^{-4} \times c_e \begin{pmatrix} -10.5 + 0.668\times10^{-3} c_e + 0.494\times10^{-6} c_e^2 \\ +0.074T - 1.78\times10^{-5} c_e T - 8.86\times10^{-10} c_e^2 T \\ -6.96\times10^{-5} T^2 + 2.80\times10^{-8} c_e T^2 \end{pmatrix}^2 \tag{C.3}$$

$$D_e = 10^{-4} \times 10^{-4.43 - \frac{54}{T-229-5.0\times10^{-3} c_e} - 0.22\times10^{-3} c_e} \tag{C.4}$$

The effective conductivity in the solid phase is defined as

$$\sigma_{eff,i} = \varepsilon_{1,i} \sigma, \quad i = p,n \tag{C.5}$$

The open circuit potentials for the $LiMn_2O_4$ cathode as functions of state of charge are given by [105]:

$$
\begin{aligned}
U_{LMO} = {} & 4.19829 + 0.0565661\tanh\left(-14.5546\theta_{LMO} + 8.60942\right) \\
& - 0.0275479\left(\frac{1}{\left(0.998432 - \theta_{LMO}\right)^{0.492465}} - 1.90111\right) \\
& - 0.157123\exp\left(-0.04738\theta_{LMO}^{8}\right) + 0.810239\exp\left(-40\left(\theta_{LMO} - 0.133875\right)\right)
\end{aligned}
\tag{C.6}
$$

The open circuit potentials for the carbon anode as functions of state of charge are given by [22]:

$$
\begin{aligned}
U_C = {} & 0.7222 + 0.13868\theta_C + 0.028952\theta_C^{\,0.5} - \frac{0.017189}{\theta_C} \\
& + \frac{0.0019144}{\theta_C^{\,1.5}} + 0.28082\exp\left[15(0.06 - \theta_C)\right] \\
& - 0.79844\exp\left[0.44649(\theta_C - 0.92)\right]
\end{aligned}
\tag{C.7}
$$

where the SOC, θ, is defined by:

$$
\theta = \frac{c_{s,surf}}{c_{\max}} \tag{C.8}
$$